


11-17-2015

Corrosion of Steel in Submerged Concrete Structures

Michael Thomas Walsh

University of South Florida, mtwalsh@mail.usf.edu

Follow this and additional works at: <http://scholarcommons.usf.edu/etd>

 Part of the [Civil Engineering Commons](#), and the [Mechanical Engineering Commons](#)

Scholar Commons Citation

Walsh, Michael Thomas, "Corrosion of Steel in Submerged Concrete Structures" (2015). *Graduate Theses and Dissertations*.
<http://scholarcommons.usf.edu/etd/6048>

This Dissertation is brought to you for free and open access by the Graduate School at Scholar Commons. It has been accepted for inclusion in Graduate Theses and Dissertations by an authorized administrator of Scholar Commons. For more information, please contact scholarcommons@usf.edu.

Corrosion of Steel in Submerged Concrete Structures

by

Michael T. Walsh

A dissertation submitted in partial fulfillment
of the requirements for the degree of
Doctor of Philosophy in Civil Engineering
Department of Civil and Environmental Engineering
College of Engineering
University of South Florida

Major Professor: Alberto A. Sagüés, Ph.D.
Julie Harmon, Ph.D.
Babu Joseph, Ph.D.
Clifford Merz, Ph.D.
Gray Mullins, Ph.D.

Date of Approval:
November 10, 2015

Keywords: rebar, potential dependent threshold, marine, cathodic protection,
chloride, passivity

Copyright © 2015, Michael T. Walsh

DEDICATION

This dissertation is dedicated to God, who in his sovereignty and providence gave me my wife Jennifer, my son Mickey, and the other uncountable, unearned, unmerited, and undeserved gifts that made this work possible.

ACKNOWLEDGMENTS

The work described herein was supported by the State of Florida Department of Transportation (FDOT). The opinions, findings, and conclusions presented here are those of the author and not necessarily those of the FDOT.

The author acknowledges the invaluable guidance, support, and encouragement of his advisor and mentor, Dr. Alberto A. Sagüés, and further acknowledges an enormous debt of gratitude to same. The author is grateful to the committee chair and members, Drs. Cai, Harmon, Joseph, Merz, and Mullins for their collective and individual support and input for this dissertation. The assistance and support of Mr. Mario Paredes, Mr. Ivan Lasa, Mr. Paul Vinik, Mr. Ronald Simmons, and Mr. Dennis Baldi from the FDOT State Materials Office is also gratefully acknowledged.

The author wishes to extend sincere gratitude to his colleagues at the University of South Florida Corrosion Engineering Laboratory including Drs. Lau, Dugarte, Akhoondan, Busba, and Sánchez in addition to S. Hoffman, J. Fernandez, E. Paz, M. Hutchinson, L. Emmenegger, K. Williams, S. Alsherhi, J. Bumgardner, A. Ramirez Marquina, B. Kociuba, and each of the undergraduate lab technicians. The help and support of Deborah Brown-Volkman is gratefully acknowledged and greatly appreciated.

TABLE OF CONTENTS

LIST OF TABLES.....	iii
LIST OF FIGURES.....	iv
ABSTRACT	vii
CHAPTER 1: INTRODUCTION.....	1
1.1 Research Problem Statement and Objectives	1
1.2 Background	2
1.3 Relevance and Outlook	4
1.4 Corrosion of Reinforcing Steel in Submerged Concrete	5
1.5 Summary of Scope and Approach.....	10
CHAPTER 2: FIELD ASSESSMENT.....	11
2.1 Structures and Elements Examined	11
2.2 Field Assessment Methods.....	12
2.3 Field Assessment Results	15
2.3.1 Bridge A: Skyway Fishing Pier	15
2.3.2 Bridge B: Pinellas Bayway Drawbridge	18
2.3.3 Bridge C: Sunrise Key Bridge	20
2.4 Field Assessment Findings and Discussion.....	20
CHAPTER 3: STEADY-STATE MODELING	36
3.1 Steel Surface Condition in the Submerged Zone.....	36
3.2 Steady-State Model Assumptions and Configuration	39
3.3 Scenarios Examined.....	44
3.4 Modeling Results and Discussion.....	45
3.5 Steady-State Modeling Discussion	48
CHAPTER 4: DYNAMIC EVOLUTION MODEL	56
4.1 Background	56
4.2 Model Formulation.....	59
4.3 Results and Discussion	67
4.3.1 Projections for Unprotected Systems.....	67
4.3.2 Projections for Cathodically Protected Systems	73
4.4 Significance of Modeling Findings	75

CHAPTER 5: RECOMMENDED FUTURE RESEARCH.....	87
CHAPTER 6: CONCLUSIONS.....	92
REFERENCES.....	94
APPENDIX A: INITIAL CHLORIDE ANALYSIS, BRIDGE A.....	100
APPENDIX B: POTENTIAL MAPPING, BRIDGE A	103
APPENDIX C: SUNSHINE SKYWAY BRIDGE PIER FOOTERS	106
C.1 Background.....	106
C.2 Empty-Chamber Inspection.....	107
C.2.1 Methods and Results.....	107
C.2.1.1 Pier Footer Water Analysis	107
C.2.1.2 Post-dewatering Crack Seepage	109
C.2.1.3 Coring	110
C.2.1.4 Core Analysis, General.....	113
C.2.1.5 Core Analysis, Chloride	114
C.3 Filled-Chamber Inspection	117
C.4 Discussion.....	119
APPENDIX D: ROBUSTNESS OF MODEL OUTPUT.....	122
D.1 Mesh Size (Dynamic Model)	122
D.2 Steel Factor (SF) (Steady-State Model).....	123
D.3 Surface Chloride Concentration Profile (Dynamic Model).....	124
APPENDIX E: COPYRIGHT PERMISSION	126
ABOUT THE AUTHOR.....	END PAGE

LIST OF TABLES

Table 1.	Structure assessment data.....	24
Table 2.	Chloride content of Bridge A pile core slices	25
Table 3.	Chloride content of Bridge B specimens	25
Table 4.	Parameter and variable descriptions and values.....	51
Table 5.	Distribution of active and passive regions	51
Table 6.	Parameter values used in the dynamic evolution model simulations.....	80
Table 7.	Cases evaluated.....	81
Table A1.	Observed chloride concentrations.....	101
Table C1.	Sunshine Skyway pier footer water laboratory analysis results	108
Table C2.	Sunshine Skyway pier footer crack seepage water properties	110
Table C3.	Core data	113

LIST OF FIGURES

Figure 1.	Bridge A piles resting side-by-side on horizontal concrete columns.....	26
Figure 2.	Typical configuration and dimensions of Bridge A piles	26
Figure 3.	Bridge A piles, end view	26
Figure 4.	Typical configuration and dimensions of Bridge B piles	27
Figure 5.	Typical configuration and dimensions of Bridge C piles	27
Figure 6.	Cross-section of Pile #2 showing vertical and horizontal saw cuts.....	27
Figure 7.	Schematic diagram of vertical and horizontal saw cuts.....	28
Figure 8.	Actual vertical and horizontal saw cuts.....	28
Figure 9.	Rust stains in concrete cover observed during bar removal.....	28
Figure 10.	Submerged (i.e., bottom) end of pile from Bridge B, end view	29
Figure 11.	Bridge B pile selected for autopsy	29
Figure 12.	Submerged end of another pile from Bridge B	29
Figure 13.	Autopsied Bridge B pile.....	30
Figure 14.	Corrosion-free steel in much of Bridge C submerged region.....	30
Figure 15.	Corroded rebar.....	30
Figure 16.	Severe localized corrosion-related cross-section loss, Bridge A	31
Figure 17.	Cross-section loss survey	31
Figure 18.	Estimated perimeter-averaged local corrosion rate.....	32
Figure 19.	Chloride content as a function of depth from concrete surface	33

Figure 20. Exposed strand in region nearest waterline of autopsied pile	33
Figure 21. Three different instances of localized corrosion	34
Figure 22. Concrete fragment mounted on mill table	35
Figure 23. Locally corroded steel in region below mudline.....	35
Figure 24. Bottom half of pile left in place	35
Figure 25. Concrete column model schematic diagram	52
Figure 26. Potential and oxygen concentration distribution for base case.....	53
Figure 27. Oxygen content in the bulk of the concrete	53
Figure 28. Projections for column with active corrosion above the waterline	54
Figure 29. Projections for column with no corrosion above the waterline.....	54
Figure 30. Corrosion rate as a function of active rebar surface area percentage	55
Figure 31. Dynamic evolution model schematic diagram	82
Figure 32. Chloride concentration penetration as function of column age.....	83
Figure 33. Time evolution of chloride concentration and chloride threshold.....	83
Figure 34. Chloride concentration.	84
Figure 35. Potential distribution evolution with time for Case 1	84
Figure 36. Damage functions using above-water damage declaration criterion	85
Figure 37. Damage functions using alternative damage declaration criterion	86
Figure 38. Damage functions for alternate anode potentials	86
Figure A1. Observed chloride concentrations	101
Figure B1. Half-cell potential at 6-inch intervals	104
Figure C1. Resistivity and dissolved oxygen profiles.....	109
Figure C2. Rebar at the bottom of hole at core #1	111

Figure C3.	Rebar at core #4 site	112
Figure C4.	Rebar at core #5 site	113
Figure C5.	Core slicing scheme	114
Figure C6.	Core mounted on mill table.....	115
Figure C7.	Degree of inconsistency	116
Figure C8.	Chloride concentration.....	116
Figure C9.	Comparison of chloride penetration in cores	118
Figure C10.	Resistivity of pier footer water.....	118
Figure D1.	CR as a function of active rebar surface area percentage.....	124
Figure D2.	Damage functions for multiple chloride profiles, Case 1	125

ABSTRACT

This investigation determined that severe corrosion of steel can occur in the submerged portions of reinforced concrete structures in marine environments. Field studies of decommissioned pilings from actual bridges revealed multiple instances of strong corrosion localization, showing appreciable local loss of steel cross-section. Quantitative understanding of the phenomenon and its causes was developed and articulated in the form of a predictive model. The predictive model output was consistent with both the corrosion rate estimates and the extent of corrosion localization observed in the field observations. The most likely explanation for the observed phenomena that emerged from the understanding and modeling is that cathodic reaction rates under oxygen diffusional limitation that are negligible in cases of uniform corrosion can nevertheless support substantial corrosion rates if the corrosion becomes localized. A dynamic evolution form of the model was created based on the proposition that much of the steel in the submerged concrete zone remained in the passive condition given cathodic prevention that resulted from favorable macrocell coupling with regions of the steel that had experienced corrosion first. The model output also matched observations from the field, supporting the plausibility of the proposed scenario.

The modeling also projected that corrosion in the submerged zone could be virtually eliminated via the use of sacrificial anode cathodic protection; the rate of

corrosion damage progression in the low elevation zone above water could also be significantly reduced. Continuation work should be conducted to define an alternative to the prevalent limit-state i.e., visible external cracks and spalls, for submerged reinforced concrete structures. Work should also be conducted to determine the possible structural consequences of this form of corrosion and to assess the technical feasibility and cost/benefit aspects of incorporating protective anodes in new pile construction.

CHAPTER 1: INTRODUCTION

1.1 Research Problem Statement and Objectives

Current design guidelines, manufacturing processes, and construction practices for reinforced concrete structural elements serving in partially submerged conditions in marine environments may not fully address certain issues that can directly affect a structure's durability and performance. In particular, the vulnerability of steel reinforcement to corrosion in the submerged region has not been well-established.

This dissertation asserts that substantial corrosion in the submerged region is possible, that localized corroding regions can be stabilized by macrocell action and chloride threshold dependence on local potential, and that corrosion rates can be much greater than expected.

To supplement a limited knowledge-base, field assessments of actual structural elements were made and a specialized computer-based model was developed and implemented. Ultimately the work described herein was intended to show that:

1. Severe localized corrosion of steel can occur in the submerged regions of reinforced concrete structures in marine environments.
2. Cathodic reaction rates under oxygen diffusional limitation in the submerged region that are negligible in cases of uniform corrosion can support substantial corrosion rates in cases of localized corrosion.

3. Eliminating corrosion in the splash/evaporation zone could in some cases increase corrosion vulnerability of steel in the submerged region.
4. The passive state of a large portion of the steel can be preserved in the presence of high chloride concentration at rebar depth even if typical chloride threshold values are exceeded.
5. High concrete resistivity may promote unintended corrosion vulnerability in the submerged region by lowering the extent of beneficial macrocell coupling.
6. Sacrificial Anode Cathodic Protection (SACP) can effectively prevent corrosion initiation in the submerged zone and simultaneously provide some measure of protection for steel in the splash/evaporation zone.

1.2 Background

Reinforcing steel in the *atmospheric* portions of partially submerged reinforced concrete (RC) marine structures is susceptible to corrosion. Steel in this portion, especially in the low-elevation regions near the water level, is particularly vulnerable to corrosion due in part to the effects of evaporative chloride buildup and subsequent chloride diffusion through the concrete to the steel. When the chloride concentration near the steel-concrete interface exceeds a local threshold value, the steel depassivates and active corrosion can initiate. Corrosion of this type has been the object of substantial research and analysis for control and remediation.

In contrast, reinforcing steel in the *submerged* portions of the same structures has often been regarded as having little susceptibility to corrosion. This perception is based on recognition of not only the absence of chloride evaporative effects but also the strongly transport-limited oxygen supply for the cathodic reaction at the rebar surface.

In other words, even if chloride levels in the below-water regions reach the critical threshold, any resulting corrosion would be expected to proceed at a very low rate. Accordingly, corrosion in the submerged zone has historically received little attention.

Published literature relating to corrosion of steel in partially submerged marine structural elements is sparse; detailed examination of elements after decommissioning is apparently not often reported. One investigation, performed by Beaton et al. in the 1960s, did however specifically look for this form of damage in 37-year-old bridge pilings. Notably, that work found multiple instances of severe localized reinforcement corrosion deep in the submerged zone. More recently, reference to localized corrosion events in submerged concrete was made by Tinnea. [2012]

It should be noted that the near absence of reports of underwater corrosion might be attributed in part to both the lower frequency of inspection due to inherent access difficulties and to the fact that features like cracks and spalls can easily be hidden by deposits and marine growth. Further complicating detection is the fact that fluid corrosion products, which are more likely to develop in high-humidity conditions, may not induce telltale concrete cracking. [Torres-Acosta and Sagüés 2004, Broomfield 2007, Busba and Sagüés 2013] In this case, the absence of cracking could effectively prevent detection of substantial damage despite extensive steel cross-section loss and/or steel-concrete bond loss.

Corrosion in the submerged zone can be somewhat suppressed by galvanic coupling with reinforcing steel in the tidal and splash/evaporation zones which started corroding earlier in the life of the structure. This coupling tends to make the potential of the submerged steel more negative and this effectively elevates the corrosion threshold

and thereby retards the initiation of corrosion below water (a form of cathodic prevention). [Pedefferri 1996, Bertolini et al. 2004, Sagüés et al. 2009] If corrosion initiates in the submerged region, it could nevertheless be mitigated by the same mechanism. In both instances the extent of corrosion above water would be increased and corrosion in the submerged zone would be decreased. Thus it can be seen that successful implementation of some types of corrosion control measures for steel in the tidal and splash/evaporation zones (regions subject to repeated wetting/drying cycles and chloride accumulation) could actually decrease the extent of the aforementioned preventive/protective mechanisms for the submerged zone. In this way, the likelihood and severity of corrosion in the submerged region could be increased. In this case, corrosion in the submerged region could actually be aggravated if the non-corroding atmospheric region acts as an efficient supplemental cathode for the steel in the submerged portions of the structure.

Uncertainty as to the fate of reinforcing steel in the marine-submerged regions of RC structures led to interest in an investigation that would explore this issue further. This dissertation presents the methods and results of field assessments of aged bridges in the aggressive subtropical marine environment of Florida, steady-state modeling of the distribution of corrosion in a mature structure, dynamic modeling of corrosion progression over a complete service life-cycle, and a model-based assessment of the effectiveness of a cathodic protection corrosion control application.

1.3 Relevance and Outlook

The costs of corrosion detection, damage, and remediation are high enough to measurably affect the economies of developed countries worldwide. According to a

Federal Highway Administration (FHWA) corrosion-cost study conducted in 2002, the estimated direct annual costs of corrosion in the United States exceeded \$275 billion, a figure that amounts to more than 3% of the nation's gross domestic product. The costs of corrosion in the industrial sectors such as utilities, transportation, infrastructure, manufacturing, and government account for approximately half of the total. [Lee 2012]

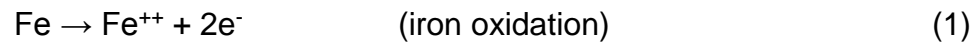
A significant part of the total cost of corrosion in the transportation and infrastructure sectors is directly related to structural maintenance, repair, and replacement necessitated by corrosion of steel reinforcing bars (rebars) used in the construction of RC bridges, dams, tunnels, etc. The FHWA study identified corrosion of steel reinforcement as the cause of structural deficiency in approximately 15% of highway bridges in the U.S. and determined that the direct annual cost of corrosion in highway bridges was approximately \$8.3 billion. Notably, the indirect societal cost (associated with things such as lost work time and extra fuel consumption from delays) was estimated to be as much as ten times this amount. [Koch et al. 2002]

Interest in the fate of reinforcing steel in submerged concrete structures in marine environments has been renewed not only by the substantial safety and economic consequences of structural failure, but also in part by increasingly ambitious structure durability expectations.

1.4 Corrosion of Reinforcing Steel in Submerged Concrete

This section provides context and terminology for the presentation of the field evidence and interpretative modeling that follows.

Corrosion of reinforcing steel in concrete may be viewed as the result of both an anodic reaction



and a cathodic reaction, usually summarized over a wide range of exposure conditions by



It is noted that hydrogen-evolving cathodic reactions are theoretically possible under extreme conditions; for simplicity and in view of additional discussion in Chapter 4, these reactions will not be addressed here.

Given the concrete's highly alkaline pore solution, reinforcing steel initially acquires a passive film that strongly limits the rate of the anodic reaction. [Bertolini et al. 2004, Broomfield 2007] Passivity breakdown can however occur if the concentration of chloride ions (from seawater) near the steel surface exceeds a critical threshold value. [Ann and Song 2007] In this case the steel undergoes active dissolution associated with a large increase in the rate of iron oxidation.

The concrete pore network of atmosphere-exposed concrete is usually not saturated with pore water. [Bertolini et al. 2004] The effective diffusivity of oxygen in the concrete is relatively high and an abundant supply of oxygen at the steel surface enables a relatively high cathodic reaction rate. The pore network of submerged concrete can however be regarded as water-saturated, in which case the diffusivity of oxygen in saturated concrete is much lower than that in dry concrete. [Tuutti 1982, Broomfield 2007] A severe diffusional limitation of the cathodic reaction occurs and an associated decrease of the corrosion rate is expected, as noted earlier. [Raupach 1996]

If corrosion in the submerged portion of a structure proceeded uniformly and if any macrocell coupling with the atmospheric portion was disregarded, the oxygen-diffusion-limited corrosion rate for a simple system with nearly one-dimensional transport, uniform concrete properties, and a steel placement density factor (i.e. ratio of embedded steel surface area to column exterior concrete surface area) equal to one would correspond to a corrosion current density

$$i_{\text{CORR}} = (D n F C_{\text{eO}}) / x \quad (3)$$

where D = effective diffusivity of oxygen through the concrete (cm^2/s), $n = 4$ (per Equation 2), F = Faraday constant, $96,480 \text{ A}\cdot\text{s} / \text{mol}$, C_{eO} = concentration of oxygen at the exterior concrete surface⁽¹⁾ (mol/cm^3), and x = concrete cover depth (cm). (Note that the steel placement density factor is often simply referred to as the steel factor, SF. A value of SF=1 is on the order of SF values typically encountered in marine bridge substructures design.) Using typical values of D and x for water-saturated concrete and marine substructure respectively, and assuming that the seawater is in equilibrium with atmospheric oxygen, the resulting values of corrosion rate (CR) for steel (after Faradaic conversion: $1 \mu\text{A}/\text{cm}^2 \Leftrightarrow 11.7 \mu\text{m}/\text{y}$) can be $< 1 \mu\text{m}/\text{y}$. [Jones 1995] Such low values would extend the corrosion propagation stage to a period of several decades assuming that critical corrosion penetration depths (χ_{CRIT}) for corrosion product-induced cracking are on the order of $100 \mu\text{m}$, a typical value encountered in atmospherically exposed concrete. [Torres-Acosta and Sagüés 2004, Broomfield 2007] Since, as noted above,

⁽¹⁾ In this dissertation (and consistent with previous modeling work [Sagüés et al. 2003]) oxygen concentration is expressed in terms of estimated oxygen content of the pore water of the concrete; the value of D is adjusted accordingly depending on the literature source used.

the corrosion products might be transported away from the corroding bar more easily in water-saturated concrete than in atmospheric-air-exposed concrete, [Liu and Weyers 1998, Broomfield 2007] the effective value of χ_{CRIT} may be even greater. Accordingly it might be expected that corrosion of reinforcement in submerged concrete under the assumed conditions would not have any important externally visible manifestation during a typical design service period, e.g., 75 years.

The circumstances and conditions described above represent the core of the argument for the traditional expectation that corrosion in the submerged zone will not be consequential, at least in the absence of adverse corrosion macrocell coupling with a more-efficiently oxygenated and non-highly-corroding atmospheric zone. If such coupling existed, uniform corrosion in the submerged zone would indeed be enhanced. It could be further argued however that the expected relatively low resistivity of water-saturated concrete and the direct external contact with a body of very low resistivity seawater would effectively diminish any adverse consequences because the aggravating effect would be dispersed over the generally large, uniformly corroding steel surface area in the submerged zone.

It is important to note that both of these arguments would only be applicable if corrosion is uniformly distributed over the entire surface of the embedded steel assembly. If active corrosion was limited to only a small fraction of the steel surface while the rest of the steel remained in the passive condition, the situation would have to be reevaluated.

In the first case i.e., no coupling with the atmospheric zone, Equation (3) would no longer be valid. Due to the prevalent low ohmic resistance conditions, substantial

corrosion macrocell action *within* the submerged zone itself could effectively couple the active regions with the rest of the passive rebar assembly and consequently could not be ignored. In this way, the cathodic current acting on a mostly passive region could be concentrated and thereby maintain high corrosion rates in a small anodic region, well in excess of the value implied by Equation (3).

If additional macrocell action was available via coupling with a strong cathodic atmospheric region, the effect would be concentrated in the locally active region, with consequent aggravation of corrosion limited to the local region instead of being applied to the entire steel assembly. Preliminary work by the author provided initial evidence supporting these propositions [Sagüés et al. 2012, Walsh and Sagüés 2014] and comparable work has received increased attention in recent years [Holland 2012, Pergola et al. 2013, Thistlethwaite 2014] indicating the desirability of more detailed investigation.

The recognition of the possible enhanced corrosion scenario described above was the focus of the examination of substructure elements from decommissioned bridges presented here. Following examination of the submerged region of marine bridge piles, further analysis was conducted via the development and implementation of a quantitative physical model based on a mechanistic interpretation of the phenomena that may lead to corrosion in the submerged region. The model was used to project the extent of corrosion aggravation in various plausible scenarios and the projections were compared with the field observations as a means of evaluating the suitability of the underlying hypotheses.

1.5 Summary of Scope and Approach

In summary, the objectives of this investigation were to determine the extent to which corrosion is present in marine-submerged substructures, the mechanisms by which corrosion could occur, and the means by which corrosion of this type could be controlled.

As detailed above, the objectives were approached via the assessment of corrosion in decommissioned field piles and the subsequent formulation of a predictive model based on the field assessment findings and basic corrosion science. The model, once formulated and validated, was also applied to the evaluation of both the possible extent of corrosion in typical marine piling in a subtropical environment and the feasibility of corrosion control by means of sacrificial cathodic protection anodes. The following chapters detail the methods, results, and conclusions drawn while following this approach.

CHAPTER 2: FIELD ASSESSMENT

This chapter describes the assessment of submerged region corrosion in decommissioned bridge piles from an aggressive subtropical service environment.

2.1 Structures and Elements Examined

Square cross-section pile specimens from three decommissioned Florida bridges were made available by the Florida Department of Transportation (FDOT). The bridges, designated here as A, B, and C, ranged in age from 51 to 66 years at the time of pile extraction. Specific details relating to the bridges and their associated pile portions are presented in Table 1.

The marine service environment of each of the three bridges contained very high chloride and each was classified as “extremely aggressive” by the FDOT.⁽²⁾[2002] Two pile portions were extracted from Bridge A (see Figures 1 and 2). The portions, which came from two different piles (designated Pile #1 and Pile #2) were subjected to detailed examination in a remote inland yard subsequent to being removed from service. Pile portions from bridges B and C (Figures 4 and 5) were visually inspected and further examined on each respective bridge demolition site. Each pile from Bridge A featured a steel reinforcement rebar cage and a central steel H-beam, which was 10 in (25 cm) wide and situated inside the rebar cage as shown in Figure 3. Each pile

⁽²⁾ Florida Department of Transportation, 5007 N.E. 39th Avenue, Gainesville, FL 32609

portion from bridge A also included a conventional repair jacket (consisting of concrete filler material and epoxy-coated rebar) that had been installed on its upper half after the pile had been in service for approximately 41 years. The pile from Bridge C had likewise been fitted with a conventional jacket at some point during its service life.

The pile portions were demolition cutouts from whole piles. Each portion included parts of both the atmospheric and submerged regions. Note that the submerged region, for the purposes of this paper, is defined as the part of the pile that extends from the bottom end of the pile up to the highest elevation of the marine-organism coated region, hereafter called the waterline. The submerged zone includes any part of the overall length below the elevation at which the pile was buried in the bottom soil, a level hereafter referred to as the mudline. The waterline can be said to be approximately coincident with the mean high-tide level in typical Florida marine locations, where the tidal span is only on the order of 2 ft (0.6 m). For this reason, the waterline was assumed to represent a simple transition between submerged and atmospheric regimes conditions for both the field assessments and modeling, recognizing that other geographic locations may require detailed treatment to account for an extended tidal zone.

2.2 Field Assessment Methods

For the Bridge A pile portions, autopsy began approximately one year after removal from service. During the intervening period, the pile portions were kept in an inland yard covered by a tarp and subjected to periodic water hosing to minimize moisture loss. Segments, 11 ft (3.3 m) long, of all corner rebars in both piles, extending from the bottom of the pile cutout up to the lower end of the pile jacket, were exposed

using saw cuts as shown in Figures 6-8. After the cuts were made, a hammer and chisel were used to crack the concrete in order to fully expose the bars (Figure 9).

After visual examination, six of the exposed corner bar lengths (2 from Pile #1, 4 from #2) were fully removed so that any decrease in the bar's cross-sectional area caused by corrosion could be quantified. Due to a number of factors including great overall length, presence of corrosion products, and irregular corrosion distribution, the amount of metal lost to corrosion for each bar was indirectly determined using a specially developed process. The process involved measuring variations in electrical resistance at fixed 5 cm intervals along the entire length of each bar and relating the measured values to cross-sectional area, recognizing that an increase in local resistance would correspond to a decreased cross-sectional area. First, small electrical contact points were made by abrading the steel surface. Next, a direct current (DC) of 10 Amperes was applied over the entire length of the bar. Finally, the potential difference was measured between each pair of contact points. The DC-related local potential difference was measured in both forward and reverse polarities and the observed values were averaged to eliminate any residual measurement bias. DC was used to avoid artifacts that develop when using alternating current due to the electromagnetic skin effect. [Perkins et al. 2005]

After determining the baseline segmental voltage difference over non-corroded regions of each bar, excursions from this baseline were quantified and converted to reflect local reduction in cross-sectional area with respect to the area of the non-corroded rebar regions. The cross-sectional area reduction was converted into an equivalent perimeter-averaged local radius loss. Making a working assumption for the

amount of time that the corrosion had been in progress during the service life of the piles, the radius loss was subsequently converted to an effective, time- and perimeter-averaged corrosion rate.

Concrete resistivity was measured on the freshly cut surfaces of the pile concrete using a C.N.S. RM MkII four-point Wenner array probe with 2.5 cm probe spacing. Thirteen resistivity measurements were recorded and then averaged. Concrete specimens were collected for determination of both bulk porosity (per ASTM C 642 [ASTM 2006]) and chloride content (per FM 5-516 [FDOT 2010]). In both cases, multiple specimens were collected and tested so that reproducibility of results could be established. Phenolphthalein was applied to fresh cut concrete surfaces to assess the degree of carbonation.

For the Bridge B pile portion, autopsy was performed under field conditions (see Figures 10 and 11) and was limited to a single corner of the pile, exposing only one of the 20 steel strands in the cross-section by cutting the concrete in a manner similar to that used on Bridge A (see Figures 12 and 13). The pile section had been removed from the bridge less than three days prior to the autopsy and had been laid on its side on a barge. The single strand was effectively exposed between the pile's mudline and an elevation approximately 2 ft (0.6 m) below the waterline. The strand was visually inspected and the strand cross-section loss was estimated. Concrete resistivity was measured with the same instrument and technique used for the pile from Bridge A; observed Bridge B values were likewise averaged. Concrete porosity and chloride content specimens were also collected and evaluated according to the same procedures used for Bridge A. Additional concrete specimens were collected for pore

water pH assessment which was made using the in-situ leaching (ISL) method. [Cáseres et al. 2006]

For the Bridge C pile portion, an autopsy of a completely demolished pile was conducted on-site. The entire rebar cage was exposed for examination as shown in Figure 14. Pile demolition and reinforcing steel inspection took place immediately after the pile was pulled out of service. After a thorough visual inspection was made, a corroded steel specimen was cut from the rebar cage. The specimen was transported to the laboratory for direct corrosion penetration measurement using a dial caliper; the cross-section loss was subsequently estimated.

2.3 Field Assessment Results

2.3.1 Bridge A: Skyway Fishing Pier

The inspection revealed significant localized corrosion in the parts of the submerged regions that were examined. None of the four exposed corner bars in Pile #1, including the two bars that were fully removed from the pile, showed any conspicuous corrosion. In contrast, three of the four corner bars from Pile #2 (all removed for detailed examination) showed substantial localized corrosion and associated cross-section loss. The corroded regions showed the greatest metal loss on the side of the bar closest to the outer concrete surface, while the inward-facing side (toward the bulk of the concrete) showed little or no corrosion. It is particularly notable, considering the pile service life of approximately sixty years, that after removing concrete residue from the steel bars, the original dark mill scale was visible and apparently undisturbed on the bar surface in regions distant from localized corrosion.

Figure 15 (left) shows typical in-place appearance of the localized high corrosion regions of one of the Pile #2 bars (which was designated as Bar #2b). The picture was taken immediately after the bar was exposed and all loose concrete and corrosion products were removed. Figure 15 (right, in this case Bar #2c) illustrates the abundant corrosion products typical of those seen in the regions of localized corrosion.

The corrosion products associated with some of the affected regions appeared to have spread into cracks, possibly corrosion-induced, that radiated from the bar. Notably however, some corrosion product penetration into the bulk of the concrete near the bar was also apparent. Figure 16 shows locally corroded regions on Bar #2a, as seen shortly after bar extraction, and illustrates the considerable metal loss (as much as several mm in depth and representing nearly 30% of the cross sectional area; see Table 1), which was concentrated on the side of the bar facing the external pile surface.

Typical electric resistance measurement raw data are presented in Figure 17. Corrosion rate estimates and distribution profiles based on the electric resistance measurement data are shown in Figure 18. As mentioned above, the perimeter-averaged metal loss was converted into a time-averaged corrosion rate over a nominal timespan. Assuming that the corrosion had started early in the pile's service life due to high concrete permeability (reported below) or possibly local concrete deficiencies, the timespan was approximated as being equal to the pile's service life i.e., 60 years. The resulting perimeter-averaged values for the corroding regions typically ranged from 5 to 35 $\mu\text{m}/\text{y}$. The lengthwise locations of the peaks for estimated corrosion rate (shown in Figure 18) corresponded directly to the regions of visually observed severe corrosion such as that in Figure 16. As can also be seen in Figure 18, the length of the each

localized corrosion regions on the bars removed from Pile #2 typically measured between 4 and 8 in (10 to 20 cm) long, without any apparent preferential elevation location within the pile depth range sampled. It should be noted that equipment limitations precluded extracting or even accessing the rebar segments in the regions where the original piles were covered by the jackets.

The combined length of conspicuously corroded bar segments is listed in Table 1 in addition to the total length of rebar directly examined in both piles. The ratio of corroded-length to total-length is also provide in the table, and can be seen to amount to only approximately 6% of the total rebar length directly surveyed. The rebar stirrups, visible in Figure 15, were not part of the assessment but could be assumed to have shared an overall proportional incidence of corrosion. The H-beam was not included in the assessment either, as the examination focused on steel closest to the external pile surface and thus subject to the most aggressive conditions.

Concrete resistivity ranged from 3.31 to 4.97 k Ω -cm (see average in Table 1). Such low values are typical of high-permeability concrete when saturated with seawater and they are consistent with values expected in the class of concretes (with unblended cement) that was typically used in FDOT pile applications at the time of construction. [Sagüés et al. 1997] As indicated in Table 1, porosity was also quite high.

Two concrete cores from each of the piles were extracted for chloride analysis. One core from each pair was taken from a position at an elevation of approximately 1 ft (0.3 m) above the mudline and the other core taken from a position at an elevation approximately halfway between the mudline and the waterline i.e., 8 ft (2.4 m).

Results (Table 2 and Figure 19) indicate that after the 60-year service period the concrete had reached a state of near chloride saturation in the region between the outer concrete surface and the rebar. The concrete chloride content is on the order of that expected given the observed concrete porosity, the chloride content of the seawater, and a presumed typical amount of chloride binding by the cement paste. [Cáseres et al. 2006] The nearly flat chloride concentration profiles are also consistent with those expected given the time-in-service and the typical chloride ion diffusivity value (on the order of 10^{-7} cm²/sec) of concrete associated with the low resistivity values reported earlier. (Note that a description of methods and results for a preliminary chloride content assessment is presented in Appendix A.)

Phenolphthalein solution sprayed onto the freshly cut concrete surfaces in the exposed rebar region resulted in solid purple coloration on the entire surface. This result indicated, as expected for submerged concrete [Sagüés et al. 1997] that no discernible carbonation of the concrete had taken place near the pile surface during the pile service life or after extraction during the pre-autopsy period when the piles were frequently wetted. (Note that a description of methods and results for a Bridge A pile potential map survey are presented in Appendix B.)

2.3.2 Bridge B: Pinellas Bayway Drawbridge

Corrosion in the submerged zone was also observed in the pile portion of this structure. Most of the exposed strand was free of visible corrosion but five segments typically ~10 cm long showed evidence of reduced cross-sectional area in some of the individual strands. A distinct rust-color was visible in the concrete near each corroded strand segment, as shown in Figures 20 and 21. The segments were located at

elevations approximately 52, 71, 95, 112, and 138 in (1.3, 1.8, 2.4, 2.8, and 3.5 m) below the waterline with no clear preferential elevation location. No locations below the mud line were surveyed due to on-site time and equipment constraints. The observed corrosion affected approximately 12% of the total length of strand examined.

Concrete resistivity measured on the freshly cut surfaces of the submerged region ranged from 1.8 to 3.5 k Ω -cm. Concrete porosity was 13%. The resistivity values and the porosity of concrete in the seawater-saturated condition are comparable to those of Bridge A and similarly indicative of high-permeability concrete, again consistent with the construction-era practice. [Sagüés et al. 1997] For verification of expected trends, resistivity values were also obtained for a region on the pile surface at an elevation of 8 ft (2.5 m) above the waterline. The results ranged from 31 to 47 k Ω -cm (average 38 k Ω -cm), consistent with the expectation of higher resistivity when the concrete is drier and consequently having lesser electrolytic connectivity.

Concrete chloride content measurements were performed at two elevations. In each case chloride content was measured near the concrete surface and also near the strand trace, with duplicate specimens in both cases (see Figure 22). Results (Table 3) show, as in the case of Bridge A, high levels of apparent chloride penetration and a nearly flat chloride profile, typical of concrete with a high chloride diffusivity. This behavior is consistent with expectations for highly permeable concrete, this being presumed given the resistivity and porosity results.

For pore water pH evaluation, one specimen each was prepared using concrete fragments from two locations at elevations of ~2 ft (0.6 m) and ~16 ft (~3 m), below the

waterline. ISL test results (average of three measurements in each case) indicated pore water pH of approximately 12.5 in both specimens.

2.3.3 Bridge C: Sunrise Key Bridge

As shown in Figure 14, most of the embedded reinforcing steel in the submerged region was corrosion-free and had presumably remained in a passive condition through the entire time-in-service (~60 years). Evidence of severe corrosion below the waterline was however present in one region of one vertical bar (see Figure 23). The highest loss of cross-section of the bar was estimated to be 23%. The affected region was approximately 10 in (0.25 m) long and was located at an elevation of approximately 10 ft (3 m) below the mudline. The total steel surface area below the waterline per pile was estimated to be 10 ft² (~0.9 m²) and the total surface area of the corrosion-affected region was estimated to be 0.14 ft² (~0.013 m²), or about 1.4% of the total submerged steel surface area. Note that the rebar in the splash/evaporation zone (i.e., the region near the waterline subject to repeated wetting/drying cycles and evaporative chloride buildup effects) of several of the piles of this bridge was severely corroded (see Figure 24). No concrete property data were obtained from this bridge but given the estimated date of construction, it is assumed that permeability was high and comparable to that of the other two bridges.

2.4 Field Assessment Findings and Discussion

The field examinations addressed a sparsely documented issue and ultimately revealed severe localized corrosion in the submerged zone of several piles, thus substantiating some of the concerns indicated in the introduction. The observed

corrosion was not limited to regions in close proximity to the waterline but was also found in the submerged regions, including elevations below the mudline.

The chloride content at the steel depth in the pile portions examined was high, averaging 29 lb-yd⁻³ (17.2 kg·m⁻³). This high value is indicative of the high-permeability concrete used in this era [Presuel-Moreno et al. 2005] and it amply exceeded the typically accepted corrosion threshold value that plain steel exhibits when in the passive state and at potentials typical of atmospheric exposure. [Presuel-Moreno et al. 2005, Sagüés et al. 2014, Sánchez and Sagüés 2014a].

Given the high concrete permeability of the cases considered here, the high chloride concentrations at cover depth were likely to have been reached quite early in the service period of the piles, consistent with the nearly flat chloride profiles encountered on autopsy. Despite the high chloride levels, submerged-region steel which was exposed for examination was generally free of any severe corrosion except for the localized strongly corroding regions affecting typically only about 10% of the examined steel length. That observation agrees with the expectation, detailed in the introduction, that the average rate of corrosion below the waterline would be very small due to limited oxygen transport to support the cathodic reaction. While the overall average was low, the corrosion rate was clearly very high in the small fraction of the surface where corrosion occurred.

The results of the pile examinations effectively parallel the results of the limited number of other investigations of corrosion of steel in submerged concrete. Beaton et al. reported “heavy corrosion” in the submerged region of eight out of 17 bridge piles. [1967] As in the present cases, corrosion in that investigation was found to be highly

localized; maximum penetration depths ranged from 0.117 to 0.260 in (2.9 to 6.5 mm) for spots with lengths up to ~6 in (15.2 cm), comparable in scale with the present observations. Beaton also observed high chloride concentrations at the steel depth, averaging 25 lb-yd⁻³. Tinnea's investigation of steel reinforcement in a salt water aquarium also revealed severe corrosion, including full-depth penetration (i.e., 100% cross-section loss) of rebar steel near local deficiencies of a holding tank wall. [2012] A related examination conducted by the author (see Appendix C) revealed an instance of localized corrosion in an epoxy-coated rebar at a concrete crack location in a normally submerged pier footer chamber. The footer had been in service for approximately 30 years at the time of the examination. While in this particular case the cathodic reaction over much of the rest of the rebar assembly was likely impeded by the presence of the epoxy coating, the combined effect of many small imperfections in the coating might have supplied appreciable cathodic current when aggregated over the very large area of the same structural element. Of special interest in this case was the fact that the concrete was sound (i.e., not cracked or otherwise damaged) and was much less-permeable (as indicated by high observed resistivity values of ~28 kΩ-cm [Sagüés and Walsh 2015]) than the concrete in the piles examined in the field assessments.

The findings from the various field sources are consistent with the hypothesis, noted in the introduction, that the effect of the small but finite cathodic reaction taking place on the entire submerged region (plus any additional coupling to cathodic regions above water) can be enough to sustain appreciable anodic activity over small regions. This effect would be facilitated if electrolytic coupling was made more efficient by a low-electric-resistance path between anodic and cathodic regions. As shown in the next

section, the highly conductive seawater forms much of that path, though some of the path is formed by the concrete itself. The concrete in the present piling cases exhibited low resistivity values, near the low end of the range typically reported for reinforced concrete. [Bertolini et al. 2004] This would also facilitate effective coupling. As noted above however, localized corrosion in the submerged region may still take place with higher bulk concrete resistivity. The complicated role of resistivity is discussed in greater detail in Chapter 4.

In summary, results of the field assessments indicated that severe localized corrosion of steel can occur in the submerged portions of reinforced concrete structures in marine environments. Reinforcing steel from piles of decommissioned marine bridges showed multiple instances of strong corrosion localization and appreciable local loss of steel cross-section. The observed patterns were consistent with observations made in an earlier exploratory investigation.

The following chapter establishes, in the light of the field findings, a quantitative description of the extent of localized corrosion that may take place and the condition of the steel surface responsible for that behavior.

Table 1. Structure assessment data.

Bridge Designation	A	B	C
	Skyway Fishing Pier	Pinellas Bayway Drawbridge	Sunrise Key Bridge
FDOT bridge number	139002	150050	865725
Water chloride content (ppm)	18,504 ¹	19144 ²	20,000 (est)
Bridge construction date	1952	1962	1949 (est)
Element assessment date	2011	2013	2015
Age at time of assessment (years)	59	51	66 (est)
Structural element type	Square Pile	Square Pile	Square pile
Element size (cross section, in x in / m x m)	20 x 20 / 0.6 x 0.6	22 x 22 / 0.65 x 0.65	12 x 12 / 0.3 x 0.3
Number of piles assessed	2	1	1
Steel reinforcement type	#8 rebar / 2.54 cm diam.	0.5 inch / 1.26 cm prestressing strand	#5 rebar / 1.59 cm diam.
Number of reinforcement elements in cross section	8	20	4
Submerged length of each pile portion (linear ft / m)	19 / 5.8	23 / 7.0	17 / 5.2
Pile length below mudline (linear ft / m)	1.5 / 0.5	7 / 2.1	13 / 4.0
Length of submerged steel (linear ft / m)	304 / 93 ³	460 / 140	68 / 21
Length of submerged steel directly examined (linear ft / m)	88 / 26.8 ³	14 / 4.3	68 / 20.7
Fraction of submerged steel length directly examined	0.29	0.03	1
Length of examined submerged steel exhibiting corrosion (linear ft)	5.25 ³	1.7	0.83
Fraction of examined submerged steel length exhibiting corrosion	0.06	0.12	0.012
Maximum corrosion penetration depth observed (in / mm)	0.082 / 2.1	.04 / 1.0 (est)	0.08 / 2.0
Maximum local corrosion-related cross sectional area loss (%)	29	20 (est)	23
Maximum depth below waterline of observed corroded region (ft / m)	18 / 5.5	12 / 3.7	13 / 4.0
Average cover depth (in / cm)	3 / 7.6	3.1 / 7.9	3.5 / 8.9
Average concrete resistivity in submerged region (kΩ-cm)	4.2	2.6	-
Concrete porosity (%)	16	13	-
Maximum measured concrete chloride concentration at reinforcement depth (lb x yd ⁻³ / kg x m ⁻³)	23 / 13.6	36 / 21.4	-

1 [FDOT 2002]

2 [FDOT 2015]

3 Total for both piles; nominal amount disregarding H-piles and stirrup steel.

Table 2. Chloride content of Bridge A pile core slices.

		Chloride Content [pcy]			
		Pile #1 (west pile) (source of bars 3 & 4)		Pile #2 (east pile) (source of bars 1, 2, 5, & 6)	
Slice	Depth of midpoint [in]	Core #1 (1' above mud line)	Core #2 (8' above mud line)	Core #3 (1' above mud line)	Core #4 (8' above mud line)
A	0.25	17.1	18.9	21.1	24.7
B	0.75	14.3	20.5	18.5	23.2
C	1.5	16.2	22.5	23.4	25.6
D	2.5	14.6	21.7	22.9	22.5
E	3.5	15.7	22.7	19.5	20.7
F	4.5		21.4	17.0	
G	5.25			17.7	
H	5.75			17.0	

Table 3. Chloride content of Bridge B specimens.

Location	Average Cl Concentration lb/yd ³ (kg/m ³)	
	Near Concrete Surface	Near Strand Trace
16' BWL	30.3 (18.0)	34.1 (20.2)
2' BWL	22.4 (13.3)	26.3 (15.6)



Figure 1. Bridge A piles resting side-by-side on horizontal concrete columns. Note jackets on upper area (left) of piles and H-beams visible at each pile bottom end (right).

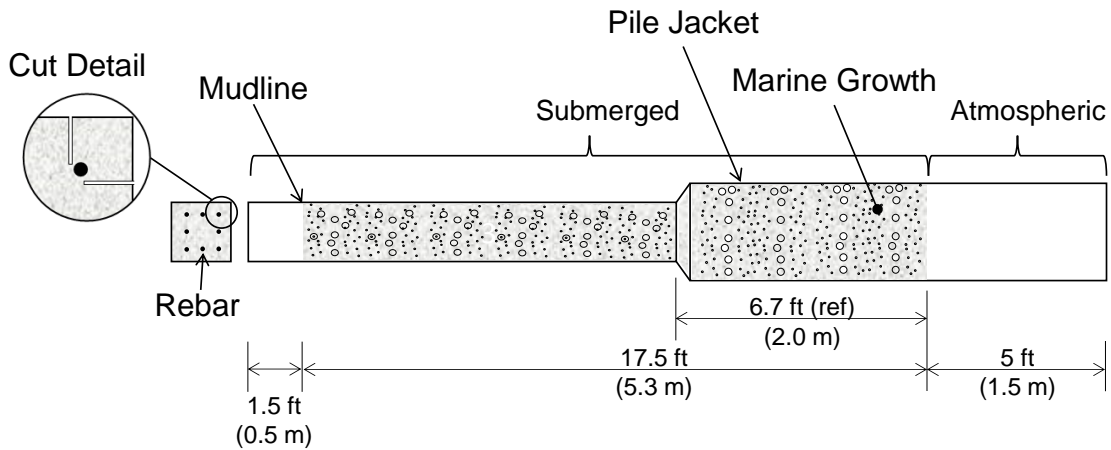


Figure 2. Typical configuration and dimensions of Bridge A piles. (Skyway Fishing Pier) Note indicated jacket length below the waterline (BWL).



Figure 3. Bridge A piles, end view. Note marine organisms and muck accumulation on each pile's exterior surface everywhere except region below the mudline (foreground).

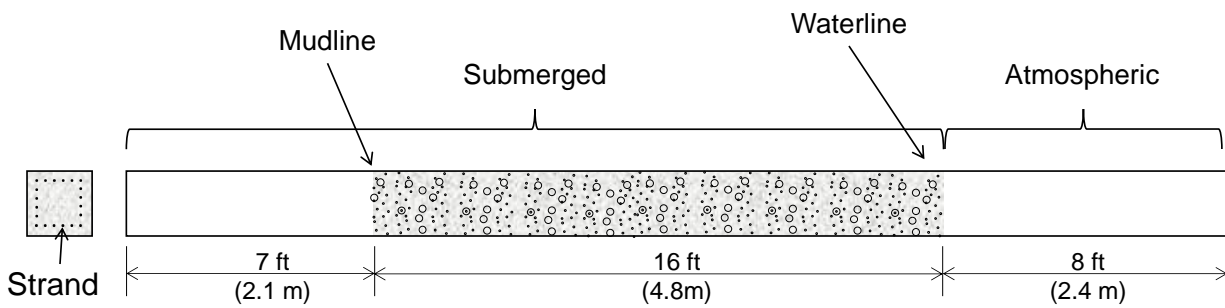


Figure 4. Typical configuration and dimensions of Bridge B piles.

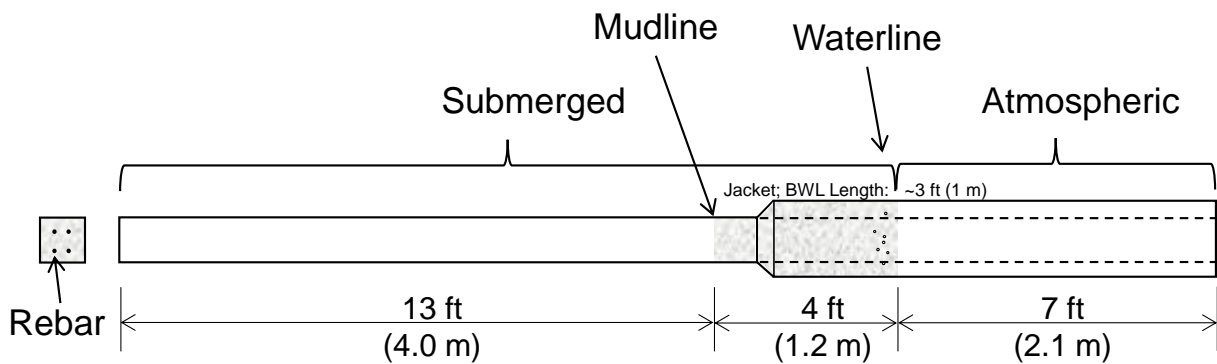


Figure 5. Typical configuration and dimensions of Bridge C piles.

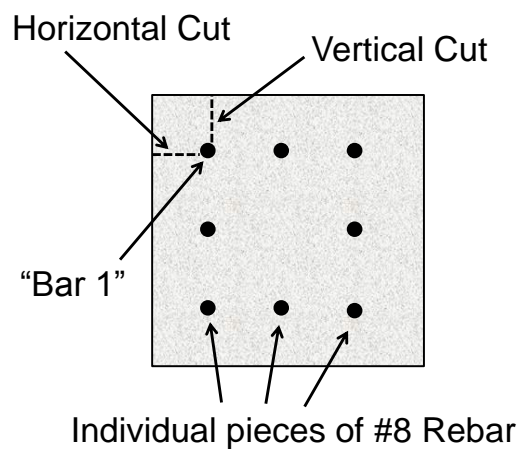


Figure 6. Cross-section of Pile #2 showing vertical and horizontal saw cuts. H-beam not shown.

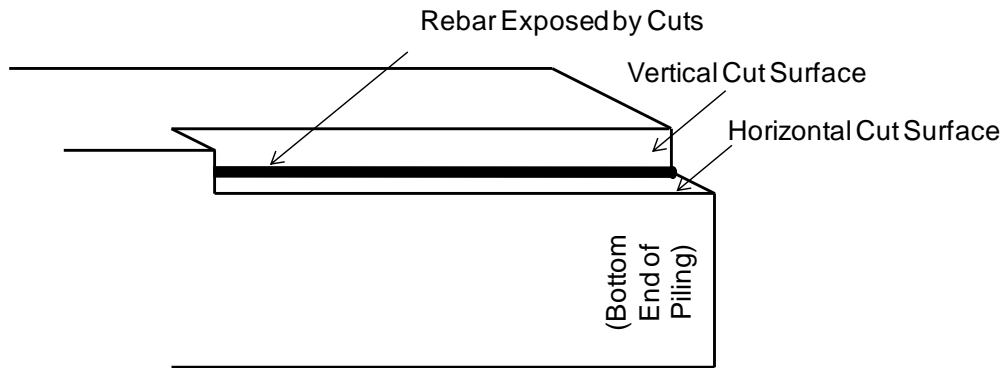


Figure 7. Schematic diagram of vertical and horizontal saw cuts. (not to scale)



Figure 8. Actual vertical and horizontal saw cuts. (Bridge A Pile #2)



Figure 9. Rust stains in concrete cover observed during bar removal. (Bridge A Pile #2)



Figure 10. Submerged (i.e., bottom) end of pile from Bridge B, end view. Note that the absolute bottom end of the in-service pile was left in situ and that this pile portion was cut from it.



Figure 11. Bridge B pile selected for autopsy. Atmospheric air-exposed end of pile (i.e., top) is in the foreground. Note marine growth between waterline and mudline.



Figure 12. Submerged end of another pile from Bridge B. Note that marine growth has been scraped from the surfaces near the corner to facilitate saw cuts.

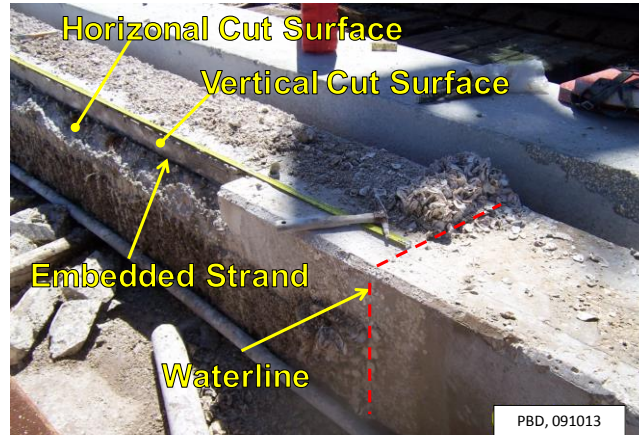


Figure 13. Autopsied Bridge B pile. Note concrete chunks on deck removed from pile with a hammer and chisel after vertical and horizontal saw cuts were made.



Figure 14. Corrosion-free steel in much of Bridge C submerged region. Note that pile in photo was lying on its side.

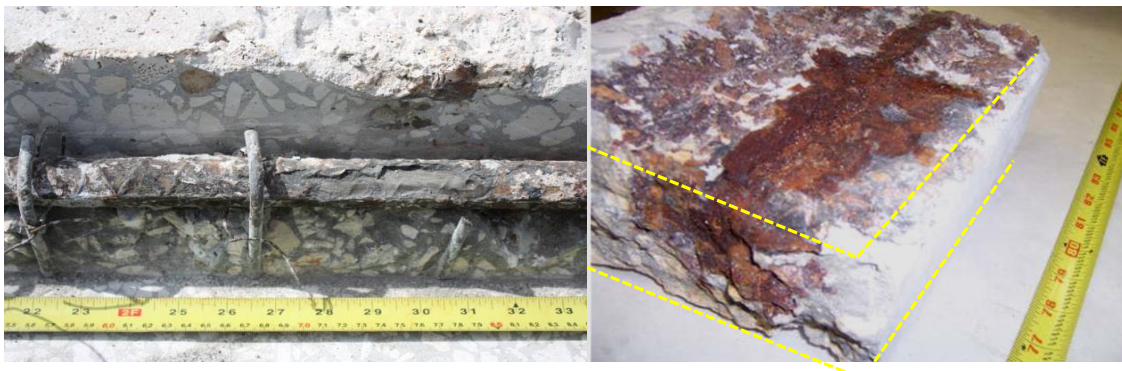


Figure 15. Corroded rebar. Left: Bridge A rebar in-situ showing localized corrosion following the removal of the concrete; Bar #2b, Location: 17ft (5 m) below waterline. Right: Corrosion products spreading far from a localized corrosion spot. Top and bottom dashed lines indicate rebar placement plane and external pile surface plane respectively; Bar #2c, location: 10ft (3 m) below waterline. Bar diameter: 1 in (2.5 cm).



Figure 16. Severe localized corrosion-related cross-section loss, Bridge A. Corrosion was limited to relatively short segments of the bar length and in each segment most of the metal loss took place on the side of the bar facing the external pile surface (top of each picture). Bar #2a; locations from left to right: 140 and 175 in (3.6 and 4.4 m) below high tide, respectively. The rebar is 1 in (2.5 cm) in diameter.

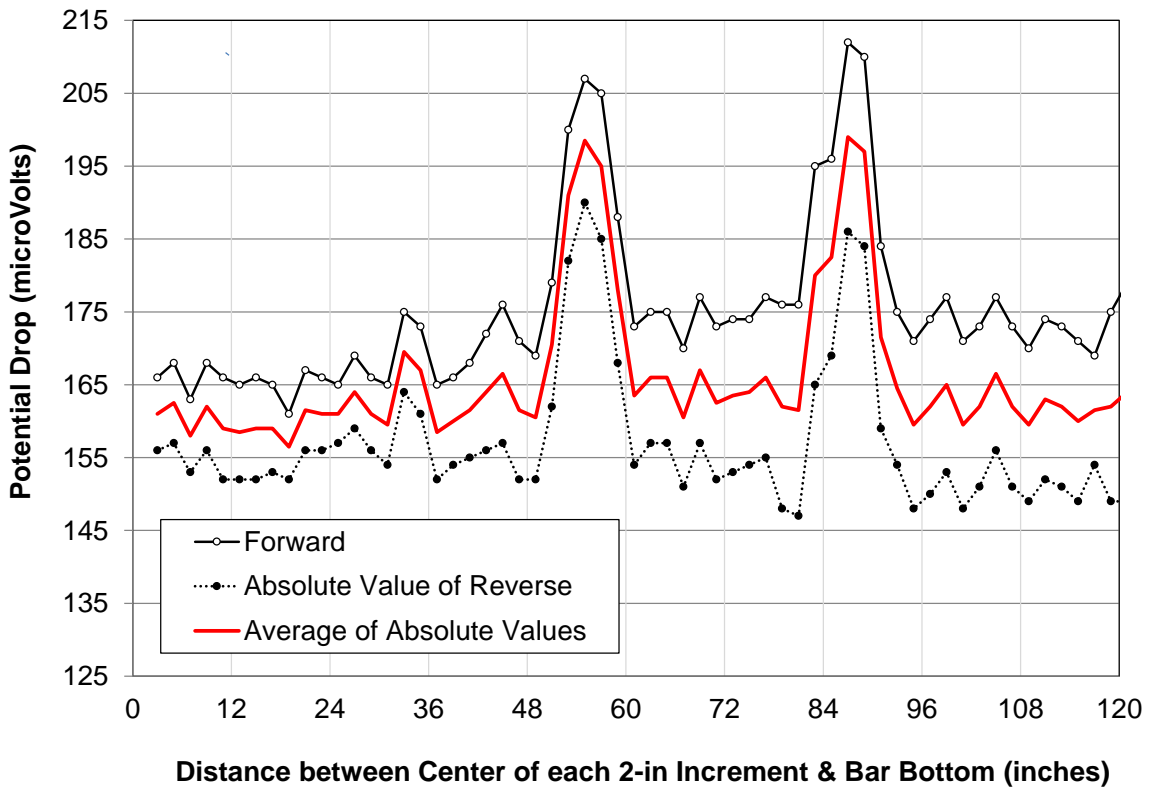


Figure 17. Cross-section loss survey. Voltage drop at 2-inch intervals along the length of Bridge A, Pile #2, Bar #2a with DC current of 10 amperes.

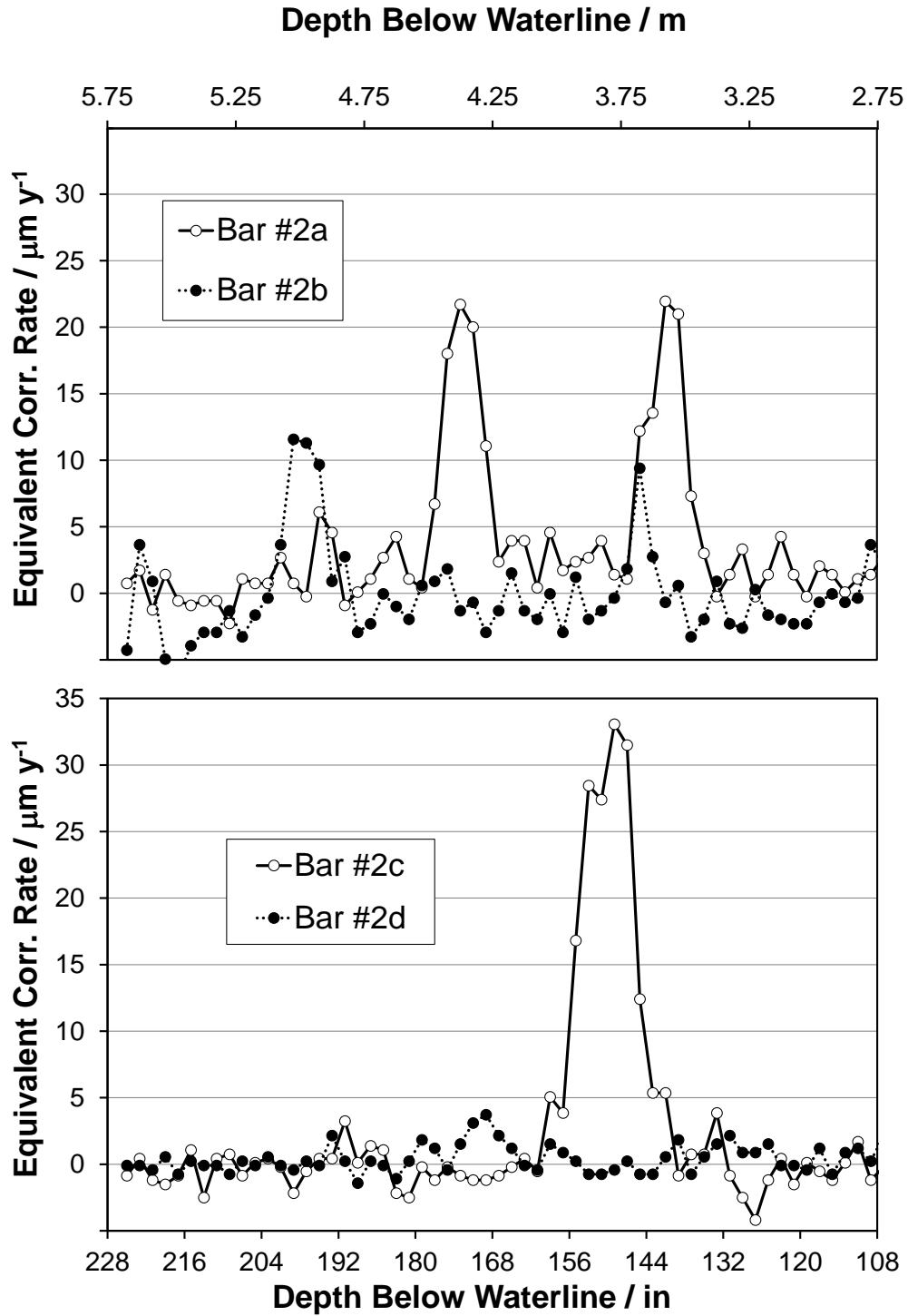


Figure 18. Estimated perimeter-averaged local corrosion rate. Rate was time-averaged over a nominal 60-year span. (Bridge A, Pile #2)

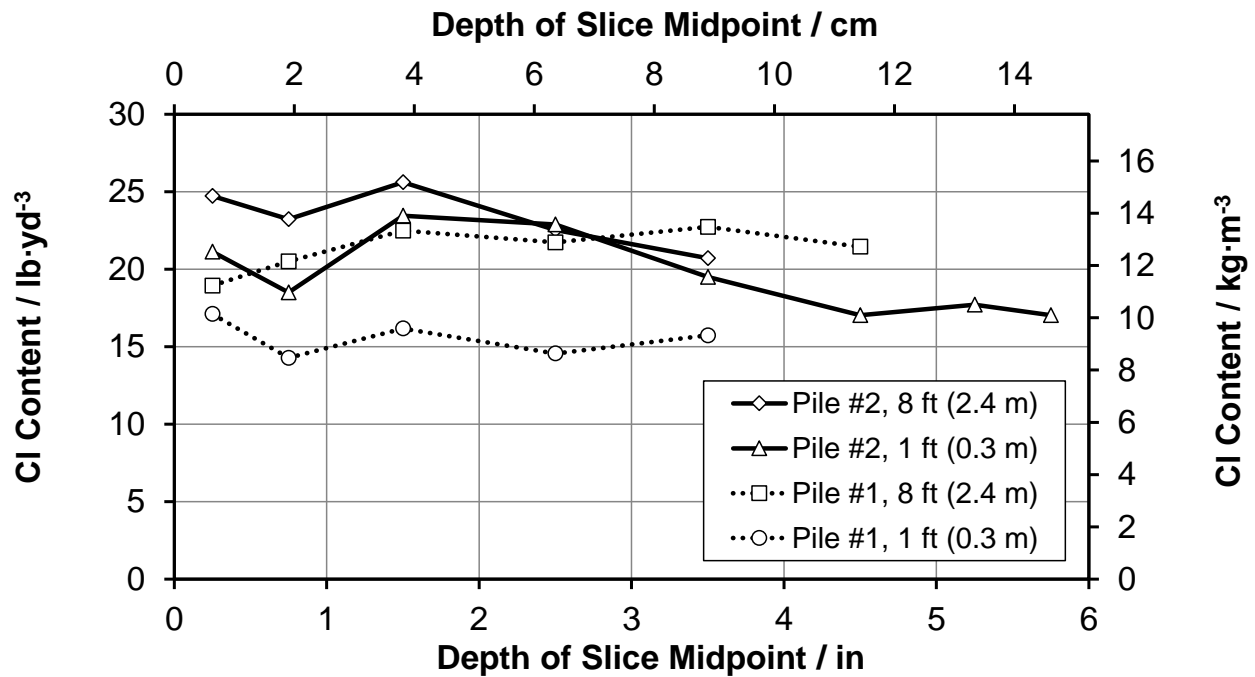


Figure 19. Chloride content as a function of depth from concrete surface. Cores taken from Bridge A piles, at indicated depth above the mudline



Figure 20. Exposed strand in region nearest waterline of autopsied pile. (Bridge B) Note rust-colored regions. (Photo taken immediately after strand was exposed.)



Figure 21. Three different instances of localized corrosion. (Bridge B) Note that the measurement datum for the indicated distances was the waterline.



Figure 22. Concrete fragment mounted on mill table. (Bridge B) Note that the measurement datum for the indicated depth was the waterline of the in-service pile.



Figure 23. Locally corroded steel in region below mudline. (Bridge C) Note corrosion-related cross-sectional area decrease of bar near top of photo.

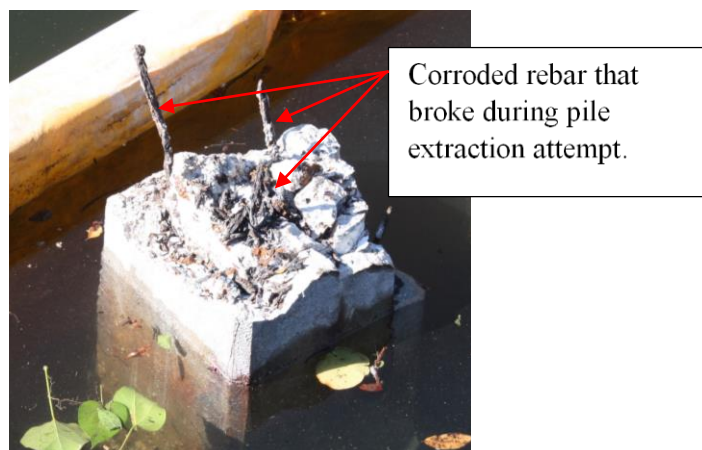


Figure 24. Bottom half of pile left in place. (Bridge C) Note visible rebar corrosion and section loss in splash zone that resulted in pile breakage during extraction attempt.

CHAPTER 3: STEADY-STATE MODELING

This chapter describes the development, implementation, and output of a partially submerged bridge pile model that projects steady-state oxygen and potential distribution within the pile, in addition to corrosion rate for embedded active steel.

3.1 Steel Surface Condition in the Submerged Zone

The results of the field assessments indicated that a small portion of the examined steel had experienced severe corrosion while the majority of the steel had not experienced any appreciable corrosion. It can be supposed that the steel that did not show appreciable corrosion must have been either in the active condition and corroding at a very low rate or in its initial passive condition despite the presence of high chloride content on its surface.

To accept the proposition that all submerged steel was in the active condition but corroding at different rates, it would be necessary to explain how the corrosion rate could be so much greater (and sustained over long periods) in some regions than it is in others when no protective film is present in either. One way to explain this phenomenon would be to propose a scenario in which the corroding regions are associated with local concrete deficiencies, such as cracks [Sagüés et al. 2014, Lau et al. 2010] that somehow (e.g., by allowing faster removal of iron ions from the corroding region) enhance the rate of the anodic reaction compared to that of the rest of the steel surface.

Alternatively the phenomenon could be explained by proposing that the stabilization of the local corrosion pattern is facilitated by migration-enhanced chloride ion accumulation (to balance the ejection of positive metal ions at the anodic region) and local pH depression by associated hydrolysis, [Fontana 1987] both processes acting to somehow strongly increase the anodic reaction rate over that of a likewise active region elsewhere. Neither of these explanations provides however an indication as to how or why the corrosion rate over the majority of the steel would be dramatically smaller than that in the affected region even in the presence of severe chloride contamination.

It could be proposed that the suppression of corrosion in the majority of the steel was enabled by macrocell coupling to the severely corroding regions, which would negatively polarize the steel in the rest of the steel assembly. However, such coupling would still leave the less-corroding regions at a potential less-negative than that of the more-corroding spots, so for a given exchange current density of the anodic reaction, the former would be the ones corroding faster, which was not the case. It would be necessary then to invoke mechanisms (as exemplified above) strong enough to yield a dramatically higher anodic reaction rate for a given potential at one set of active steel regions, than for other regions that are at an even more positive potential. These conditions constrain the plausibility of this explanation.

To accept the second proposition, i.e., that passivity was preserved over much of the submerged region, it would be necessary to explain how some regions of the rebar assembly were passive while other regions were not able to retain their initial passive character. The concept of chloride threshold dependence on local potential can provide

such an explanation. In this interpretation, before significant chloride buildup at the steel cover depth, the steel assembly is in the passive condition. The steel potential is at a value not very different from that of steel in an atmospheric regime, as the overall anodic reaction occurs at the very slow rate associated with anodic passive dissolution, hence demanding very little oxygen and resulting in a relatively elevated (nobler) mixed potential value. [Sagüés et al. 2003] As time progresses, chloride buildup at one given spot on the steel assembly causes the chloride threshold to be exceeded there. Given the prevalent value of the potential, the threshold value would be comparable to that of atmospherically exposed concrete. [Sagüés et al. 2014] The event localization could be attributed to a variety of causes, which may include but not limited to a local concrete deficiency or slightly faster local chloride transport, somewhat greater surface chloride at the concrete surface near that spot, lower local threshold due to variability in the steel-concrete interface, and combinations of these circumstances. As a result of the local activation, the corrosion rate there would increase dramatically over the original passive dissolution rate, with the rest of the assembly remaining in the passive condition. That arrangement promotes local chloride buildup and acidification by the mechanisms noted above, but also promotes a pronounced drop of steel potential that would also affect the rest of the steel assembly to an extent and distance from the spot that depends on the steel polarization characteristics of the steel and on the extent of electrolytic coupling possible. That potential drop would have the effect of increasing the chloride threshold of the still-passive steel as in a classic cathodic prevention scheme, [Pedferri 1996, Presuel-Moreno et al. 2005, Sagüés et al. 2009, Sagüés et al.

2014, Sánchez and Sagüés 2014a] thus stabilizing its passive condition so the corrosion rate remains low.

Conversely, corrosion at the active steel would be aggravated by this coupling (in addition to seeing adverse changes in the local chemical composition noted above) as it elevates the local potential, increasing the rate of the anodic reaction. The small corroding region / large passive zone configuration would thus be stable, a condition consistent with the observed behavior.

As time progresses, chloride penetration from the outside and its consequent buildup at the steel surface would increase. If the chloride concentration becomes high enough, it may exceed the previously increased threshold elsewhere and consequentially new corroding spots may eventually appear. These new spots will nevertheless tend to slow down the development of yet other active corrosion locations on the rest of the steel assembly, resulting in a prolonged nearly stable state where corrosion is still limited to a relatively small fraction of the steel assembly.

The second proposition is deemed more plausible and is examined further in the next section by means of a corrosion distribution model that simulates a late, nearly steady-state localized corrosion in an aged pile or column resembling those from the field assessments. The identification of a sequence of events leading to the development of that pattern is addressed in Chapter 4 to provide further insight as to the process and to examine possible corrosion control by means of cathodic protection.

3.2 Steady-State Model Assumptions and Configuration

A notional partially submerged cylindrical steel-reinforced concrete column was modeled using a Finite Element Modeling (FEM) two-dimensional axisymmetric

geometry in COMSOL Multiphysics⁽³⁾ Version 5.0. Some of the specific system dimensions, parameter values, and variation schemes were chosen to match those of similar previously modeled systems [Kranc and Sagüés 1994, Sagüés et al. 2014, Sánchez and Sagüés 2014a] to facilitate accuracy and consistency verification checks. The final arrangement nevertheless effectively captured the essential representative conditions of piling in a marine environment, so the insights derived are applicable to the issues at hand.

The column had a 0.525 m radius and 12 m height. The rebar cage was simulated by an arrangement of horizontally oriented interconnected hoop elements made of 0.02 m diameter bars vertically separated by 0.063 m on center (see Figure 25). The close spacing was chosen to obtain $SF=1$, a typical value as noted earlier. Clear cover depth was 0.075 m. The waterline was placed at the midpoint of the total height, elevation $z = 6$ m. For simplicity, vertical bars or similar features not suitable for full rotational symmetry representation were not included. Thus, while simulation of corrosion localization to extremely small portions of the steel was precluded, examination of the effects of small percentages of active surface such as those encountered in the field was nonetheless reasonably enabled.

Following the approach detailed in previous work, [Kranc and Sagüés 1994] the half of the column above the waterline including the top end was regarded as having an electrically insulated surface and the lower submerged half was regarded as having a surface with a single floating potential, given its direct contact with relatively high

⁽³⁾ Trade Name.

conductivity seawater. For simplicity, the bottom end of the column was regarded as an electrically insulated surface. For conservation of charge, the net electrolytic current integrated on the rest of the submerged surface was set to zero.

The resistivity of the concrete and the oxygen diffusion coefficient of the modeled concrete were set at elevation-independent values below the waterline, reflecting the assumption that the concrete in this region was uniformly wet (see Figure 25). For the region above the waterline it was assumed that increasingly drier conditions with elevation led to both higher concrete resistivity and oxygen diffusivity. As in previous work [Kranc and Sagüés 1994] both the resistivity and the logarithm of the oxygen diffusivity were made to vary linearly with height above the waterline as indicated in Figure 25. For simplicity, oxygen flow through the top and bottom surfaces of the column was not allowed.

Oxygen concentration at all points on the column's exterior surface, C_{eO} was assigned a constant value of 0.3 mol/m^3 , consistent with concentrations observed in warm seawater at near-surface depths. [Shifler and Aylor 2005] For simplicity, oxygen depletion beneath biofilms or marine growth was not represented in the model though depletion was regarded as possible and was deemed to merit consideration in future work. Also unresolved but likewise meriting consideration are the implications and effects of marine barnacle adhesion to the concrete surfaces. Marine barnacles, which covered much of the submerged surface of the piles from Bridges A and B, (see Chapter 2) can effectively change oxygen conditions in the concrete beneath the organism footprint. The presence and concentration of oxygen in the concrete (which serves as the substrate for the adhered barnacle shell) may depend on the complicated

oxygen balance evolution in the barnacles' mantle cavities. [Davenport and Irwin 2003] Various interpretations of the actual conditions have been proposed. Early work by Eashwar et al. [1992] suggested anoxic conditions beneath the footprint (in the case of decomposing dead barnacles) while later work by Sangeetha et al. [2010] suggested oxic conditions.

It should be noted that even if oxygen supply below the waterline was strongly limited, macrocell coupling between the atmospheric and submerged regions of an actual column could still facilitate the initiation and propagation of corrosion, as mentioned in Chapter 1, suggested by others, [Sagüés et al. 2003, Pergola et al. 2013, Thistlethwaite 2014] and further addressed below. The model assumes, also for simplicity, that the steel concrete cover has not experienced degradation severe enough to substantially change the average transport properties of species through that domain. This simplification should also be addressed in future treatments.

The entire surface of each individual rebar loop was designated as passive or active, according to the specifications of various simulation scenarios described below. Polarization behavior for active dissolution and oxygen reduction was determined by a simplified adaptation of Butler-Volmer kinetics as in previous work [Kranc and Sagüés 1994] and is described below.

For the anodic reaction on active steel regions:

$$i_a = i_{oa} 10^{(E_s - E_{oa})/\beta_a} \quad (4)$$

where parameter symbols and values, also chosen for consistency with other recent plausible treatments of these systems, [Sagüés et al. 2014] are presented in Table 4.

On passive steel regions with sufficient anodic polarization, the anodic current density was made to reflect slow passive dissolution at a potential-independent value i_p :

$$i_a = i_p \quad (5)$$

The cathodic reaction was assumed for simplicity to take place at similar rates on both active and passive steel regions, given by:

$$i_c = -i_{oc} (C_{sO}/C_{eO}) \cdot 10^{(E_{oc}-E_s)/\beta_c} \quad (6)$$

The signs for anodic and cathodic current densities were chosen to follow the usual convention.

The oxygen mass flux associated with oxygen reduction at all rebar surfaces was equal to $i_c / 4F$ (mol / m²·s). The coupling between oxygen transport and the cathodic reaction at the steel surface was given by

$$i_c = -4 \cdot F \cdot D \cdot |dC_o/dn| \quad (7)$$

where D is a function of elevation per Figure 25 with values per Table 4, and n is the length along a line normal to the rebar surface. The current density distribution in the concrete domain is described by Ohm's law

$$i = -\rho^{-1} \nabla (E) \quad (8)$$

and in that domain both i and C_o are also subject to their respective continuity equations

$$\nabla (\rho^{-1} \nabla (E)) = 0 \quad (9)$$

$$\nabla (D \nabla C_o) = 0 \quad (10)$$

Equations (4) through (10) were solved simultaneously to yield the electric potential and the oxygen concentration everywhere in the concrete domain. The potential and oxygen distributions were then used in post-processing to obtain the corresponding values of the reaction current densities at the steel surface.

3.3 Scenarios Examined

The model simulations assumed that the steel above water was subject to corrosion in a splash/evaporation zone that extended vertically upward from the waterline to an elevation 2 m above it. Simulation scenario number 1 (see Table 5), which was regarded as the base case, designated as active all rebar in both the splash zone and submerged region, and as passive all rebar in the rest of the column above the waterline. Active/passive designations for the other scenarios are given in Table 5.

All scenarios except 1 and 6 represent cases that involve localized active regions of the rebar assembly (a limited number of rebar hoops) with a number of hoops vertically centered at a point halfway between the bottom of the column and the waterline. These cases idealize, as indicated earlier, possible situations of localized depassivation that established a corrosion pattern that was stable for at least part of the structure's life.

Scenarios 1-5 designated all rebar in the splash zone as active while Scenarios 6-10 designated rebar in that zone as passive to simulate cases in which the splash zone was passive. The passive splash zone scenarios represent cases wherein this region had been protected (e.g., by means of impermeable coatings) or had been rehabilitated via removal of chloride-contaminated-concrete and replacement with new concrete.

Robustness of the model output to choices of FEM mesh size, SF value, and multiple manifestations of a spatially varied chloride concentration profile on the outer concrete surface (described in detail in section 4.2) was ascertained by trial calculations, with results given in Appendix D.

3.4 Modeling Results and Discussion

Figure 26 exemplifies results for Scenario 1. Potential (E) and oxygen concentration (O_2) profiles are shown for the column cross-section. (Note that the label O_2 in the figure corresponds to C_O in Table 4.) The color-coded trends match expected results, [Kranc and Sagüés 1994] as diffusion-limited oxygen reduction below water leads to oxygen depletion inside the column (i.e., in the bulk of the concrete) in that region and potential is more negative in the submerged region than near the top.

Figure 27 shows a close-up view of a region in the submerged portion of the column where oxygen transport has reached a diffusion-limited condition. The top of the figure shows diffusional flux streamlines from the outer surface of the concrete (where $C_{eO} = 0.3 \text{ mol/m}^3$) to the region near the bars, shown in cross-section, where oxygen concentration is near zero. It should be noted that essentially all O_2 is consumed by the cathodic reaction occurring at the bars and that virtually no O_2 reaches a depth much greater than the “inner” edge of the bars; the inner core of the column throughout the submerged zone and much of the above-waterline active region is oxygen-starved.

The anodic current density was calculated for each scenario and averaged on the circumference (i.e. cross-sectional perimeter) of each individual rebar hoop in the column. The results were plotted as functions of column elevation in Figures 28 and 29. Figure 30 shows a summary of the average corrosion rate (obtained by Faradaic conversion) of steel in the submerged zone of each scenario, as a function of its associated nominal percentage of active steel surface area.

The results for Scenario 1 (steel uniformly active in the entire submerged region and splash zone) project a corrosion current density of $0.156 \mu\text{A/cm}^2$, corresponding to

a very low corrosion rate of $1.8 \mu\text{m}/\text{y}$. This result is in close agreement with the limiting cathodic current density for oxygen reduction estimated using Eq. (3), which yields $\sim 0.154 \mu\text{A}/\text{cm}^2$ when D_L and x are replaced with the values indicated in Table 4. It is also consistent with the expectations indicated in Chapter 1⁽⁴⁾ and the mechanistic interpretation made earlier. It is noted that the submerged region corrosion rate calculated for that scenario is quite uniform up to the waterline. At higher elevations the corrosion rate begins to increase as oxygen starvation and more efficient coupling with cathodic regions at greater elevations become less pronounced. For Scenario 6 (steel uniformly active in the entire submerged region but not active in splash zone), the corrosion current density for much of the submerged zone, $0.21 \mu\text{A}/\text{cm}^2$ (corresponding to a corrosion rate of $\sim 2.4 \mu\text{m}/\text{y}$), is still small but slightly larger than that of Scenario 1, showing a distinct increase when approaching the waterline. The greater corrosion below waterline and the altered pattern can be ascribed to the splash zone being a stronger net cathode than in Scenario 1, as now there is no important anodic current to support in the splash zone (i_p being very small). Macrocell cathodic coupling with the zone below water is most noticeable near the waterline where the ohmic path is shortest, hence accounting for the local corrosion current elevation there and the effects of notional immersion in saltwater as detailed below.

In contrast to the uniform corrosion scenarios, the local anodic current density/corrosion rate was much higher (by up to two orders of magnitude) in cases that

⁽⁴⁾This comparison applies for a steel placement density that was chosen to be 1:1 (i.e., $SF=1$) for these model calculations. Such a condition is not restrictive and calculations for other steel configurations are straightforward by appropriate consideration of the amount of steel surface area involved.

involved highly localized anodes (e.g. scenarios 2-5 and 7-10) even if the overall cathodic reaction rates were small. The corrosion rate enhancement was proportionally greater as the active zone involved lesser fractions of the steel surface. Clearly, while the overall amount of cathodic reaction remained nearly the same and was diffusion-limited, the concentration of the balancing anodic reaction in increasingly smaller areas led to the much higher corresponding local corrosion rates. In that context, the projected corrosion rate for a particular amount of active steel can be roughly estimated by dividing the limiting current density of the system by the fraction of active steel to total steel. This is borne out by the near-unity slope m of the log-log lines in Figure 30 ($m = -0.94$ and -0.82 for the cases without and with corrosion above the waterline respectively).

These findings are fully consistent with the mechanistic expectations noted earlier as well as with the field observations made here and documented in earlier work. [Beaton 1967] The macrocell action responsible for the concentration of corrosion is facilitated in part by the strong coupling between anodic and cathodic regions provided by the highly conductive seawater surrounding the submerged region that was represented by the equipotential treatment of the submerged surface. This issue is considered further in Chapter 4.

Of significant interest is the fact that each simulation involving passive rebar in the splash zone, while allowing for the cathodic reaction to still take place there, indicated a higher local anodic current density than that of the corresponding simulation with active rebar in the splash zone (Figure 30). Those cases effectively simulate situations where corrosion abatement was successfully implemented by means such as

rehabilitation with new concrete or the use of less permeable concrete from the start.⁽⁵⁾⁵

As noted in Chapter 1, corrosion in the splash zone would be expected to mitigate corrosion in the submerged zone due to beneficial galvanic coupling. Conversely, absence of corrosion above water while still allowing for cathodic action would be expected to have the opposite effect i.e., aggravating corrosion in the submerged zone. The model outcomes are again consistent with those expectations.

3.5 Steady-State Modeling Discussion

The most noteworthy outcomes of this investigation thus far have been the confirmation of severe localized steel corrosion in submerged bridge piles and an increased understanding of the underlying phenomena. Traditional expectations for corrosion in the submerged region rightfully indicated that in the absence of strong external cathodic regions the overall rate of corrosion would be very low, due to limited oxygen delivery to the surface of the steel. That situation however is applicable only on the average, and does not preclude the development of small regions of intense corrosion coupled to the remaining part of a generally passive steel assembly. Because of a large cathode-to-anode ratio, even a very small amount of average cathodic reaction can be enough to support a high corrosion rate on small lengths of the steel in the submerged zone.

⁽⁵⁾ Suppression of splash/evaporation zone corrosion by means of jackets with low oxygen permeability or cathodic protection/prevention could in contrast be beneficial to the submerged region, as those methods would not adversely shift the submerged steel potential upon galvanic coupling. The modeling methods used here can easily be adapted to examine those situations in follow-up investigations.

The modeling effort showed quantitatively that the observed corrosion in the piles from the field assessments is fully consistent with the postulated electrochemical setting when plausible material properties and polarization parameters are used. The modeling provided additional insight also by indicating that corrosion below water could, under certain circumstances, be aggravated if some otherwise successful corrosion control methods were effectively suppressing corrosion in the immediate tidal and low elevation atmospheric region. Those regions, where damage is conspicuous and tends to happen early, have received most of the attention in the past. It should therefore be noted that the present accepted strategy of substructure corrosion control, based on extending the length of the initiation stage through high concrete quality and thick cover, may have the unintended effect of greater vulnerability in the submerged zone. Such an effect should merit careful attention as more-ambitious durability goals e.g., design service life of 100 years or more, become commonplace.

It should be emphasized that the model used here involved a number of sweeping assumptions and simplifications, so that projections for specific cases inevitably involve uncertainty from both conservative and non-conservative treatment issues. Nevertheless the model results provided important insight with respect to the corrosion behavior of the system and provided the opportunity for more advanced realizations (e.g., a full three-dimensional treatment) to serve as tools for choosing among alternative design options.

In summary, this chapter presented a steady-state corrosion distribution model that provided a quantitative understanding of the submerged region corrosion phenomenon and its causes. The results of the steady-state modeling effort indicated

that cathodic reaction rates under oxygen diffusional limitation that are negligible in the submerged region in cases of uniform corrosion can support substantial corrosion rates when corrosion is localized. Corrosion rates projected by the model were consistent with corrosion observed and documented in the field assessments. Results also indicated that the elimination of corrosion in the splash/evaporation zone could in some cases increase corrosion vulnerability of steel in the submerged region.

The previous chapters and the advanced work described in the following chapter focus on the extent of corrosion in the submerged zone. The issues associated with structural consequences of that corrosion were beyond the scope of the work but they become an important follow-up step in the light of the expectation for possibly localized severe corrosion metal-loss documented here. In durability projection terms, that follow-up work should be the rational definition of a serviceability limit-state for the system, based on the combination of resistance and loads for which the system is designed. The dynamic corrosion progression model in Chapter 4 provides a basic foundation for this work and offers some corrosion control considerations. The dynamic modeling work also provides support for the mechanism of passivity preservation on much of the submerged region steel even in the presence of high chloride levels at the steel surface.

Table 4. Parameter and variable descriptions and values.

Parameter / Variable	Description	Value
β_a	Activation Tafel Slope for the anodic reaction	60 mV
β_c	Activation Tafel Slope for the cathodic reaction	140 mV
C_{eO}	Oxygen concentration at the external concrete surface	$3 \times 10^{-7} \text{ mol/cm}^3$
D_L	Oxygen diffusivity below the waterline, constant	$1 \times 10^{-5} \text{ cm}^2/\text{s}$
D_H	Oxygen Diffusivity above the waterline, maximum	$1 \times 10^{-3} \text{ cm}^2/\text{s}$
E_{0a}	Redox potential for the Fe/Fe ⁺⁺ + 2e system	-780 mV _{SCE}
E_{0c}	Redox potential for the OH ⁻ /O ₂ + 2H ₂ O + 4e system	160 mV _{SCE}
i_{0a}	Exchange current density for the Fe/Fe ⁺⁺ + 2e system	$3.75 \times 10^{-8} \text{ A/cm}^2$
i_{0c}	Exchange current density for the OH ⁻ /O ₂ + 2H ₂ O + 4e system	$1.4 \times 10^{-10} \text{ A/cm}^2$
i_p	Passive anodic current density	$0.01 \times 10^{-6} \text{ A/cm}^2$
ρ_L	Concrete resistivity below the waterline (constant)	3.5 kΩ-cm
ρ_H	Concrete resistivity above the waterline (maximum)	17.5 kΩ-cm
C_{sO}	Oxygen concentration at the steel surface	(calculated)
C_O	Oxygen concentration at a point in the bulk of the concrete	
E	Potential of the steel with respect to a point in the bulk of the concrete	
E_s	Potential of the steel with respect to the immediately surrounding concrete	
i	Current density	
i_a	Anodic current density	
i_c	Cathodic current density	

Table 5. Distribution of active and passive regions.

Simulation Scenario Number	Condition of Steel in Splash Zone	Nominal Percentage, Surface Area of Active Steel in Submerged Region
1	active	100
2		30
3		10
4		3
5		1
6	passive	100
7		30
8		10
9		3
10		1

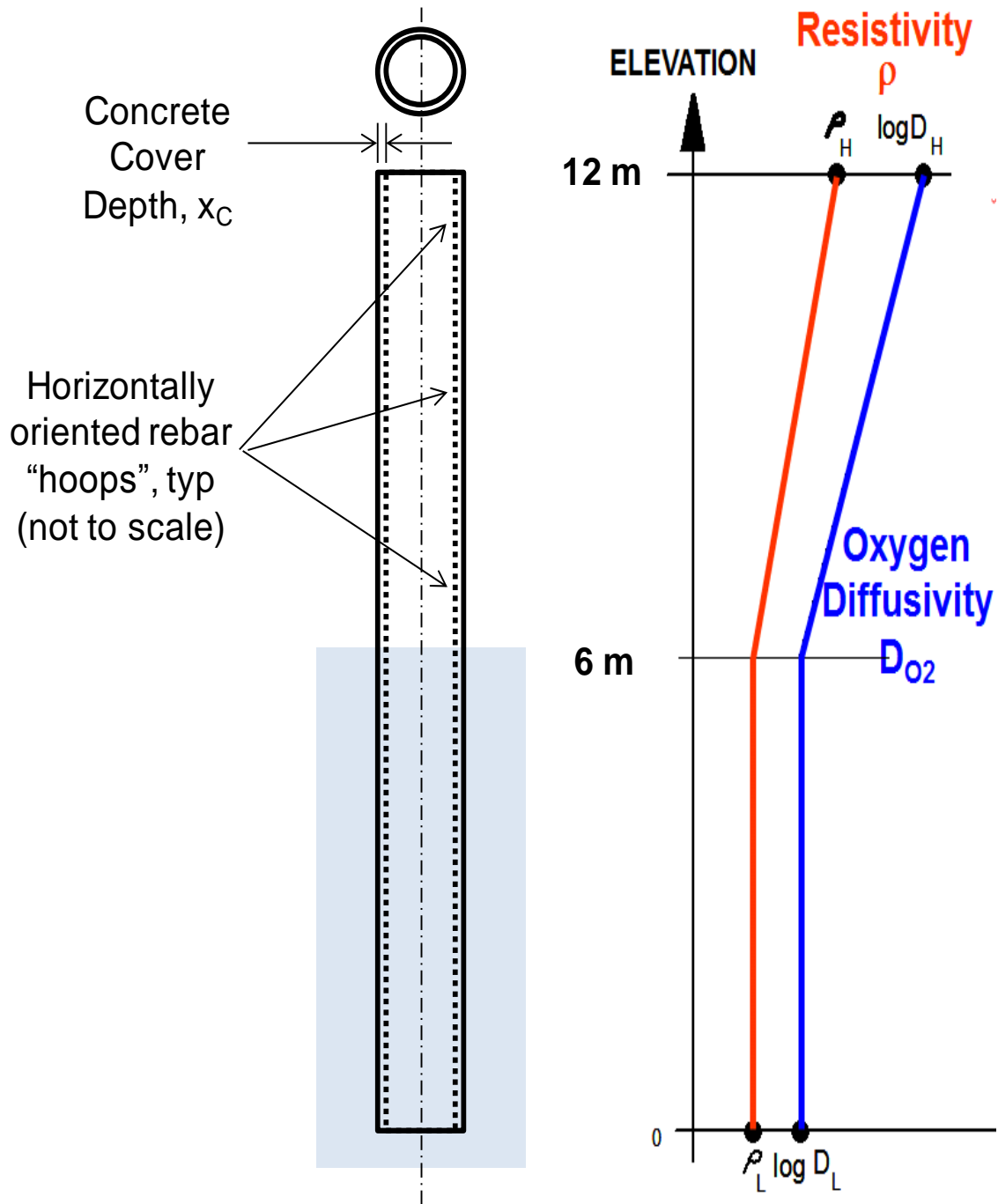


Figure 25. Concrete column model schematic diagram. Note concrete resistivity profile and oxygen diffusivity profile.

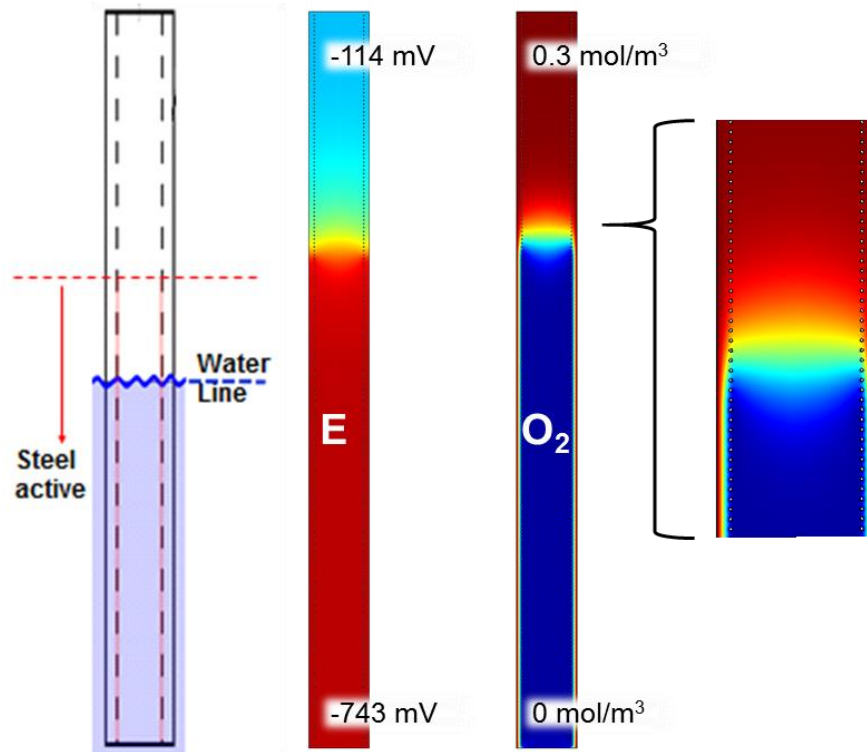


Figure 26. Potential and oxygen concentration distribution for base case. (Scenario 1) The labels indicate the values associated with the colors at the extremes of the color maps. Note that O_2 corresponds to C_o in Table 4.

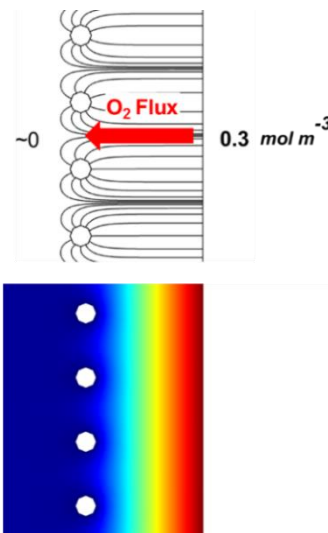


Figure 27. Oxygen content in the bulk of the concrete. Top: Streamlines that indicate the oxygen diffusion path between the outer concrete surface and the surfaces of individual rebars. Bottom: Color variation representation of the oxygen concentration between the outer concrete surface and steel bars (i.e. magnified view of the edge of the column in the submerged region depicted in Figure 26)

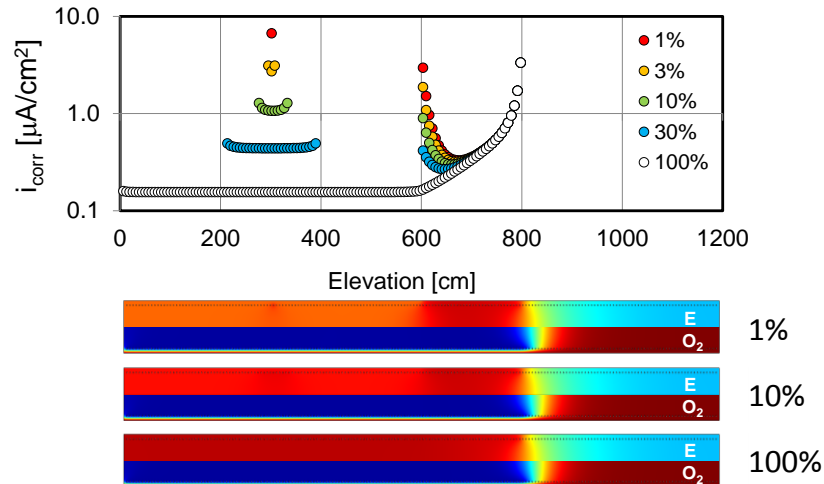


Figure 28. Projections for column with active corrosion above the waterline. Top: Corrosion current densities associated with active rebar (of indicated percentage of the submerged steel surface) centered at $z = 3$ m, and in the Splash Zone ($z = 6$ to 8 m). The rest of the steel is passive and experiencing dissolution at an extremely low rate ($0.01 \mu A/cm^2$, not plotted). Bottom: Potential and oxygen concentration profiles in selected scenarios, color-coded as in Figure 9. Note that color contrast is too subtle to reveal more-negative values in the actively corroding regions in the submerged zone. Note also that O_2 corresponds to C_o in Table 4.

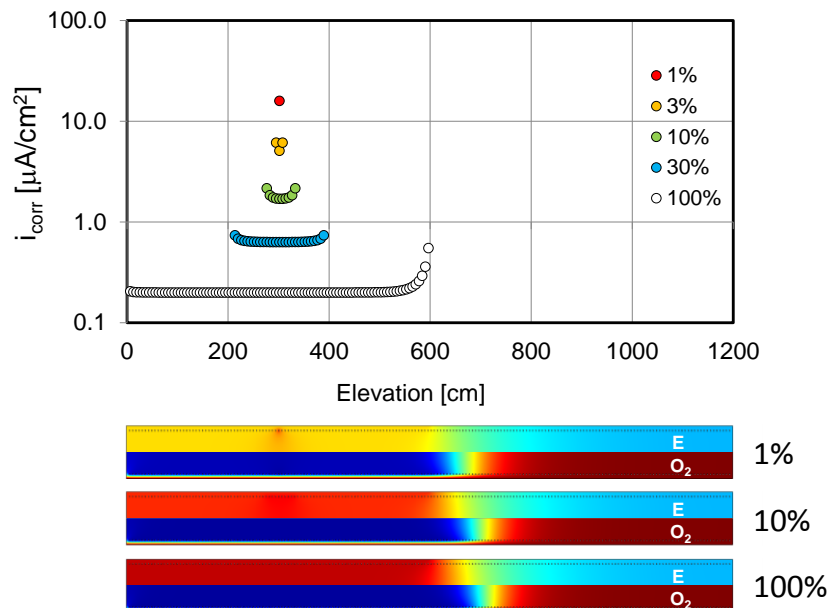


Figure 29. Projections for column with no corrosion above the waterline. Top: Projected corrosion current densities associated with active rebar (of indicated percentage) Centered at $z = 3$ m; Bottom: Potential and oxygen concentration profiles in each scenario color coded as in Figure 9. Note localized dark regions of high anodic current density in the potential profiles; O_2 corresponds to C_o in Table 4.

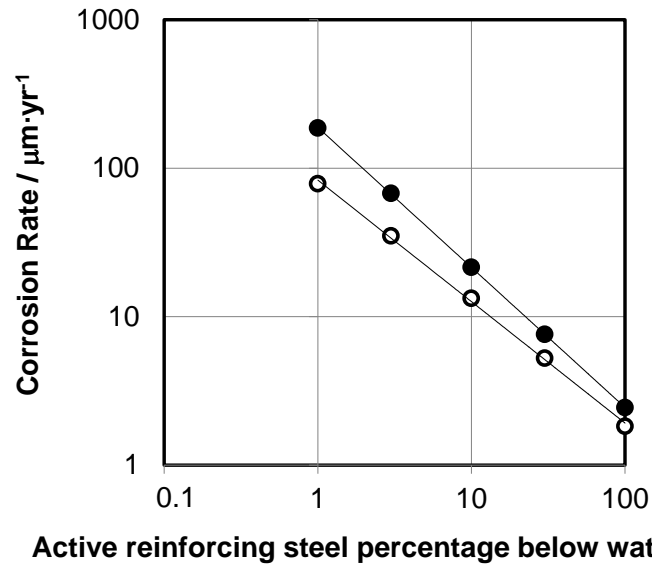


Figure 30. Corrosion rate as a function of active rebar surface area percentage. Filled circles correspond to cases with no corrosion above waterline, resulting in higher corrosion rates in submerged zone. Empty circles correspond to cases with corrosion above the waterline.

CHAPTER 4: DYNAMIC EVOLUTION MODEL

This chapter describes the development, implementation, and output of a partially submerged bridge pile model that addresses the dynamic evolution of chloride concentration at rebar depth, steel activation, corrosion current density, oxygen concentration distribution, and potential distribution. Output post-processing, damage function computation, and prognosis for a sacrificial anode cathodic protection application are also described.

4.1 Background

The results of the steady-state model presented in Chapter 3 provided support for the proposition that overall cathodic reaction rates under oxygen diffusional limitation that are negligible in cases of uniform corrosion can support substantial corrosion rates when corrosion is localized. The model results were in agreement with the field assessment, and were also consistent with the additional proposition that much of the steel in the submerged region could remain in the passive condition even in the presence of strong chloride contamination. Modeling in Chapter 3 addressed an idealized steady-state condition in a partially submerged reinforced concrete column using selected corrosion distribution patterns in the submerged and atmospheric regions. The sequence of events leading to those patterns was not however addressed beyond proposing that the stability of passive zones reflected an increase in the local chloride initiation threshold, due to cathodic polarization stemming from the anodic

reactions in nearby localized active regions. That concept is developed here in greater detail and further developed to provide an evaluation of one particular form of corrosion control.

The process presented here deals with the initiation and development of localized corrosion in both the submerged and atmospheric regions of a partially submerged column (see Figure 31). Discrete activation events are allowed to progressively modify conditions in the system, effectively accounting for interactions between the corrosion initiation and propagation stages of different parts of the system. In a successful treatment of that scenario provided recently elsewhere, [Sagüés et al. 2014] early in the life of the column the chloride presence at the steel surface is negligible and the entire reinforcing steel assembly is considered to be in the passive condition. An anodic reaction occurs everywhere on the surface of the reinforcing steel assembly at the very slow rate associated with anodic passive dissolution. In this early condition, oxygen consumption and demand are low and a relatively elevated mixed potential value prevails in both the submerged and atmospheric regions. [Sagüés et al. 2014] As time progresses, chloride from the seawater diffuses through the concrete cover and builds up near the steel-concrete interface (see Figure 32). Chloride does not accumulate uniformly at the interface due to systematic spatial variations such as higher external chloride concentration in the splash/evaporation zone [Bertolini et al. 2004] or random disparities such as local concrete deficiencies, including cracks or local variations in concrete cover thickness and surface chloride concentration. Eventually chloride concentration in one localized spot along the steel assembly exceeds the chloride threshold value and active corrosion initiates there (see Figure 33).

Continuing with this interpretation, the local corrosion rate increases dramatically over the original passive dissolution rate as a result of that initial activation. This results in a pronounced drop in local steel potential. [Bertolini et al. 2004, Sagüés et al. 2003, Broomfield 2007] The rest of the assembly remains in the passive condition but is affected by a decrease in potential to an extent that depends on the distance from the newly corroding region, the polarization characteristics of the steel, and the degree of electrolytic coupling. The most notable effect for the still-passive steel is an increase in local chloride threshold due to the potential drop, as in a classic cathodic prevention situation. [Sagüés et al. 2014, Pedeferra 1996, Sagüés et al. 2009, Lau et al. 2010 Sánchez and Sagüés 2014a] (see Figure 33) This potential dependent threshold (PDT) situation stabilizes the passive condition in nearby regions and the corrosion rate there remains low. Conversely, corrosion at spots of newly active steel is aggravated by the resulting macrocell coupling which elevates the local potential, increasing the rate of the anodic reaction. [Sagüés 2003] As time progresses, overall chloride buildup at the steel surface increases. If the chloride concentration becomes high enough, it may exceed the previously increased threshold values in other parts of the still-passive assembly and new corroding spots may appear. These new spots also tend to delay or prevent corrosion in the rest of the steel assembly, resulting in a localized corrosion pattern that tends to be sustained over a shorter or longer time-frame depending on the rate of chloride ingress and the efficiency of macrocell coupling between the various parts of the system. In the submerged region, macrocell coupling tends to be efficient due to the surrounding highly conductive seawater, thus much of the ohmic resistance between different submerged regions is presented only by the relatively short path

through the concrete cover. Consequently if corrosion at a spot in the submerged region started relatively early in the life of the structure e.g., due to a local concrete deficiency, that spot may tend to remain relatively stable feature over a long period of time. Such a situation would be consistent with the field observations presented in Chapter 2 where relatively small localized corrosion regions were found to be surrounded by large amounts of non-corroding steel, much of which exhibited an undisturbed surface appearance.

To examine the plausibility and implications of the above interpretation, an enhanced corrosion progression model incorporating the effects of macrocell coupling, PDT, and integrated initiation-propagation corrosion behavior was created to simulate the sequence of events leading to the development of a nearly stable corrosion distribution pattern in the submerged region. The model also improves over the earlier PDT treatment [Sagüés et al. 2014] by representing detailed spatial resolution at the rebar level. As mentioned previously, the enhanced model also provided the capability to evaluate the possible application of cathodic protection (CP) of the submerged region by sacrificial anodes.

4.2 Model Formulation

A notional partially submerged cylindrical steel-reinforced concrete column (Figure 31) was modeled using a Finite Element Modeling (FEM) two-dimensional axisymmetric geometry in COMSOL Multiphysics. The selected dimensions, values, and some variation schemes largely approached those of the steady-state model presented in Chapter 3 but are restated here in part, for completeness. This arrangement, while idealized, effectively captures the essential representative

conditions of piling in a marine environment and the insights derived are applicable to the issues of interest. The column had a 0.525 m radius and 12 m height. The rebar cage was simulated by an arrangement of horizontally-oriented interconnected hoop elements made of 0.02 m diameter bars vertically separated by 0.063 m on center (see Figure 31). As in Chapter 3, a steel placement density factor (SF) =1 (i.e., 1 m² of steel surface area for every 1 m² of column exterior concrete surface area), was used. Clear cover depth was 0.075 m. The waterline was placed at the midpoint of the total height, elevation $z = 6$ m. For simplicity and because of practical computational limitations, vertical bars or similar features not suitable for representation in full-rotational symmetry were not included. Events such as activation of the steel surface or subsequent surface damage due to corrosion-product-induced cracking are thus somewhat coarsely ascribed to one entire rebar hoop at a time. However, while simulation of corrosion localization to extremely small portions of the steel is thus precluded, examination of the effects of small percentages of active surface such as those encountered in the field can nonetheless be reasonably conducted given the large number of hoop elements in the system.

The half of the column above the waterline, including the top end, was regarded as having an electrically-insulated surface; the lower submerged half was regarded as having a surface with a single floating potential, given its direct contact with relatively high conductivity seawater. For simplicity, the bottom end of the column was regarded as an electrically insulated surface. For conservation of charge, the net electrolytic current integrated on the rest of the submerged surface was set to zero.

The resistivity of the concrete and the oxygen diffusion coefficient of the modeled concrete were set at values below the waterline that were not elevation-dependent, reflecting the assumption that the concrete in this region was uniformly wetted. For the region above the waterline it was assumed that increasingly drier conditions with elevation led to both higher resistivity and oxygen diffusivity. Consequently and following previous work [Kranc and Sagüés 1994] both the concrete resistivity and the logarithm of the oxygen diffusivity were made to vary linearly with height above the waterline as in the steady-state model and as shown in Figure 31. Oxygen concentration at all points on the column's exterior surface was assigned a constant value (see Table 6) and oxygen flow through the top and bottom surfaces of the column was not allowed.

The chloride concentration profile on the exterior surface of the column, implemented for all of the dynamic evolution simulations, was built by adding statistical spatial variability, as described later, to a simple time-invariant baseline function of elevation. The baseline chloride concentration was uniform below the waterline but rose sharply to a peak at the waterline (see Figure 34, top), representing evaporative salt accumulation as discussed in detail in Chapter 2 and elsewhere. [Kranc and Sagüés 1994, Sagüés et al. 2001, Sagüés et al. 2010] Baseline concentration then decreased linearly to zero at the top of the column. Table 6 lists model parameters and their respective values plus additional parameter variation values used in the cases examined. The steel polarization and cathodic prevention parameter values are based on those used in the steady-state model and previous investigations. [Sagüés et al. 2014] The key concrete properties of resistivity and chloride diffusivity were assigned

various alternative values representing a broad range of conditions. Those values included combinations typical of less-protective, highly-permeable, and highly-conductive concrete (i.e., high chloride diffusivity, low resistivity cases) such as that encountered in some of the Florida Keys bridges that experienced early corrosion in the 1980s [Sagüés et al. 2010] and in the older bridges whose piles were described in Chapter 2. The cases examined also included values characteristic of highly protective concrete (i.e., low chloride diffusivity, high resistivity cases) approaching conditions encountered with the use of modern concrete with low water-to-cement ratio, high cement content, and pozzolanic admixtures. [Sagüés et al. 2001] For completeness, cases with medium (“Med” in the table and figures) parameter values and combinations of contrasting resistivity and chloride diffusivity properties were also included. The matrix of cases explored is presented in Table 7.

For the PDT treatment, the chloride threshold C_T was assumed to increase as the result of cathodic polarization according to

$$\log\left(\frac{C_T}{C_{T_0}}\right) \sim \frac{E_{T_0} - E}{|\beta_{C_T}|} \quad (11)$$

[Alonso et al. 2000, Presuel-Moreno et al. 2005, Lau et al. 2010] where C_{T_0} is the chloride threshold at the baseline potential E_{T_0} , E is the potential of the steel (while still in the passive condition), and β_{C_T} is the so-called cathodic prevention slope.

The implementation of PDT features for developing a dynamic corrosion evolution projection involved: 1. Simulating the ingress of chloride ions via diffusion into the bulk of the notional concrete column, 2. Monitoring chloride concentration near each discrete segment of the rebar cage, 3. Recognizing points in time when the chloride

concentration in the discrete region of the rebar closest to the external surface exceeded the chloride threshold in that region, 4. Modifying the electrochemical condition of the steel surface (i.e., changing its designation from “passive” to “active”) in that region where the threshold was exceeded, and then recalculating the resulting new potential profile with associated new chloride threshold profile, and 5. Allowing the chloride diffusion penetration in the system to further evolve until the new local threshold is exceeded in another region, changing steel character there to “active”, and repeating the process for the next steps. [Sagüés et al. 2014]

Each simulation covered a 100-year service period. Prior to initiating each simulation (i.e., commencement of service life), the chloride concentration in the bulk of the concrete column was set to zero, approximating the typically very low native chloride content present in field applications. [Sagüés et al. 2001]

For proper incorporation of corrosion propagation stage features, the model keeps track of both the resulting corrosion rate at each elevation and the accumulated corrosion penetration P at the rebar surface. For elevations above water, it is assumed that when P reaches a critical value P_{Crit} , the accumulation of corrosion products at the rebar-concrete interface will cause cracking of the concrete cover. This criterion has been used successfully in prior modeling efforts [Sagüés et al. 2014] where a nominally representative value $P_{\text{Crit}} = 100 \mu\text{m}$ was adopted based on observations from the literature [Torres-Acosta and Sagüés 2004, Broomfield 2007]. Note that an alternative P_{Crit} value of $250 \mu\text{m}$ for steel in the submerged zone was also implemented for comparison as described below. Given the rebar size and center-to-center distance used in the simulations, damage in the form of cracking and related delamination/spall

associated with one rebar reaching the cracking criterion was regarded as affecting a region of elevation with height h around the entire circumference of the column. The parameter h was assigned a value equal to the center-to-center rebar distance, approximately 6.3 cm. Accordingly, the fraction of the external concrete surface having reached the declared damage condition at a given time was simply equal to the number of rebar hoops for which the condition was reached, divided by the total number of rebar hoops. The resulting value as time evolves, expressed as a percentage, was defined as the Damage Function (DF) of the column.

Preliminary calculations were performed with the present model using column dimensions and parameters, as well as a baseline chloride surface concentration without statistical variability, matching those used in a previous investigation of the PDT concept that used a simplified *finite-difference* corrosion computation method. [Sagüés et al. 2014] The DF results obtained with the present more-sophisticated model were found to closely approach those in the earlier work, thus providing a positive check of the functionality of the present implementation.

In the present model some degree of parameter spatial variability was introduced to simulate random early corrosion initiation at some locations on the steel assembly, including some in the submerged zone. That variability can possibly reflect, as indicated above, issues that may include but not be limited to local concrete deficiencies, local lower rebar cover, or fluctuations in steel-concrete interfacial condition and surface chloride content. For modeling convenience and simplicity, random spatial variability was chosen to be limited to the single parameter, chloride content C_s on the exterior concrete surface. For the purposes of the present

examination this approach captures the essential features necessary for a degree of randomness in corrosion initiation. This choice is not limiting and future implementation of combined variability of multiple parameters such as rebar cover and chloride diffusivity, while possibly laborious, would be conceptually straightforward. Advances of this type have been successfully implemented in a previous finite-difference PDT model implementation by Sánchez. [2014, Sánchez and Sagüés 2014c]

The C_s variations were assumed to involve a coefficient of variation (standard deviation divided by average) of 0.25 (25%) around the baseline elevation trend shown in Figure 34 (top). The 25% value was on the order of the variability encountered in C_s values in representative marine substructures. [Sagüés et al. 2001] The profile with surface concentration variability was constructed by selecting elevations evenly separated by 0.5 m, starting from the bottom of the column (a total of 25 values) and multiplying the initial C_s value at each point by the sum $(1 + \text{random adj})$ where “*random adj*” is a number generated by a one-time application of the Microsoft Excel function $\text{NORMINV}(\text{RAND}()) \times 0.25$. As chloride concentration was assumed to vary linearly between local minima and maxima, the value of C_s at any point on the exterior surface of the column elevation was obtained by interpolation of the values declared at the selected points used in the above procedure.

Figure 34 (bottom) illustrates the resulting pattern of chloride concentration at the rebar depth as function of time. The altered C_s pattern, which was used for all simulations presented here, yielded situations in the submerged portion where corrosion initiation occurred slightly earlier than in the rest of that portion, thus generating local anodes and enabling exploration of the implications of PDT behavior. An evaluation of

system response to the use of alternative C_s profile realizations with the same variation parameters but different random assignments is presented in Appendix D which shows that the resulting DF projections are largely unaffected by the specific selection of a given statistical assignment.

In addition to simulating the evolution of corrosion without intervention, the model was used to examine the effectiveness of corrosion control measures in the submerged zone and low-elevation regions above the waterline by means of a notional sacrificial anode cathodic protection (SACP) approach. Implementation of this feature represented what would have been accomplished, in practical terms, by pre-fitting the rebar assembly with a contact for an external sacrificial anode to be installed at the commencement of a structural element's time-in-service. Given the low resistivity of seawater and the relatively low current densities present in these systems, it was assumed that the connection of the anode resulted in a shift of the assumed single floating-potential condition at the submerged surface of the column, to an operating potential value E_{Prot} characteristic of the anode used. For these realizations the anode was assumed to be a commercial zinc anode with $E_{Prot} = -1,050$ mV (vs SCE). The DF for the SACP cases was calculated using the same approach as used for the freely corroding system. Table 7 identifies the cases in which SACP was implemented.

In addition to the sensitivity of computation results to the choice of randomization of C_s , test trials were made to ascertain robustness of outcome to the choice of both FEM mesh size and SF. The results of those evaluations are presented in Appendix D. Note that the calculations and their results can be applied to both the steady-state and dynamic models as the models share current distribution calculations.

4.3 Results and Discussion

4.3.1 Projections for Unprotected Systems

As mentioned previously it should be emphasized that the model involved a number of sweeping assumptions and simplifications. Consequently, projections for specific cases inevitably involve uncertainty from both conservative and non-conservative treatment issues. Nevertheless the model results provided important insight on the corrosion behavior of the system and on the feasibility of corrosion control. A detailed discussion of the sequence of events taking place in a PDT simulation has been presented elsewhere, [Sagüés et al. 2014] so only the salient points for the present system are discussed in the following.

As the simulation is initiated, chloride starts to diffuse inward from the concrete's exterior surface to the surface of the embedded reinforcing steel. As shown in Figure 34, the highest chloride concentration values in the randomly altered C_s pattern on the concrete exterior surface are found near the waterline, where evaporative concentration is greatest, so the first projected corrosion activation events occur in that region as expected. The projected time-evolved corrosion distribution is shown in Figure 35 for Case 1 (Table 7) via potential maps of the concrete cross section. For the particular parameter values in that case the potential over much of the concrete domain is a sensitive indicator of corrosion condition of the nearby steel. More negative potential (color shifting in the red direction) is for the present example indicative of nearby anodic activity, to some extent analogous to the indications obtained by potential surveys

performed according to ASTM C-876. [ASTM 2009]⁽⁶⁾ While the calculation time step was 30 days, the maps are shown at uneven intervals in multiples of nine years for brevity, illustrating the majority of a 100-year simulated service timespan. The detailed order of activation events in the first nine-year period is not apparent given the selected timescale but relative color intensities provide some indication of the activation history. Each of the first five steel elements to activate was either in or very near the splash/evaporation zone, separated vertically by a number of other steel elements that remained in the passive condition, in keeping with the behavior expected under a PDT scheme. [Sagüés et al. 2014] The projected activations started at $t = 3.4$ years and occurred at uneven intervals over the ensuing two years. As Case 1 is a high-resistivity concrete scenario, preventive polarization from early corrosion onset near the waterline did not extend strongly to the submerged region. Consequently, and as that region had some of the largest C_s values (per the profile in Figure 34) the next projected activation events took place near the center of the submerged region (at 5.9 years) and later near the bottom of the column. As time progressed and chloride content at the steel depth increased, other activation events took place both above and below the waterline. Potentials throughout the submerged zone and at parts of the splash zone reflected that situation by becoming increasingly negative. The corrosion in parts of the submerged region distant from the waterline remained limited to only a few locations through the entire simulated period. Such outcome is consistent with and in support of the expectations noted in Chapter 1. As will be shown below, projected development of

⁽⁶⁾ It is recognized that as oxygen starvation becomes more marked, the relationship between potential and corrosion condition becomes less significant. [Elsener et al. 2003]

corrosion in the much of the submerged region became even more restricted in cases where concrete resistivity was low and preventive coupling with corroding regions in the atmospheric zone was more effective. It is important to note that, as indicated in Chapter 1, the localized corrosion rates in the submerged region can be very high even though the supply of oxygen to the rebar surface is very limited. The local corrosion rates in the submerged zone projected by the model were high enough to result in multiple damage declarations during the service span considered.

The resulting DF for each case presented in Table 7 is shown in Figure 36. The DFs show the typical time trends expected for this kind of system when chloride diffusivity has been assumed, for simplicity, to be the same at all elevations. [Sagüés et al. 2014] No significant damage was projected during an initial period corresponding to the chloride ion buildup time at the rebar depth before the first event where a local corrosion threshold is reached. Corrosion, once it initiates near the waterline, is localized and its rate is high since no active steel exists elsewhere and the rest of the system is cathodic. Accordingly, the first manifestation of damage occurs in that region quite early, at a time equal to the sum of the time-to-activation and the time necessary for local metal wastage to reach P_{crit} . That total duration is shortest for the cases of lowest resistivity, where the sacrificial macrocell coupling of that first corroding steel to the rest of the rebar assembly is strongest.

As time progresses, the initial pattern of dependence of damage on resistivity tends to be reversed. The corrosion-preventive effect of the first corroding zone on the rest of the assembly, which results in a delay of the second activation event, is stronger when low resistivity concrete permits more efficient macrocell coupling between

corroding and non-corroding regions and this effect continues in the chain of subsequent events. As evidenced by comparing the DF plots for a given chloride diffusivity, the projected long-term damage progression becomes (paradoxically) less-pronounced with decreasing concrete resistivity, as is discussed in greater detail elsewhere. [Sagüés et al. 2014, Sánchez 2014, Sánchez and Sagüés 2014b]

The projected dependence of the damage progression on chloride diffusivity is straightforward; as the chloride diffusivity decreases, the time-scale of initial and subsequent activation events increases. Accordingly the DF plots are displaced to greater time values as the implemented chloride diffusivity value decreases. The timescale of the simulations captures DF projections that agree with typical observations in bridges in aggressive marine environments such as those in Florida. [Sagüés et al. 2001, Sagüés et al. 2010, Sagüés et al. 2014] As is well-documented in the literature, structures with chloride diffusivity on the order of 10^{-7} , 10^{-8} , and 10^{-9} cm²/s are expected (for the rebar cover value assumed, 7.5 cm), to begin showing some signs of deterioration at times on the order of one decade, a few decades, and from several decades to over 100 years respectively. [Sagüés et al. 2001, Sagüés et al. 2010, Lau et al. 2010] The DF projections indicate that very conspicuous damage (several % of the column surface exhibiting delamination or spall symptoms) can be expected at structure ages on the order of two times greater than ages at which the first signs of damage appear.

The results discussed above addressed the combined damage of both the atmospheric and the submerged regions. Regarding the main issue in this investigation, it is noted that in those realizations the part of the DF specific to the

submerged region was found to be consistently smaller than that for the atmospheric region. That difference is to be expected from the above discussion, as exemplified by the Case 1 analysis. For those calculations no distinction on the limit damage criterion was made between the submerged and atmospheric zones, using the same value $P_{CRIT}=100 \mu\text{m}$ value for both regions. While this value represents a reasonable assumption for typical atmospherically exposed concrete situations, [Torres-Acosta and Sagüés 2004] it may not be the most appropriate for the submerged zone, for the reasons discussed in Chapter 1. As discussed in Chapter 3 and suggested by the field examination results in Chapter 2, it is likely that damage in the submerged zone may not be manifested by significant concrete cracking since (given the saturated pore network) corrosion products may be more easily transported via the saturated pore network, to locations further away from the corroding interface than would be observed in atmospheric regimes. It should also be noted that in cases that involve limited oxygen availability, iron ions could stay in solution locally [Broomfield 2007] and, unlike the expansive corrosion products more often encountered, be less likely to exert tensile stresses in the concrete that could lead to cracking. Thus, a more relevant local limit-state using a greater P_{crit} value in the submerged zone may be selected to account for issues such as loss of bond between rebar and concrete, simple rebar mechanical failure under acting stresses, or loss of bending moment as described by Andrade et al. [1990] In the absence of reliable data, a conservative tentative limit condition is proposed whereby bond loss or other adverse mechanical deterioration would take place when rebar cross-section is reduced by corrosion to a level comparable with the low-end of rebar production dimensional tolerance, i.e., about 5% less than the initial

cross-section. For the 2 cm bar diameter in the simulations, this would correspond to a P_{Crit} value of approximately 250 μm , or 2 ½ times greater than the one used for the atmospheric condition. In the case of the alternative interpretation by Andrade et al. [1990] described above, this P_{Crit} value would correspond to a loss in bending moment for an affected structural element of an amount on the order of 6%. While recognizing its tentative character, that value was adopted to recalculate damage progression projections specific to the submerged region. Results are shown in Figure 37 for steel in locations below an elevation corresponding to a distance approximately 1/3 of a column radius below the waterline in order to avoid conditions not fully representative of the submerged condition.

Figure 37 shows that the projected damage for the submerged zone by itself is generally only a small fraction of the total damage and that it affects only a few percent of the steel elements below water after several decades of service, a result consistent with the field observations noted in Chapter 2. Moreover, for any given chloride ion diffusivity, the projected submerged region damage was distinctly greater in cases of high concrete resistivity, consistent with the interpretation discussed above whereby preventive and protective cathodic polarization from the rest of the system is expected to be less efficient in lowering the incidence of activation events. The projected dependence on chloride diffusivity is also consistent with assumptions discussed earlier. It is noted that, as shown by the added example included in Figure 31 for Case 1, the above observations are not likely to be highly sensitive to the choice of P_{Crit} . Using the lower P_{Crit} value (100 μm) yielded earlier damage projections but did not otherwise significantly affect the overall DF development. In conjunction with the previous

discussion, these observations provide further support for both the conceptual validity of the modeling approach used and the interpretation of the sequence of events leading to the observed corrosion modality in the submerged region described in Chapter 1. Such consistency encouraged the further use of the model to examine the prospect of success for a possible corrosion control method.

4.3.2 Projections for Cathodically Protected Systems

Figure 36 shows the projected DF for the SACP cases in dotted lines with the same line color as the corresponding cases without SACP. Application of the anode from the start significantly delays the projected appearance of first damage in most cases, and also reduces the total amount of projected damage over the long term. Even though the anode is placed in contact with the seawater only, appreciable beneficial effect was projected to extend to steel above water, (consistent with the findings of other authors [Sagüés et al. 1998, Presuel-Moreno et al. 2005, Pergola 2013]) especially in the low-elevation regions where the electrolytic conductive path via the column concrete is shortest and the resistivity of the concrete is lowest. Of great significance is the result that application of the anode completely prevented the onset of projected corrosion below water for the entire 100-year simulation period for the entire set of scenarios investigated, regardless of the local limit-state declaration used. Consequently, no DF projection curves for the SACP cases appear in the submerged region projections in Figure 37.

The projected electrical current demand on the anode by the column modeled here (having about 20 m² of surface below water, a size comparable to that encountered in typical service applications) was found to be only on the order of 40 mA.

That value changed little with projected age as new regions on the column surface (all above water) became active. The relatively small current value is consistent with the amount expected to be sufficient to sustain the cathodic reaction at the small limiting current density prevalent in these systems as noted earlier. For a zinc marine anode with a typical consumption rate of 11.2 kg / year, [Roberge 2008] the wastage would be on the order of 0.5 kg / year, so modest-sized commercially available anodes such as those used for marine substructure jacket rehabilitation systems [FDOT 2010] could conceivably last for long time periods (e.g., decades) in regular piles before needing replacement. It is noted that a potentially adverse effect could be an increased susceptibility to hydrogen embrittlement (HE) of the high-strength strand in pre-stressed concrete piles. This issue is addressed in greater detail below.

The assumed operating potential for the zinc anode i.e., -1,050 mV SCE, is more negative than the potential values beneath which the likelihood of hydrogen evolution and associated HE is deemed to be of concern, approximately -950 mV SCE. [Hartt et al. 1993, Hartt et al. 1998] However, the model calculations indicated that potential of the steel in the submerged region (at least in the high resistivity cases) was about 35 mV less negative than the assumed anode potential, accordingly reducing the excursion into adverse polarization regimes. Also, typical instant-off steel potential values observed in a recent survey of marine substructure field installations with zinc galvanic anodes were seldom more negative than -900 mV SCE, [Hartt and Presuel-Moreno 2009], likely due to anode polarization and electrolyte plus metallic circuit resistances, factors for which the model only partially accounted. Hence the risk from excessive

cathodic polarization, while meriting some consideration in future work, does not appear to be a high-priority concern.

To further explore the HE susceptibility issue, sensitivity to anode potential was evaluated with special model subcases for three cases of particular interest: (1) low concrete resistivity, high chloride diffusivity (Case 16), typical of concrete used in the mid-20th century; (2) high concrete resistivity, low chloride diffusivity (Case 12) , typical of modern-specification concrete; and (3) high concrete resistivity, high chloride diffusivity (Case 10), typical of modern-specification concrete with deficiency(ies).

Damage functions for various anode potentials (-600 mV, -750 mV, -900 mV, and -1,050 mV SCE) are shown in Figure 38. As indicated, projected corrosion suppression below water and in the region near the waterline was still very effective even if the operating anode potential is much less negative than the -1,050 mV value used e.g., -600 mV SCE. Furthermore, damage function sensitivity to anode potential within the range explored was shown to be small indicating consistency with the provisions of model uncertainty noted earlier. Given the effectiveness of projected protection of the submerged zone for representative Cases (1, 12 and 16 in Table 7) under anode operating potentials as modest as -600 mV, alternative anode operating modes (e.g., using limiting resistors) could be implemented if HE was a concern.

4.4 Significance of Modeling Findings

The modeling effort showed quantitatively that the corrosion observed in the field is fully-consistent with the electrochemical mechanism described in the introduction when plausible material properties and polarization parameters are used. The insight provided by the steady-state model presented in Chapter 3 indicated that the corrosion

of steel below the waterline could be aggravated if some kind of otherwise successful corrosion control methods (e.g., conventional jackets) effectively suppresses corrosion in the immediate tidal and low elevation atmospheric region while still allowing for cathodic reactions. Those regions, where damage is conspicuous and tends to happen early, have received most of the attention in the past. In the absence of corrosion there, those regions could support significant external cathodic action (not countered by the suppressed anodic reactions) and be available to enhance corrosion below water. Hence, it is possible that the present accepted strategy of marine substructure corrosion control, based on extending the length of the initiation stage through high concrete quality and thick cover, may have the unintended effect of greater vulnerability in the submerged zone. This type of effect would become increasingly important as durability goals become more ambitious and design lifetimes are extended to 100 years or more. Accordingly, a broader-scope approach to marine substructure corrosion control including both atmospheric and submerged regions merits renewed consideration.

The dynamic modeling effort presented here examined the evolution of corrosion in a generic column/pile for scenarios generally representative of the range of conditions encountered in marine bridges. Results of the calculations indicated that the vulnerability to submerged zone corrosion, for a given rate of chloride penetration in the concrete, tended to be more manifested if the concrete resistivity was high. This behavior is somewhat counterintuitive, as corrosion is usually expected to be more severe in cases where low concrete resistivity permits more efficient macrocell coupling between anode and cathodes. However, in the context of the phenomena noted earlier, higher resistivity also tends to electrolytically isolate the new candidate anodic sites

(while they are still in the passive condition) from previous, already active anodic regions. The poorer electrolytic contact diminishes macrocell coupling that would have been beneficial by making the potential of the candidate sites more negative, thus preventing or delaying new corrosion initiation events (and also providing some degree of cathodic protection after new activations). For the submerged region, those preventive/protective previously corroding regions are most likely corroding spots in the region immediately above water. As the best-performing concrete formulations used by transportation agencies for marine service also have high resistivity, [FDOT 2015] the possibility of corrosion in the submerged region could be compounded accordingly.

From the standpoint of damage development with time and with consideration of the fact that the concrete cover chosen for the simulations is representative of common pile design, the model projections suggest that substantial incidence of submerged-region corrosion could take place during the first few decades of service for more permeable concretes. For medium quality concrete the damage is projected to develop after several decades of service. For modern, high-quality concretes in sound condition the damage prognosis indicates some concern only for ages on the order of the present commonly adopted service life of 75+ years. It is noted however that these projections have not explicitly addressed the case of cracked concrete. If cracks were to occur during pile-driving for example, chloride penetration and hence corrosion initiation at the crack-steel intersection could happen very fast. [Lau et al. 2010] Thus, the damage development at cracks below water in otherwise high-quality concrete may resemble that of the high-resistivity, but medium- or even high-chloride-diffusivity concrete. Consequently, the possibility of topical severe corrosion at the spots affected by

cracking could not be ignored under those circumstances. As noted in Chapter 3, a thorough analysis of structural implications of the corrosion damage addressed here is in order as an important follow-up step for establishing a serviceability limit condition more suitable for more useful life forecasts.

The model also permitted evaluation of the effectiveness and feasibility of controlling submerged zone corrosion by means of a sacrificial cathodic protection anode. The results were favorable, projecting virtual suppression of submerged zone corrosion and some additional benefit in reducing corrosion in the immediate tidal zone above water. The projected rate of anode consumption was low enough to indicate that application of a regular modestly-sized and priced commercial anode could offer effective corrosion control over a period of decades before need for replacement. Accordingly, the possible incorporation of anodes as a regular feature for submerged piling in new construction is deemed as meriting further examination.

In summary, the results of dynamic modeling supported the proposition that the passive state of a large portion of the steel can be preserved in the presence of high chloride concentration at rebar depth, even if typically assumed chloride threshold values have been exceeded. This can be attributed to the threshold dependence on local steel potential. The model projections of corrosion extent and localization were also consistent with the findings of field assessments. Results also indicated that high concrete resistivity, which is typical in low permeability concrete chosen for achieving long service-life in the above water region, may under certain conditions promote unintended corrosion vulnerability of the submerged region by lowering the extent of beneficial macrocell coupling there.

In addition, the model projected that *sacrificial anode cathodic protection* for partially submerged marine reinforced concrete structural elements could effectively eliminate corrosion in the submerged zone and simultaneously provide some measure of protection for steel in the splash/evaporation zone.

Table 6. Parameter values used in the dynamic evolution model simulations.

Parameter	Description	Value	
β_a	Activation Tafel Slope for the anodic reaction	60 mV	
β_c	Activation Tafel Slope for the cathodic reaction	140 mV	
β_{CT}	Cathodic prevention Slope	0.55 V	
C_{eO}	Oxygen concentration at the external concrete surface	3×10^{-7} mol/cm ³	
C_{sO}	Oxygen concentration at the steel surface	(calculated)	
C_{sB}	Chloride concentration at the concrete surface, bottom	9 kg/m ³	
C_{sP}	Chloride concentration at the waterline	20 kg/m ³	
C_{sT}	Chloride concentration at the concrete surface, top	0 kg/m ³	
C_{T0}	Baseline chloride threshold value at E_{T0}	1.78 kg/m ³	
D_L	Oxygen diffusivity below the waterline	1×10^{-5} cm ² /s	
D_H	Highest value of oxygen Diffusivity above the waterline	1×10^{-3} cm ² /s	
D_{Cl}	Chloride diffusivity	Low	8.3×10^{-9} cm ² /s
		Med	2.5×10^{-8} cm ² /s
		High	7.5×10^{-8} cm ² /s
E_{0a}	Redox potential for the Fe/Fe ⁺⁺ +2e system	-780 mV _{SCE}	
E_{0c}	Redox potential for the OH ⁻ /O ₂ + 2H ₂ O +4e system	160 mV _{SCE}	
E_s	Potential of the steel with respect to the immediately surrounding concrete	(calculated)	
E_{T0}	Baseline steel potential value at C_{T0}	-0.100 V	
i_{0a}	Exchange current density for the Fe/Fe ⁺⁺ +2e system	3.75×10^{-8} A/cm ²	
i_{0c}	Exchange current density for the OH ⁻ /O ₂ + 2H ₂ O +4e system	1.4×10^{-10} A/cm ²	
i_p	Passive anodic current density	0.01×10^{-6} A/cm ²	
x_c	Concrete cover	7.5 cm	
ρ_L	Concrete Resistivity below the waterline (three cases)*	Low	3.5 kΩ-cm
		Med	10.5 kΩ-cm
		High	31.5 kΩ-cm
ρ_H	Concrete Resistivity above the waterline (three cases)*	Low	17.5 kΩ-cm
		Med	52.5 kΩ-cm
		High	157.5 kΩ-cm

* Note that each case modeled used both a ρ_L and a ρ_H value linked according to the description "High", "Med", or "Low". Example: "High" resistivity cases used $\rho_L = 31.5$ kΩ-cm and $\rho_H = 157.5$ kΩ-cm. The "High", "Med", or "Low" designation for D_{Cl} was independent of that used for resistivity.

Table 7. Cases evaluated.

Case Number		1	2	3	4	5	6	7	8	9	10	11	12	13	14	15	16	17	18
Concrete Resistivity *	High	•	•	•							•	•	•						
	Med				•	•	•						•	•	•				
	Low							•	•	•							•	•	•
Chloride Ion Diffusivity *	High	•			•			•			•			•			•		
	Med		•			•			•			•			•			•	
	Low			•			•			•			•			•			•
Submerged Sacrificial Anode Cathodic Protection (SACP)	N	•	•	•	•	•	•	•	•	•									
	Y										•	•	•	•	•	•	•	•	•

* The descriptions "High", "Med", and "Low" correspond to parameter values indicated in Table 6. All cases were examined for the randomly altered surface chloride pattern (see text).

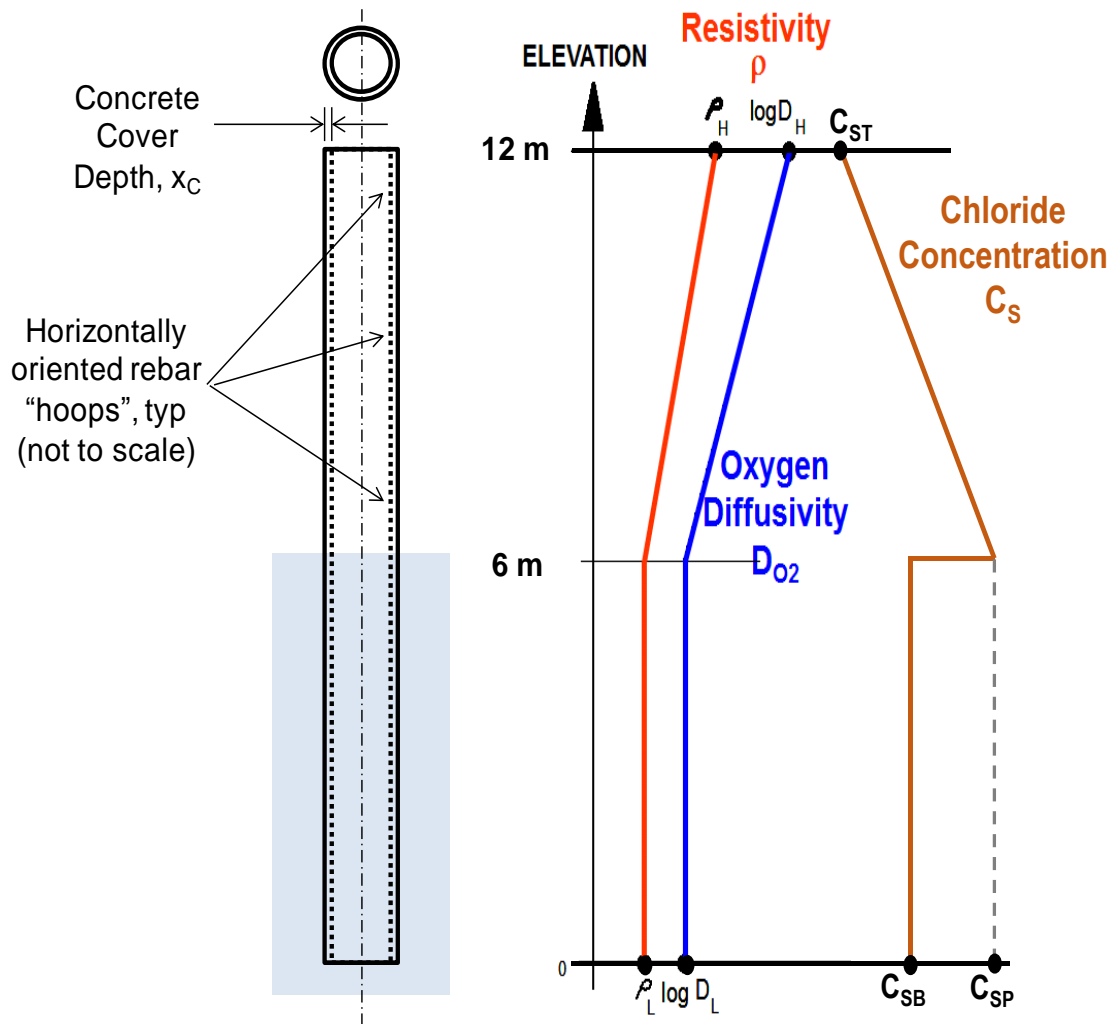


Figure 31. Dynamic evolution model schematic diagram. Chloride concentration profile is a baseline trend on which statistical variability is superimposed. Other parameter distribution patterns match those of the steady-state model in Chapter 3.

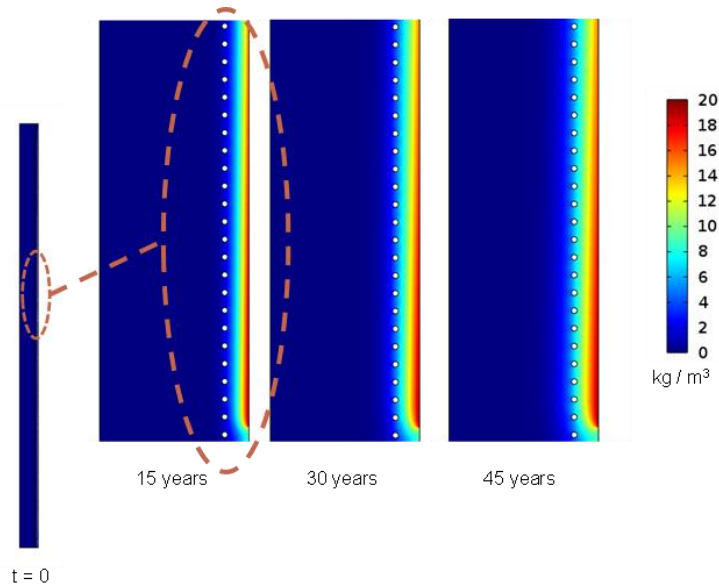


Figure 32. Chloride concentration penetration as function of column age. Time-evolved chloride concentration in the region just above the waterline with a simple surface chloride profile is shown. Concrete property parameters correspond to the medium chloride ion diffusivity cases in Table 7 simulating a moderately permeable concrete.

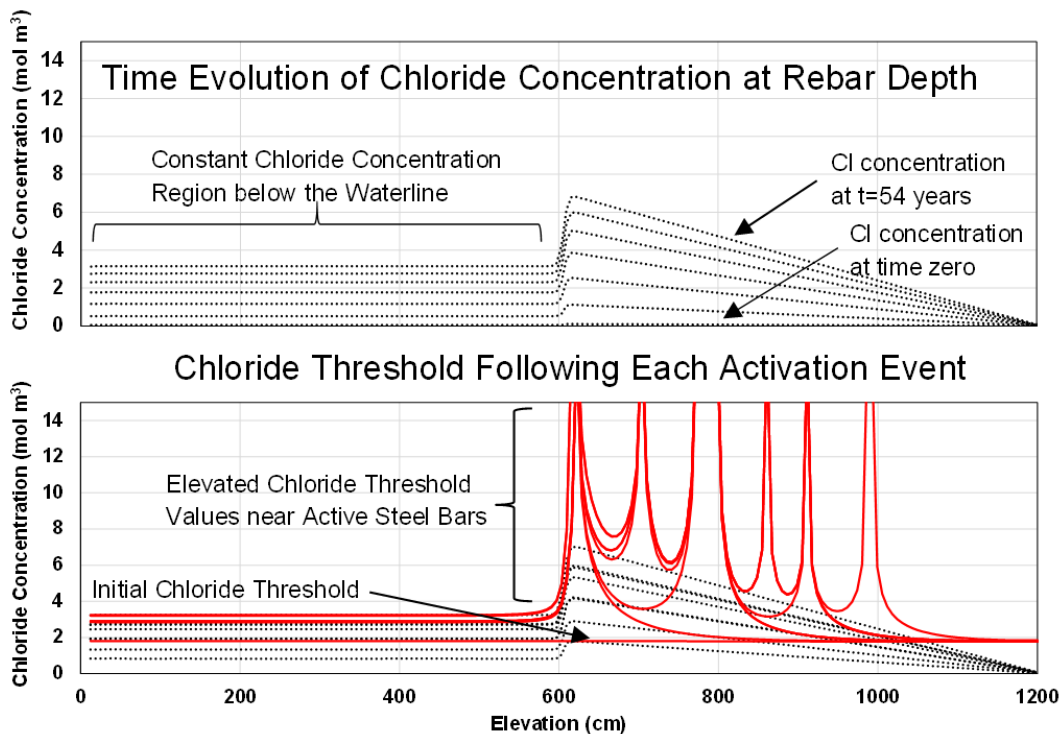


Figure 33. Time evolution of chloride concentration and chloride threshold. Top shows chloride concentration at rebar depth at nine-year intervals. Bottom shows chloride threshold values (red lines) following each activation event. (Chart shows “Medium” chloride ion diffusivity for a simple surface chloride profile without random variability).

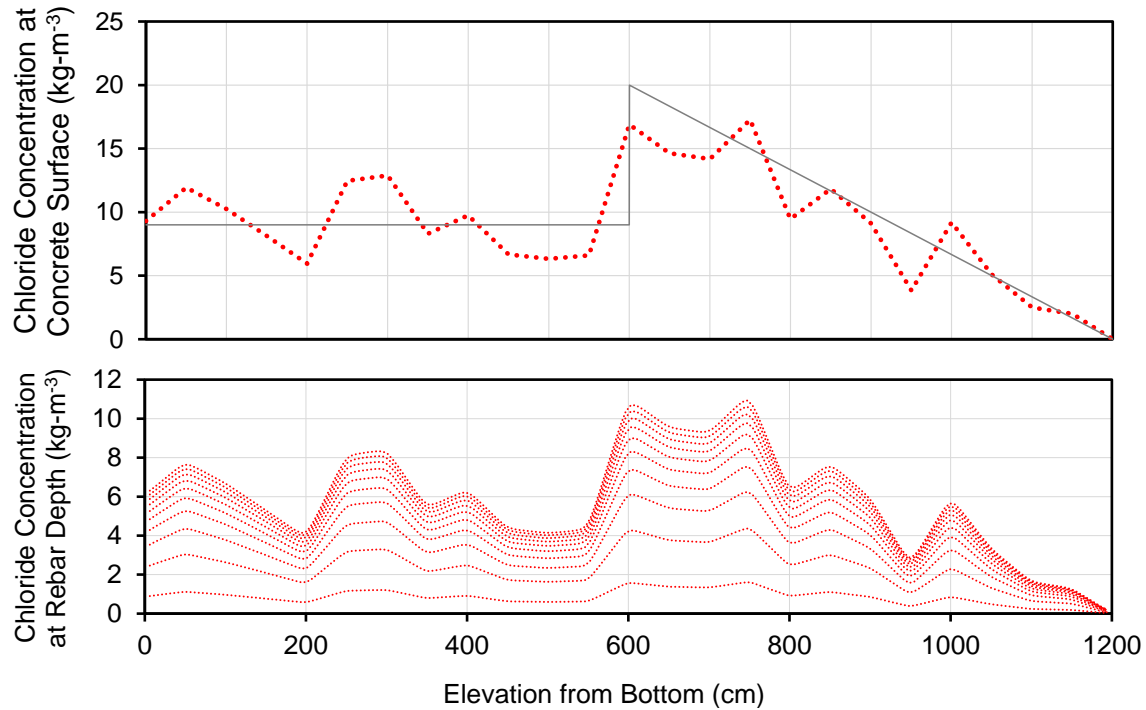


Figure 34. Chloride concentration. Top: C_s pattern for both the baseline profile (black solid line) and with spatially varied profile as used in the calculations (red dotted lines). Bottom: Evolution of the concentration profile at the rebar depth, illustrated for 10-year intervals for a medium chloride diffusivity realization.

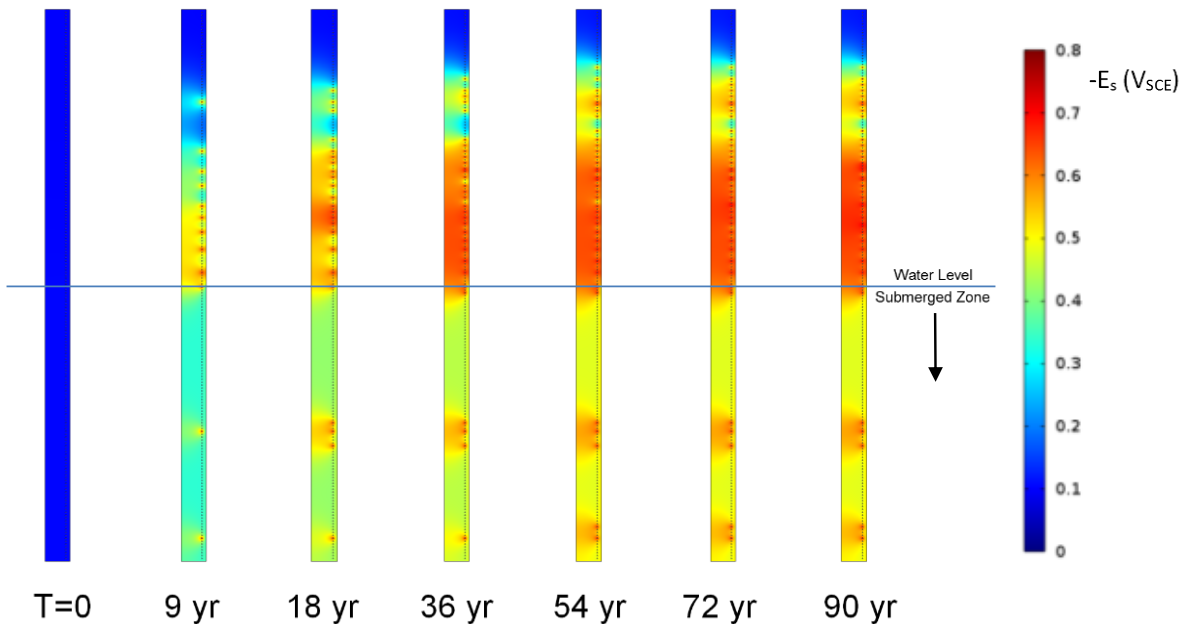


Figure 35. Potential distribution evolution with time for Case 1. Simulation used the randomly altered C_s pattern. Note early onset of corrosion in the submerged zone. Each individual potential map is shown in vertical column cross-section with the cylindrical symmetry axis on the left edge.

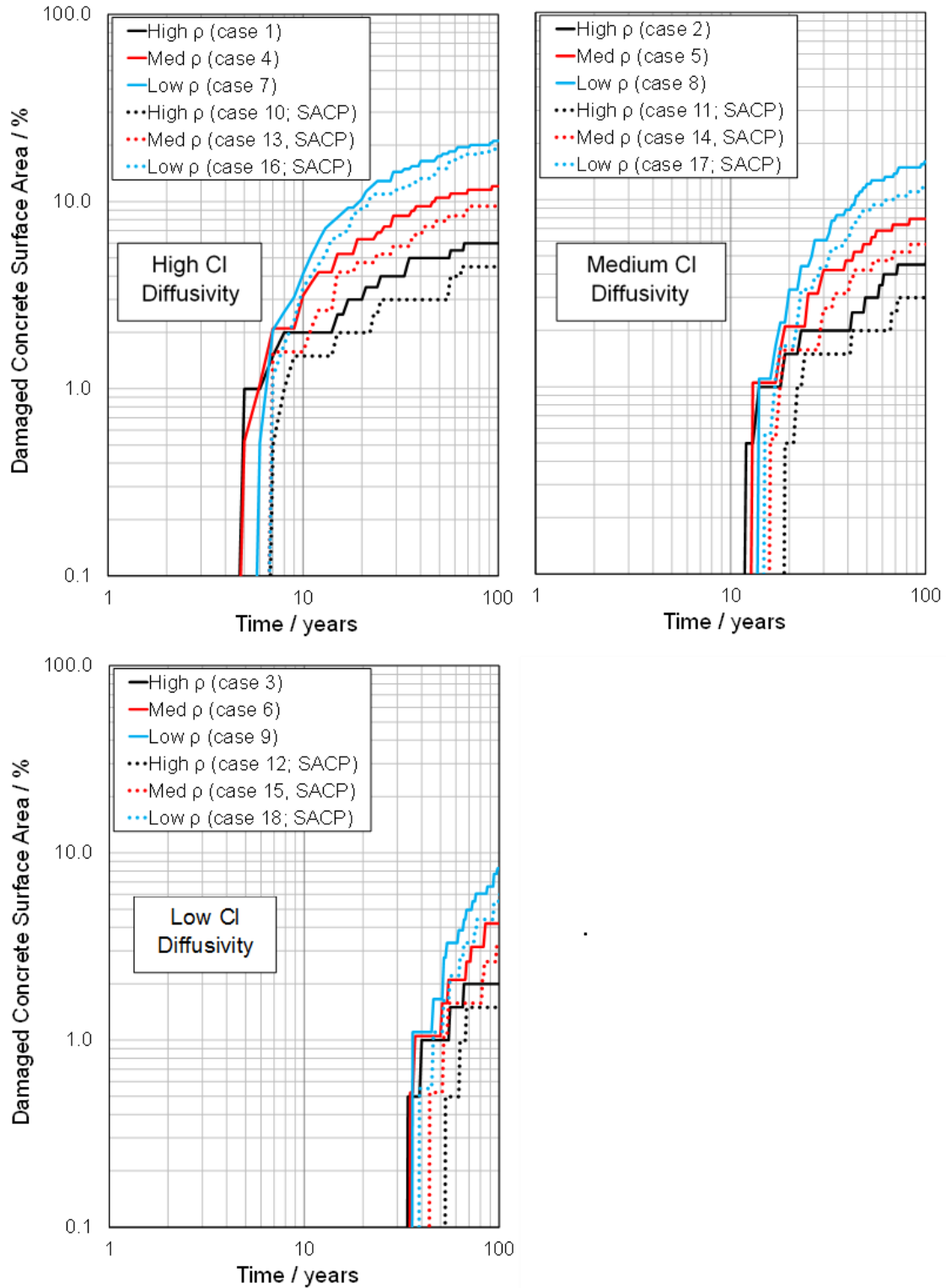


Figure 36. Damage functions using the above-water damage declaration criterion. Numbers in parentheses are keyed to cases listed in Table 7. The three charts represent damage given three different chloride diffusivities

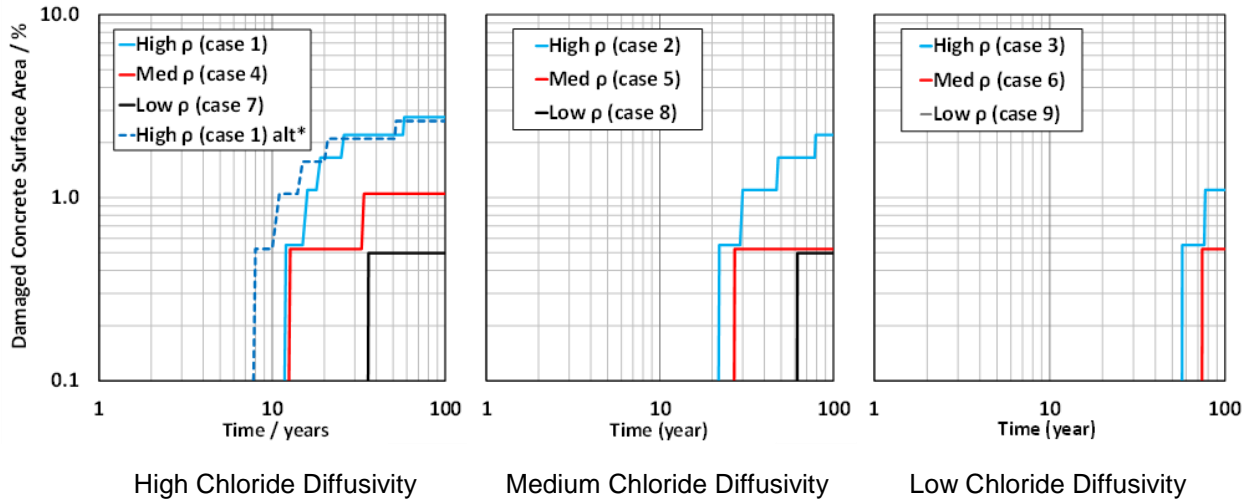


Figure 37. Damage functions using alternative damage declaration criterion. Results are based on percentage of entire column surface for the submerged portion only (alternative damage declaration criterion discussed in the text). Application of SACP projected complete suppression of corrosion damage in the submerged zone so curves for those cases are not shown.

*Dashed line for Case 1 is projection with $P_{crit} = \sim 100 \mu m$ shown for comparison.

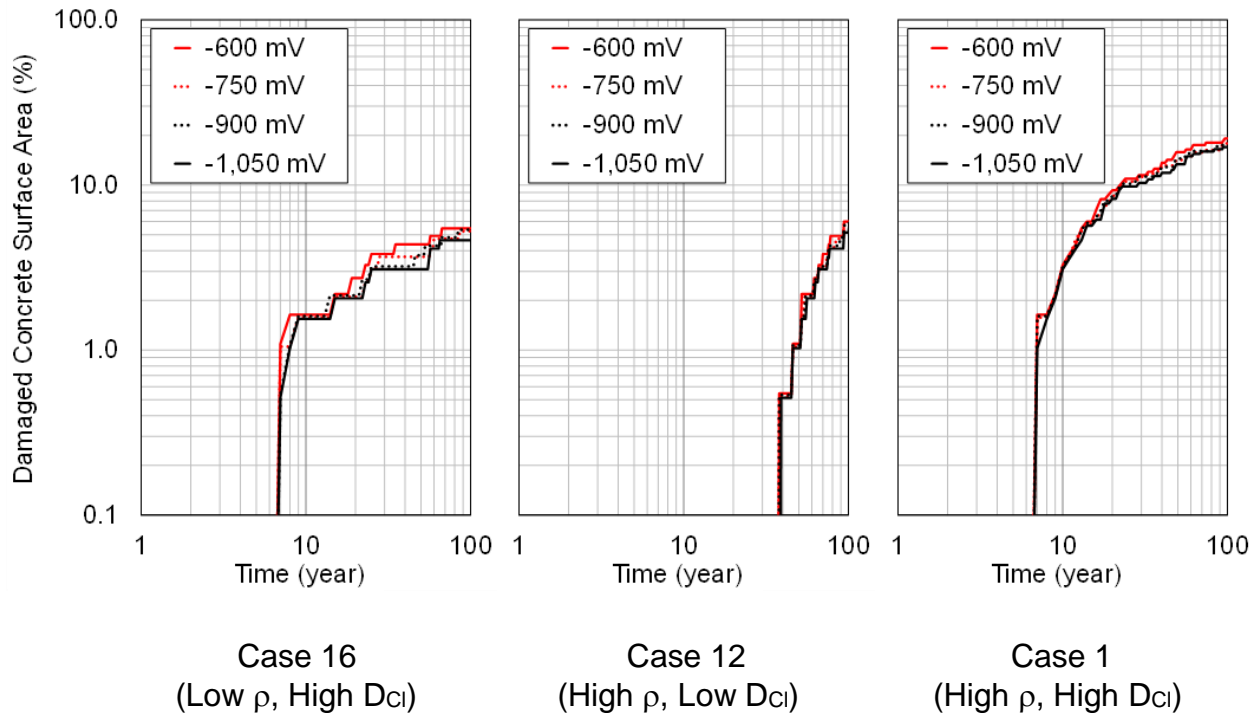


Figure 38. Damage functions for alternate anode potentials. ($E_{Prot} = -600, -750, -900,$ and $-1,050$ mV SCE for selected cases.) Note minimal sensitivity of damage projections to anode potentials in the given range.

CHAPTER 5: RECOMMENDED FUTURE RESEARCH

This investigation has provided information related to the modality and rate of corrosion of steel reinforcement in marine submerged structural elements. The work has also generated a modeling tool that can be used to project corrosion initiation and propagation in new and existing structures and has further established prognosis for a possible means of submerged region corrosion control.

This information may be useful for the development of corrosion control strategies that can effectively increase the durability of many types of structural elements in a diverse inventory. The objectives of this investigation can be further advanced via the execution of the following recommendations for future research. The list below is not intended to be exhaustive and therefore could be favorably augmented by additional actions associated with these and other related developments.

1. Assess the structural and economic implications of the degree and type of corrosion considered here. The main modality of deterioration in the submerged zone is not likely to be cracking of the concrete cover, as is the case of above-water corrosion but instead, loss of rebar or strand cross-section with consequent loss of strength and bond. As suggested in the previous section and by others, [e.g., Thistlethwaite 2014] a strong need for the definition an alternative limit-state (i.e., other than visible external cracks and spalls) for submerged reinforced concrete remains. The amount of the

material loss and its evolution with bridge age can be projected using the dynamic evolution model or variations thereof, as noted below. Evaluation of any structure-weakening effects associated with steel cross-section loss of a given extent over a given length of steel was not within the scope of this project. Now that the presence and progression of corrosion has been established however, assessment of corrosion extent and effects should be assessed for various relevant pile configurations, dimensions, and modes of service loading. Both structural and engineering economic issues should be investigated. The relative importance of submerged zone corrosion compared to other modes of aging of structures should be established and future needs should subsequently be prioritized.

2. Consider the means by which sacrificial anode cathodic protection can be implemented in new-pile construction. The feasibility of fitting new piles with provisions for installation of cathodic protection anodes and interconnection of strands should be evaluated as part of the structural and economic analyses. Specific consideration should be given to pile design and the best practice by which external anode contacts could be installed based on pile size and configuration. If the results of the engineering and economic analyses indicate value in performing this work, guidelines should be formulated for the means to incorporate cathodic protection anodes into existing in-service piles.
3. Develop the dynamic corrosion evolution model further in order to remove existing assumptions and simplifications. The following areas represent some

of the more pressing issues that merit attention in order to create an even more realistic perspective on the system of interest:

3a. Effects of preexisting concrete cracking. This feature could be implemented beyond the present qualitative basis by replacing the given *Low, Med, and High* chloride diffusivity values with additional and more extreme diffusivity values. Quantitative treatment should assume a given incidence of cracking and should implement fast chloride penetration rates in cracked regions. The treatment used in some analogous studies [Lau et al. 2010, Busba and Sagüés 2013] may serve as an initial step.

3b: Statistical dispersion of additional system properties. The present model only addresses stochastic distribution of the surface chloride concentration. For a more-realistic representation of damage projection, variability of other parameters (especially concrete cover) should be introduced. These features would capture more accurately and more conservatively the early stages of damage development and improve rational selection of corrosion control alternatives and more accurate cost benefit analyses. The approach recently developed for FDOT in Project BDK84 977-09 [Sagüés and Sánchez 2014] is an example of a procedure that could be adopted for this purpose. Additional realizations with variations of the stochastic distribution themselves should also be conducted and the results averaged accordingly.

3c: Three-dimensional (3-D) representation. The present model assumes cylindrical geometry for simplicity, resulting in a simulated ring-pattern of

damage that is only a coarse representation of actual systems. The next-generation model should use a full 3-D geometry, which would have the added benefit of more precisely simulating corrosion damage development in square piles. This transition should be coupled with the statistical variability of parameters approach to better simulate the random development of corrosion damage. Moreover, allowance should be made for an activation delay after a chloride threshold value has been exceeded locally [Presuel-Moreno et al. 2005] and for the amount of time required for establishment of a new oxygen distribution pattern after each new activation event. In the present model both of these things are assumed, for simplicity, to be instantaneous compared to the time scale of the system evolution. Likewise and especially for thicker submerged components, the amount of corrosion that can be sustained by native oxygen content of the concrete should be considered.

3d: *Relevant tidal zone considerations.* As indicated in Section 2.1, the present model effectively simplified the tidal zone as a sharp transition from submerged to above-water regimes. While such an approximation may be partially justified for low-amplitude-tide regimes, it becomes increasingly deficient otherwise and an intermediate regime should be implemented accordingly in future simulations.

3e: *Anoxic and low-oxygen environments.* Phenomena such as the metabolism of Sulfate-Reducing Bacteria (SRB), shifts in water temperature, variations in salinity, photosynthesis, decomposition of

organic matter, and issues unique to oxygen-minimum zones (OMZs) can change the effective oxygen concentration in the bulk of the seawater and in seawater near the concrete surface beneath biofilms and/or larger surface-adhered organisms. [Thistlethwaite 2014, Shifler and Aylor 2005, Levin 2002] Bulk phenomena can be especially relevant in systems that use long structural elements that span significant water depths e.g., offshore oil platforms. Future studies that vary parameter values and introduce representation of other phenomena in the current models should be conducted accordingly.

4. Increase the knowledge-base of field observations. Due to limited opportunities during the execution period, this investigation only examined piles from aged bridges, mostly with highly permeable concrete. As new opportunities arise, samples of extracted pilling from a wider variety of bridge types and ages should be sought and examined. Of special interest would be decommissioned piles made with more-recent, less-permeable concrete formulations representative of present and future construction.

CHAPTER 6: CONCLUSIONS

- Severe localized corrosion of steel can occur in the submerged portions of reinforced concrete structures in marine environments. Field studies of decommissioned piles from marine bridges revealed multiple instances of strong corrosion localization, showing appreciable local loss of steel cross-section. The observed patterns are consistent with observations made in other similar exploratory field investigations.
- Quantitative understanding of the phenomenon and its causes was developed via a steady-state corrosion distribution model. Cathodic reaction rates under oxygen diffusional limitation that are negligible in the submerged region in cases of uniform corrosion can support substantial corrosion rates if corrosion is localized. Corrosion rates projected by the model were consistent with corrosion documented in field assessments.
- The steady-state model projections indicated that eliminating corrosion in the splash/evaporation zone could in some cases increase corrosion vulnerability of steel in the submerged region.
- Dynamic modeling of a notional partially submerged marine reinforced concrete column supported the proposition that the passive state of a large portion of the steel can be preserved in the presence of high chloride concentration at rebar depth, even if typical assumed chloride threshold values were exceeded. This can be attributed

to the threshold dependence on local steel potential. The model projections of corrosion extent and localization were also consistent with the findings of field assessments.

- Calculations indicated that high concrete resistivity, which is typical in low permeability concrete chosen for achieving long service-life in the above water region, may under certain conditions promote unintended corrosion vulnerability of the submerged region by lowering the extent of beneficial macrocell coupling there.
- Model simulations projected that Sacrificial Anode Cathodic Protection for partially submerged marine reinforced concrete structural elements could effectively eliminate corrosion in the submerged zone and simultaneously provide some measure of protection for steel in the splash/evaporation zone.

REFERENCES

- C. Alonso, M. Castellote, C. Andrade, and P. Castro, "Chloride Threshold Values to Depassivate Reinforcing Bars Embedded in a Standardized OPC Mortar," *Cement and Concrete Research*, vol. 30 (2000): p. 1047.
- C. Andrade, C. Alonso, J.A. González, and J. Rodríguez, "Approximate Calculation of Service Life of Corroding Structures Using Polarization Resistance Measurements," *CORROSION/1990*, paper no. 319 (Houston, TX: NACE, 1990).
- U. Angst, O. Vennesland, R. Myrdal, "Diffusion Potentials as Source of Error in Electrochemical Measurements in Concrete", *Materials and Structures*, Vol 42. pp. 365-375 (2009).
- K.Y. Ann, H.W. Song, "Chloride threshold level for corrosion of steel in concrete," *Corrosion Science* 49, 11 (2007): p. 4113.
- ASCE. American Society of Civil Engineers. Report Card for America's Infrastructure. Available online at <http://www.infrastructurereportcard.org/>
- ASTM C642-13, "Standard Test Method for Density, Absorption, and Voids in Hardened Concrete" (West Conshohocken, PA: ASTM, 2006).
- ASTM C876-09, "Standard Test Method for Half-Cell Potentials of Uncoated Reinforcing Steel in Concrete" (West Conshohocken, PA: ASTM, 2009).
- J.L. Beaton, D.L. Spellman, R.F. Stratfull, "Corrosion of Steel in Continuously Submerged Reinforced Concrete Piling," 46th Annual Meeting of the Highway Research Board, Report No. M&R 635116, California Division of Highways in cooperation with the U.S. Department of Commerce, Bureau of Public Roads, 1967.
- L. Bertolini, B. Elsener, P. Pedefferri, R. Polder, *Corrosion of Steel in Concrete: Prevention, Diagnosis, Repair* (Weinheim, Germany: Wiley-VCH, 2004), p. 356.
- J.P. Broomfield, *Corrosion of Steel in Concrete: Understanding, Investigation and Repair*, 2nd ed. (New York, NY: Taylor and Francis, 2007), p. 9.
- E. Busba, A.A. Sagüés, "Localized Corrosion of Embedded Steel in Cracked Reinforced Concrete Pipes," *CORROSION* 69 (2013): p. 403.

L. Cáseres, A.A. Sagüés, S.C. Kranc, R.R. Weyers, "In-Situ Leaching Method for Determination of Chloride in Concrete Pore Water," *Cement and Concrete Research* 36 (2006): p. 492.

L. Coppola, R. Fratesi, S. Monosi, P. Zaffaroni, M. Collepari, "Corrosion of Reinforcing Steel in Concrete Structures Submerged in Seawater," Third CANMET/ACI International Conference on Performance of Concrete in Marine Environment, SP 163-5 (Farmington Hills, MI: ACI, 1996), pp. 127, 134, 138.

"Corrosion Condition Evaluation of Bridge Substructure Bridge Nos. 139002, 139003, 159007, and 159008," Florida Department of Transportation Corrosion Research Laboratory, 2002.

J. Davenport and S. Irwin, "Hypoxic Life of Intertidal Acorn Barnacles," *Marine Biology* 143 (2003) pp. 555-563.

M. Eashwar, G. Subramanian, P. Chandrasekaran, and K. Balakrishnan, "Mechanism for Barnacle-Induced Crevice Corrosion in Stainless Steel," *Corrosion* vol. 48 no. 7 (1992).

B. Elsener, C. Andrade, J. Gulikers, R. Polder, M. Raupach, "Half-Cell Potential Measurements – Potential Mapping on Reinforced Concrete Structures," *Materials and Structures* 36 (2003): p. 461.

Figg Bridge Inspection, Inc. "Sunshine Skyway Bridge Specialty Engineers Report" (2013).

Florida Department of Transportation, "Structures Manual," <http://www.dot.state.fl.us/structures/StructuresManual/CurrentRelease/StructuresManual.shtm>.

Florida Department of Transportation, "Bridge Environment Data," Available online at <http://www.dot.state.fl.us/statematerialsoffice/administration/resources/library/publications/bridge/environment.pdf> (September 18, 2015).

Florida Department of Transportation, "Technical special provision for cathodic protection of integral pile jacket system" Specification 4570000, (2010).

M. Fontana, *Corrosion Engineering*, 3rd ed. (New York, NY: McGraw-Hill, 1987), p. 66.

FSTM FM 5-516, "Florida Method of Test For Determining Low-Levels of Chloride in Concrete and Raw Materials" (Tallahassee, FL: FDOT, 2010).

W.H. Hartt, C.C. Kumria, and R.J. Kessler, "Influence of Potential, Chlorides, pH, and Precharging Time on Embrittlement of Cathodically Polarized Prestressing Steel," *Corrosion Journal*, vol. 49, no. 5 (1993): p. 377.

W. H. Hartt, A. Poeydomenge, A. Stauder, and W. Scannell, "Long-Term Effects of Cathodic Protection on Prestressed Concrete Bridge Components", Report No. FHWARD-98-075, Published by NTIS (1998).

W. H. Hartt and F. J. Presuel-Moreno, "Protection of Reinforced Concrete Bridge Substructures using Submerged Bulk Anodes," Final Report to Florida D.O.T., Project BD546-3, Florida Atlantic University, Boca Raton, FL (2009). Available online, www.dot.state.fl.us.

R.B. Holland, "Durability of Precast Prestressed Concrete Piles in Marine Environments," Doctoral Dissertation, Georgia Institute of Technology (2012).

D.A. Jones, *Principles and Prevention of Corrosion*, 2nd ed. (Upper Saddle River, NJ: Prentice Hall, (1995), p. 75.

G.H. Koch, M. Brongers, N.G. Thompson, Y.P. Virmani, J.H. Payer, "Corrosion Costs and Preventive Strategies in the United States" Report FHWA-RD-01-156, Contract: DTFH61-99-X-00004 (2002).

S.C. Kranc, A.A. Sagüés, "Computation of Reinforcing Steel Corrosion Distribution in Concrete Marine Bridge Substructures," *CORROSION* 50 (1994): p. 50.

K. Lau, A.A. Sagüés, R. Powers, "Corrosion of Epoxy Coated Rebar in Marine Bridges. Part II - Corrosion in Cracked Concrete," *CORROSION* 66 (2010): p. 065002.

K. Lau, A.A. Sagüés, R. Powers, "Corrosion of Epoxy Coated Rebar in Marine Bridges. Part II - Corrosion in Cracked Concrete," *Corrosion* 66 (2010): p. 065002.

Lawrence Livermore National Laboratory, *Accounting for Skin Effect and Nonlinear Permeability*, Lawrence Livermore National Laboratory, Report LLNL-PROC-491230, July 2011.

S. Lee, "Current State of Bridge Deterioration in the U.S. – Part 1," *Materials Performance*, vol. 51, pp. 62-67, 2012.

L.A. Levin, "Deep-Ocean Life where Oxygen is Scarce," *American Scientist* vol. 90, 5 (2002).

Y. Liu, R.R. Weyers, "Modeling the Time to Corrosion Cracking in Chloride Contaminated Reinforced Concrete Structures," *ACI Materials J.* 95, 6 (1998): p. 675.

P. Pedferri, "Cathodic Protection and Cathodic Prevention," *Construction and Building Materials* 10, 5 (1996): p. 391.

A. D. Pergola, F. Lollini, E. Redaelli, and L. Bertolini (2013) Numerical Modeling of Initiation and Propagation of Corrosion in Hollow Submerged Marine Concrete Structures. *CORROSION* 69 no. 12 (2013) p. 1158.

M.P. Perkins, M.M. Ong, C.G. Brown, R.D. Speer, "Analysis of Conductor Impedances F.J. Presuel-Moreno, A.A. Sagüés, S.C. Kranc, "Steel Activation in Concrete Following Interruption of Long Term Cathodic Polarization," *CORROSION* 61 (2005): p.428.

F. J. Presuel-Moreno, S.C. Kranc, A.A. Sagüés, "Cathodic Prevention Distribution in Partially Submerged Reinforced Concrete", *CORROSION* 61 (2005): p. 548.

M. Raupach, "Investigations on the influence of oxygen on corrosion of steel in concrete – Part 1," *Materials and Structures* 29 (1996): p. 143.

P. Roberge, *Corrosion Engineering: Principles and Practice* (New York NY: McGraw-Hill, 2008).

A.A. Sagüés, H. Perez-Duran, R. Powers, "Corrosion Performance of Epoxy-Coated Reinforcing Steel in Marine Substructure Service", *Corrosion*, Vol 47, p.884, (1991).

A.A. Sagüés, J.B. Lee, X. Chang, H. Pickering, E. Nystrom, W. Carpenter, S.C. Kranc, T. Simmons, B. Boucher, S. Hierholzer, *Corrosion of Epoxy Coated Rebar in Florida Bridges*, Final Report to Florida D.O.T. WPI 0510603, University of South Florida, Tampa, FL, 135 pp. (1994).

A.A. Sagüés, E. Moreno, W. Morris, C. Andrade, "Carbonation in Concrete and Effect on Steel Corrosion," Florida Department of Transportation, State Job No. 99700-3530-119, WPI 0510685, June (1997).

A. A. Sagüés, S.C. Kranc and F.J. Presuel-Moreno, "Advanced Computational Model for Sacrificial Cathodic Protection of Partially Submerged Reinforced Concrete Marine Footers", p.1, in *Repair and Rehabilitation of Reinforced Concrete Structures: The State of the Art*, W.P. Silva-Araya, O. T. de Rincon and L. Pumarada O'Neill, Eds., ASCE, Reston, VA, (1998).

A.A. Sagüés, S.C. Kranc, F.J. Presuel-Moreno, D. Rey, A. Torres-Acosta, and L. Yao, "Corrosion Forecasting for 75-Year Durability Design of Reinforced Concrete," Final Report to Florida D.O.T. WPI 0510805. University of South Florida, Tampa, FL (2001) Available online at www.dot.state.fl.us.

A.A. Sagüés, M.A. Pech-Canul, S. Al-Mansur, "Corrosion Macrocell Behavior of Reinforcing Steel in Partially Submerged Concrete Columns," *Corrosion Science* 45 (2003): p. 7.

A.A. Sagüés, S.C. Kranc, K. Lau, "Service Life Forecasting for Reinforced Concrete incorporating Potential-Dependent Chloride Threshold," *CORROSION/2009*, paper no. 09213 (Houston, TX: NACE International, 2009), p. 22.

A. A. Sagüés, M. T. Walsh, M. A. Paredes, "Corrosion in Submerged Marine Bridge Substructure," (Presentation P12-5139), Transportation Research Board 91st Annual Meeting, Washington, D.C., January 22-26, 2012.

A.A. Sagüés, A.N. Sánchez, K. Lau, S.C. Kranc, "Service Life Forecasting For Reinforced Concrete Incorporating Potential-Dependent Chloride Threshold," *CORROSION* 70 (2014): p. 942.

A.A. Sagüés and A.N. Sánchez, "Modeling Reinforced Concrete Durability," Florida Department of Transportation, Contract No. BDK84 977-09, June 2014.

A.A. Sagüés and M.T. Walsh, "Durability Performance of Submerged Concrete Structures - Phase 2," Florida Department of Transportation, Contract No. BDV25 977-12, September 2015.

A.N. Sánchez, "Forecasting Corrosion of Steel in Concrete, Introducing Chloride Threshold Dependence on Steel Potential," Doctoral Dissertation, University of South Florida (2014).

A.N. Sánchez and A.A. Sagüés, "Chloride Corrosion Threshold Dependence on Steel Potential in Reinforced Concrete," *CORROSION/2014*, paper no. 4118 (Houston, TX: NACE, 2014a).

A.N. Sánchez and A.A. Sagüés, "Some Open Issues in Forecasting Corrosion Risk of Steel in Concrete," *CORROSION* 70 no. 11 (2014b): p. 1148.

A.N. Sánchez and A.A. Sagüés, "Probabilistic Corrosion Forecasting of Steel in Concrete with Potential Dependent Chloride Threshold," pp. 408-413 in Proceedings of the 1st International Conference on Ageing of Materials & Structures, K. van Breugel and E.A.B. Koenders, Eds., Delft University of Technology, Delft, The Netherlands (2014c).

R. Sangeetha, R. Kumar, M. Doble, R. Venkatesan, "Barnacle cement: An etchant for stainless steel 316L?" *Colloids and Surfaces B: Biointerfaces* vol. 79 (2010).

D.A. Shifler and D.M. Aylor, *Corrosion Tests and Standards, Application and Interpretation*, 2nd ed., edited by Robert Baboian (West Conshohocken, PA: ASTM, 2005) Chapter 30: Seawater.

F.A. Simon, "Improvement of the Analysis of the Biochemical Oxygen Demand (BOD) of Mediterranean Seawater by Seeding Control" *Talanta* 85, pp. 527-532 (2011).

C. Thistlethwaite, "Behaviour of Massive Reinforced Concrete Sections in Seawater," Doctoral Dissertation, University of Dundee (2014).

J. Tinnea, "Structural Steel and Concrete, Localized Corrosion," Presentation at CORROSION 2012, TEG053X Committee Meeting (2012).

A. Torres-Acosta, A.A. Sagüés, "Concrete Cracking by Localized Steel Corrosion - Geometric Effects," *ACI Materials Journal* 101 (2004): p. 501.

K. Tuutti, *Corrosion of Steel in Concrete* (Stockholm: Swedish Cement and Concrete Research Institute, 1982), p. 145.

USGS TWRI Book 9–A7 (Third Edition) Five-Day Biochemical Oxygen Demand (11/2003), p. 11. Available online at https://water.usgs.gov/owq/FieldManual/Chapter7/NFMChap7_2_BOD.pdf.

M.T. Walsh and A.A. Sagüés, "Steel Corrosion in Submerged Concrete Structures - Part 2: Modeling of Corrosion Evolution and Control," Submitted for publication in *CORROSION* (2015).

APPENDIX A: INITIAL CHLORIDE ANALYSIS, BRIDGE A

An initial/preliminary concrete chloride analysis that used concrete fragments instead of core slices was conducted prior to the analysis described in Chapter 2. Fragments were selected from various locations on the exterior surface of the pile including: (1) a region where significant corrosion was observed, as indicated by the presence of corrosion damage and corrosion products, and (2) a region that was immediately adjacent to the region where significant corrosion was observed and that was itself devoid of any visible corrosion damage or products.

The specimen preparation process involved securing a concrete fragment on a mill table, drilling into the concrete at precisely marked locations thus generating pulverized/powdered concrete spoil, collecting the pulverized/powdered concrete via a specialized powder collection system, then dividing the powder into three equal parts.

Individual specimens were collected at multiple depths that represented the outermost region (just below the outer, seawater-exposed surface of the concrete), the innermost region (just above the embedded rebar), and the intermediate region. Concrete cover thickness averaged approximately 7.5 cm. Each triplicate concrete powder specimen was analyzed according to FM 5-516, Florida Method of Test Determining Low-Levels of Chloride in Concrete and Raw Materials. [FDOT 2010] Results of the analysis are presented in Table A1 and Figure A1.

Table A1. Observed chloride concentrations. (Note that disintegration of the concrete sample prevented data collection at 5 and 25 mm in the corroded rebar region.)

Average Distance from Outer Surface [mm]	Chloride Concentration [lb/yd ³], Non-corroded Rebar Region	Chloride Concentration [lb/yd ³], Corroded Rebar Region
5	21.3	-
25	16.3	-
45	17.1	19.2
65	27.1	29

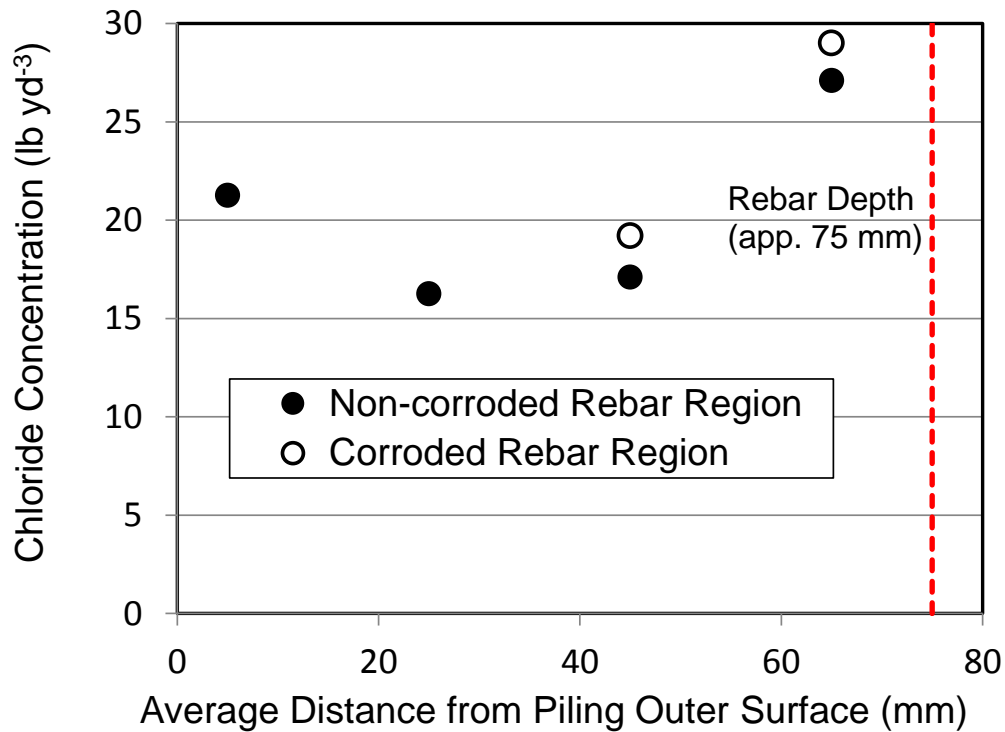


Figure A1. Observed chloride concentrations.

The results indicated that the distribution of chloride did not vary dramatically throughout the concrete cover. This can be attributed to the long seawater exposure duration (approximately 60 years) of the pile. The roughly uniform chloride distribution

precluded computation of a concrete apparent diffusion coefficient (D_{Cl}) value. It is noted however that the value of D_{Cl} must have been significantly greater than the values associated with modern highly impermeable FDOT concrete formulations which typically yield $D_{Cl} < 0.01 \text{ in}^2/\text{y}$ ($\sim 2 \times 10^{-9} \text{ cm}^2/\text{sec}$), and would have resulted in a profile decaying to $\sim 1/2$ of the surface concentration at a depth of $\sim 20 \text{ mm}$ after 60 years.

These findings are consistent with the expectation that concrete formulations in use several decades ago in applications of this type would have values of D_{Cl} that are one or even two orders greater than those of the modern materials. The higher chloride concentrations observed near the rebar could be attributed to transport obstruction effects.

APPENDIX B: POTENTIAL MAPPING, BRIDGE A

An exploratory half-cell potential measurement and mapping operation was conducted prior to the removal of bars 1a, 1b, 2b, 2c, and 2d. Note that bar 2a had been extracted prior to the establishment of a reliable potential measurement method.

Before any of the rebar-exposing saw cuts were made in the concrete of each pile, stainless steel screws were installed on the exposed end of each bar to serve as a low-resistance electrical contact point. The half-cell electrical potential (vs Cu/CuSO₄ reference electrode) was measured according to ASTM C 876. Two potential maps were made for each bar. One map followed a line parallel to the corner edge of the pile (offset by approximately 4 inches) along the “top” surface of the pile and the other map followed a similarly offset line along the “side” surface of the pile.

Figure B1 presents the half-cell potential measurement results along the length of each bar. Note that the corrosion rate estimated from the steel bar longitudinal resistance measurements described in Section 2.2 (and presented graphically in Figure 18) is included also, for reference. The regions with high estimated corrosion rate for bars 2b and 2c corresponded with regions of high visible section loss, as noted earlier.

As can be seen in the figure, all half-cell potential values were highly negative, consistent with an expectation of active corrosion of the steel. There was some apparent minor correlation between potential variations and the location of the highly corroding spots. The correlation was however in the opposite of the expected direction

(which would have resulted in somewhat more negative potentials in the area of greatest corrosion). The reason for these local discrepancies has not been established. It can be speculated nevertheless that the presence of corrosion products and pH variations in the highly corroded regions may have introduced local junction potentials that acted to result in a small excursions toward less negative values [Angst et al. 2009].

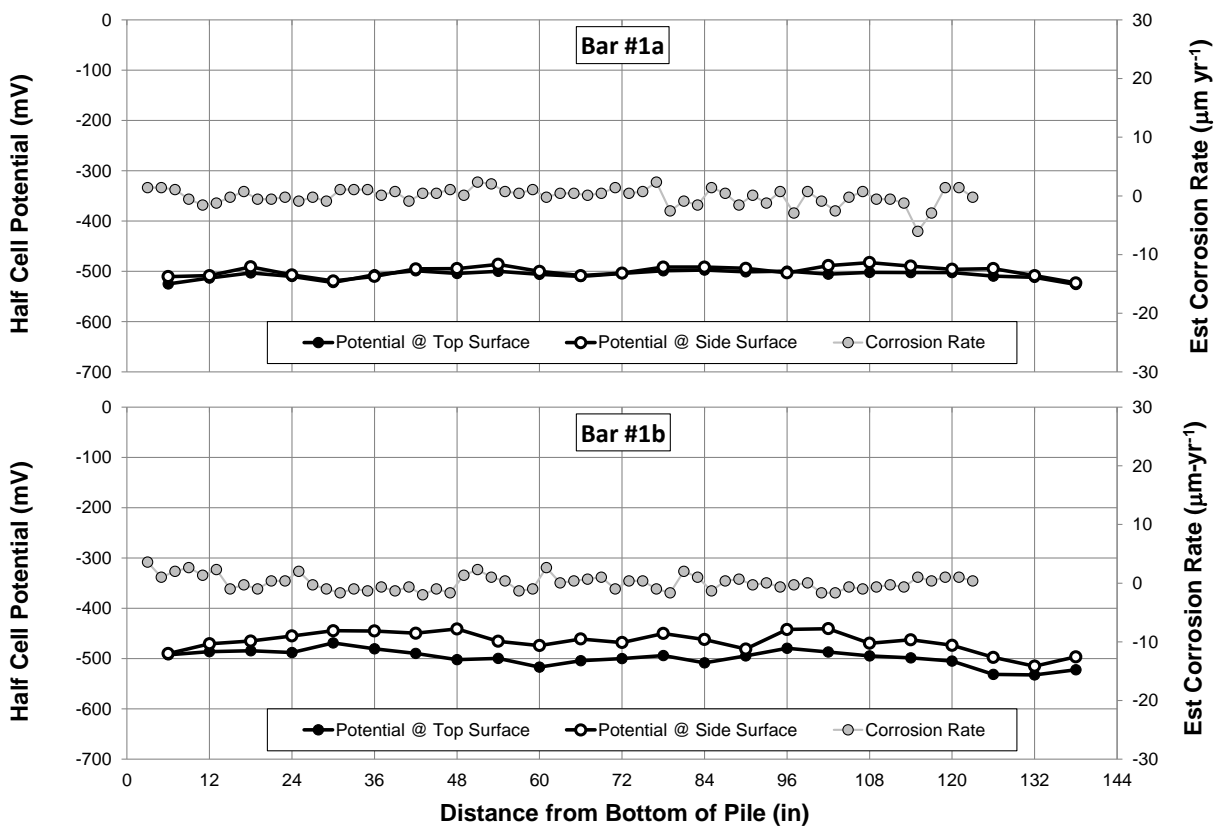


Figure B1. Half-cell potential at 6-inch intervals. Note that estimated corrosion rate from Figure 18 is presented for reference.

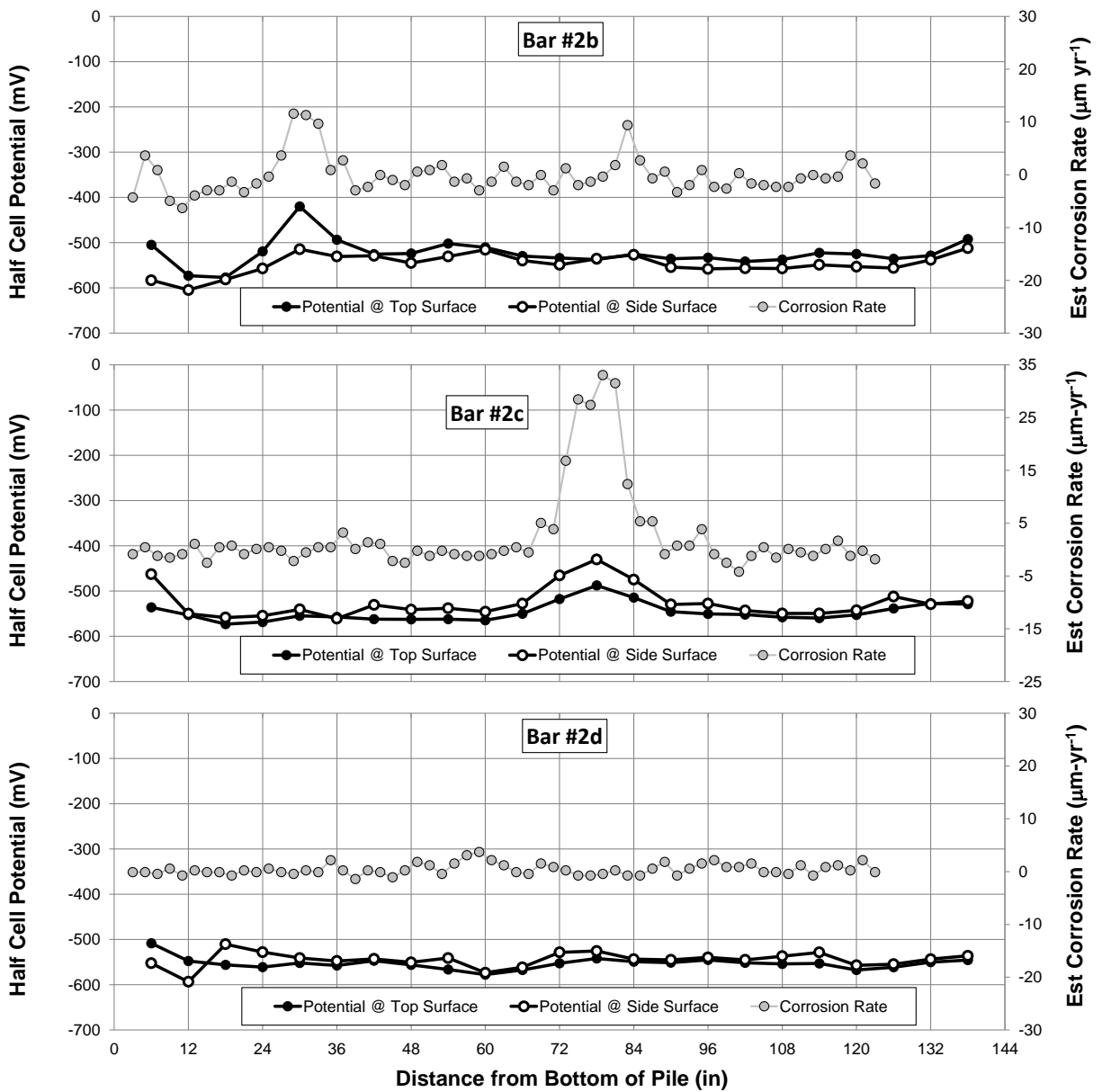


Figure B1 (continued).

APPENDIX C: SUNSHINE SKYWAY BRIDGE PIER FOOTERS

The work described below was performed as part of an examination of a structure with a time-in-service of approximately one half that of the structures from the field assessments described in Chapter 2. The results of that examination were regarded as relevant to the objectives of this dissertation and for that reason are included here.

C.1 Background

The Bob Graham Sunshine Skyway Bridge (FDOT Bridge Number 150189) spans the mouth of Tampa Bay and was opened for vehicle traffic in 1987. The bridge design features two concrete pier footers, each with geometry that includes an inner chamber portion that is normally filled with seawater. Filling the chambers with seawater was intended to prevent evaporative chloride enrichment at the concrete surface (to delay corrosion initiation) and slow oxygen ingress to the reinforcement (to make the overall corrosion rate slow after initiation of corrosion). Of special interest was the use of epoxy-coated rebar in the fact that the reinforcement in that bridge is epoxy-coated. Note that epoxy-coated rebar is no longer specified for use by FDOT but has been used in over 300 FDOT structures.

Each chamber is emptied on four-year intervals and the reinforced concrete that forms the interior of the chamber is directly inspected for corrosion-related damage. At the midpoint of each four-year interval, the concrete is re-inspected but the inspection is

performed by divers to avoid having to empty the chambers of seawater. The author participated in a recent empty-chamber inspection and then had the opportunity to collect additional relevant data two years later in conjunction with a filled-chamber/dive inspection.

C.2 Empty-Chamber Inspection

An empty chamber inspection of each of the two pier footers was performed during the week of October 15, 2012. In the week that preceded the inspection, and while the footers were still in their normal seawater-filled condition, dissolved oxygen (DO) content and resistivity of the water in the pier footers were measured with a probe at depth intervals of 3 feet between the datum surface (manhole cover deck) and the bottom (floor) of each pier footer. In addition, pier footer water samples were collected both before and at the commencement of dewatering. During the week of the inspection, three cores were extracted by FDOT personnel from the south pier (pier number 111) and two cores were extracted from the north pier (pier number 112). Half-cell potential measurements were made in the local areas of the core extraction sites and samples of water emerging from the cracks on the interior walls of the pier footers were collected.

C.2.1 Methods and Results

C.2.1.1 Pier Footer Water Analysis

On October 9, 2012, the dissolved oxygen content of the water in both (north and south) pier footers was measured at 3 ft intervals between each respective manhole cover deck and footer bottom (floor) using an Extech DO600 oxygen sensor. The lowest observed oxygen levels (~ 0.05 ppm) were found at the bottom of each pier and

the highest observed levels (~0.80 ppm) were found near the top (free) surface. A sample of water was collected at the free surface in each pier footer and subsequently analyzed at the USF Corrosion Laboratory (Table C1).

Table C1. Sunshine Skyway pier footer water laboratory analysis results. (9-9-2012) (Note that the disparity between DO observed on-site and DO observed in the laboratory can likely be attributed to oxygen uptake during sampling and transportation.)

Water Sample Location	pH	Resistivity, ρ (Ω -cm)	Dissolved Oxygen, <i>on-site</i> (ppm)	Dissolved Oxygen, <i>laboratory</i> (ppm)
Pier 111 (south)	8.31	2,440	0.06	1.93
Pier 112 (north)	8.50	2,630	0.82	1.42

The observed oxygen levels in the pier footers differed significantly from typical oxygen levels in Tampa Bay itself (~ 6 to 8 ppm) and the observed resistivity values likewise differed significantly from the expected value (~ 25 Ω -cm). As resistivity is a primary indicator of salinity and salinity affects oxygen content measurement, a plan was implemented wherein resistivity would be measured coincidentally with a second measurement of DO at the same depth intervals as the initial measurements. The measurements were made on October 12, 2012 prior to dewatering and the results are presented graphically in Figure C1.

The oxygen values observed on October 12 corresponded with the values observed on October 9; the resistivity values measured on October 12 reflected an apparent salinity gradient between the free surface of the water and the footer chamber floor. Resistivity values observed at the free-surface corresponded with resistivity

values typically observed in fresh water while resistivity values observed at each footer floor matched values observed in water in Tampa Bay.

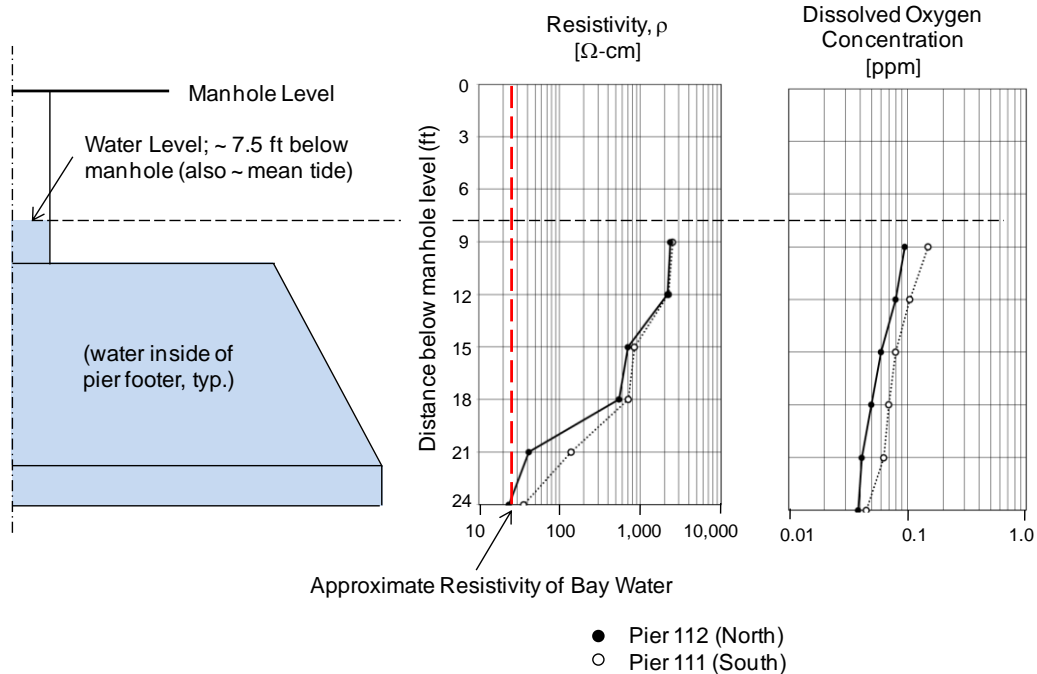


Figure C1. Resistivity and dissolved oxygen profiles. (October 12, 2012) The oxygen values observed on October 12 corresponded with the values

It was noted that, as the passivity breakdown of reinforcing steel is caused by the presence of chlorides, low chloride content of the water contained in the pier footers could be regarded as a favorable indicator of structural durability. As oxygen is required to support the cathodic reaction of depassivated steel, it was also noted that low oxygen content could likewise be regarded as favorable.

C.2.1.2 Post-dewatering Crack Seepage

Water that seeped into each pier footer through cracks during the inspection was collected and analyzed with respect to pH, resistivity, and dissolved oxygen (D.O.) content at the USF Corrosion Lab. Results of the analysis are presented in Table C2.

Table C2. Sunshine Skyway pier footer crack seepage water properties.

	pH	ρ [Ω -cm]	D.O. [ppm]
Bay Water	8.05	24.4	5.52
Crack Seepage, Pier 111 (south), sample A	7.85	500	6.42
Crack Seepage, Pier 111 (south), sample B	9.02	125	6.05
Crack Seepage, Pier 112 (north)	10.94	167	5.25

The observed elevated pH levels reflect a typical alkalinity increase caused by the mixing of crack seepage water with concrete pore water.

C.2.1.3 Coring

As indicated above, three 3-inch cores were extracted from the south pier (111). All cores within a given pier were extracted from positions in close proximity to each other. Core #1 was taken from a point along the centerline of crack #5 at a height of approximately 52 inches above the chamber “floor”. Core #2 was taken from a point offset (to the right) from the centerline of crack #5 by a distance of approximately 18 inches at a height of approximately 52 inches above the chamber “floor”. Core #3 was taken from a point offset (to the right) from the centerline of crack #5 by a distance of approximately 18 inches at a height of approximately 58 inches above the chamber “floor”. The extraction sites for core #s 2 and 3 were crack-free.

In all cases, coring was terminated upon reaching steel reinforcement and in each case, core extraction allowed visual access to the underlying rebar. Adhesion between the epoxy coating and the rebar was evaluated by scraping, to the extent possible with moderate effort, the coating from the bar with a sharp knife. Apparent loss of adhesion was indicated in the core #1 hole by the ease with which the epoxy coating

was removed from the exposed bar and also by the dark colored surface of the exposed bar (Figure C2). The epoxy coating on rebar in the core holes of core #s 2 and 3 appeared to be intact, but conditions onsite prevented the disbondment test from being conducted. Sharp knife tests conducted at the north site revealed poor adhesion in similar apparently intact coating.



Figure C2. Rebar at the bottom of hole at core #1. Before (left) and after (right) scraping epoxy coating with a sharp knife.

Two 3-inch cores were extracted from the north pier (112). Core #4 was taken from a point offset (to the right) from the centerline of crack #7 by a distance of approximately 6 inches at a height of approximately 72 inches above the chamber floor.

The core #4 site was crack-free. Core #5 was taken from a point along the centerline of crack #7 at a height of approximately 76 inches above the chamber floor.

As with core #s 1, 2, and 3, coring was terminated upon reaching steel reinforcement. The epoxy coating on bars at the bottom of core hole #s 4 and 5 appeared to be continuous and intact but when the epoxy coating on the rebar exposed by core #4 was cut with a sharp blade knife forming a triangular region, as in the case of core #1, the cut triangle was easily separated from the steel using the knife tip. This observation again indicated poor adhesion/bond between the coating and the rebar itself (Figure C3). Similar observation of poor adhesion was found at the rebar in the core #5 hole (Figure C4).



Figure C3. Rebar at core #4 site. Note epoxy cut and easily peeled showing poor adhesion.

The findings of poor epoxy coating adhesion and absence of visible corrosion in cores #4 and #5 are consistent with previous experience in examinations of marine epoxy-coated rebar in RC bridges in Florida, where coating disbondment has been observed for time-in-service periods of only a few years.

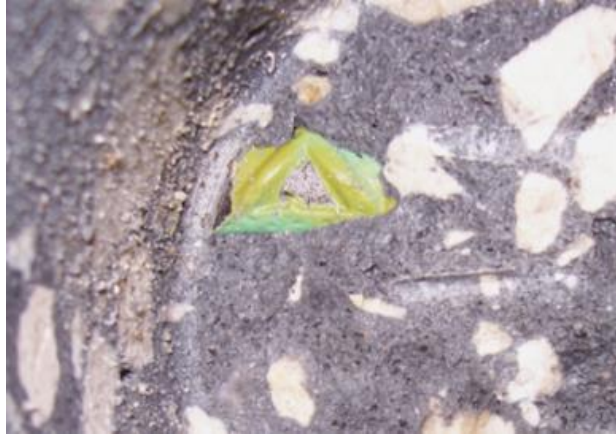


Figure C4. Rebar at core #5 site. Note poor adhesion of epoxy coating.

C.2.1.4 Core Analysis, General

Core dimensions, extraction site observations, and as-received (native moisture content) surface resistivity values (measured with a Wenner array probe with 2.5 cm spacing) are presented in Table C3.

Table C3. Core data.

Pier	FDOT Core #	Elevation Above Floor (in)	Core Length i.e. cover depth (in)	Core Site On Crack	Rebar Corrosion Observed	Epoxy Disbondment Observed	ρ , on line (k Ω -cm)	ρ , 120° CW (k Ω -cm)	ρ , 240° CW (k Ω -cm)
111 (S)	1	52	4.49	Y	Y	Y	26.1	26.2	23.5
111 (S)	2	52	5.24	N	N	N	23.3	27.0	24.8
111 (S)	3	58	5.91	N	N	N	29.7	29.8	26.5
112 (N)	4	72	4.49	N	N	Y	27.3	30.6	29.5
112 (N)	5	78	4.06	Y	N	Y	16.8	21.2	23.7

(Note: The “line” and associated angular offsets indicated in the surface resistivity headers refer to arbitrary measurement locations. Resistivity values reported include correction for finite specimen dimension and probe tip spacing. Y: Yes; N: No)

The concrete resistivity values were typical of those obtained in similar wet bridge substructures in previous surveys of bridges with comparable low permeability concrete. [Sagüés et al. 2001]

C.2.1.5 Core Analysis, Chloride

The depth at which chloride concentration would reach one half of the value observed at the exposed concrete surface was estimated to be approximately 0.50 inches according to $x_{1/2} \approx (D_{Cl} t)^{1/2}$ where t = nominal length of footer submersion i.e., ~25 years and $D_{Cl} = 2E-9 \text{ cm}^2/\text{sec}$, the expected typical chloride diffusivity for fully wet concrete in this Sunshine Skyway Bridge element. To obtain good profile resolution of chloride concentration as a function of depth, a milling scheme was developed to provide thin milling in the first 1/2 inch and thicker slices at greater depths. The slicing scheme shown is in Figure C5.

A special tiltable mounting jig was constructed to ensure that milling was true to the core face, which deviated somewhat from the core axis perpendicular. The arrangement is shown in Figure C6.

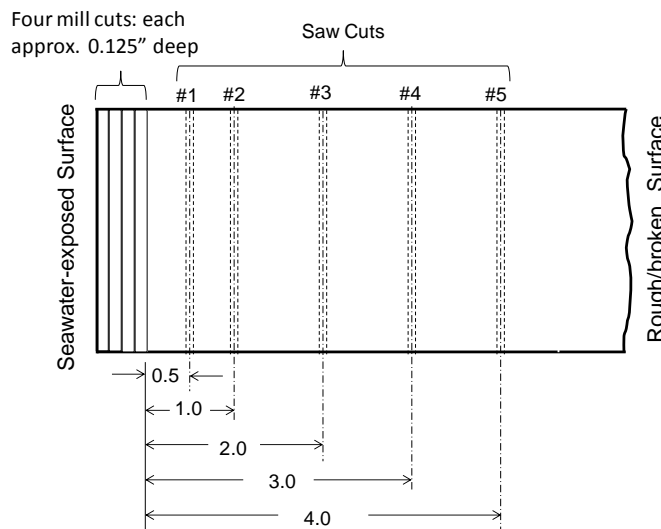


Figure C5. Core slicing scheme.



Figure C6. Core mounted on mill table.

Each powdered sample was divided into three equal portions for chloride analysis. Chloride analysis of the milled samples of Core #3 was conducted at the University of South Florida Corrosion Lab, and analysis of all remaining samples at the FDOT State Materials Office. Although the USF analysis of the milled samples of Core # 3 was conducted in accordance with FDOT FM 5-516, high inconsistency was observed among the triplicate results, likely due to subsequently discovered improper functioning of the silver/sulfide electrode used in the analysis.

The degree of inconsistency among each set of triplicate specimens was evaluated by the ratio of the difference between the maximum and minimum observed chloride content to the average chloride content of the triplicate fractions at each depth. Results are shown in Figure C7. The ratio approached or exceeded 1 (indicating a 100% scatter) in two cases for Core #3, while it was about 1/3 or less in all other cases. Consequently, the results from those two cases were declared outliers and not used for profile evaluation.

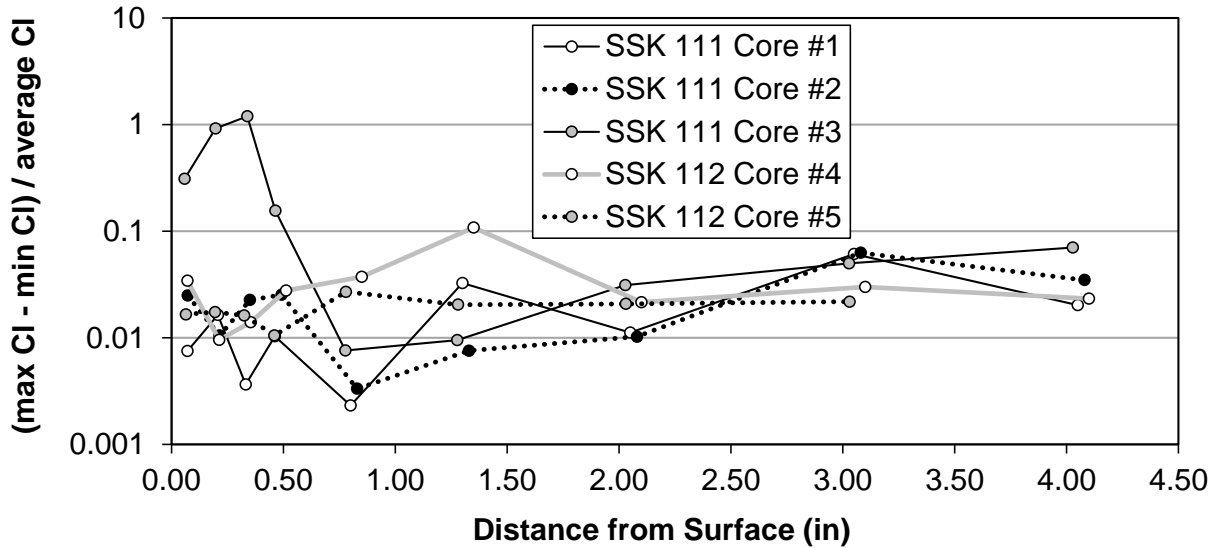


Figure C7. Degree of inconsistency. Ratio of the difference between the maximum and minimum chloride concentration values to the average chloride concentration value.

The resulting chloride profiles shown in Figure C8 indicated a decrease with depth as expected. It is noted that the results of the analysis of Core #s 1 and 5 (“on-crack” cores) presented higher low-depth chloride content than the other cores. However, even in those cases, the chloride content was less than $\sim 1/2$ of the values often seen in the splash/evaporation zone (e.g., 30 to 40 lb·yd⁻³), consistent with the expectation of a more moderate surface chloride content in fully submerged concrete.

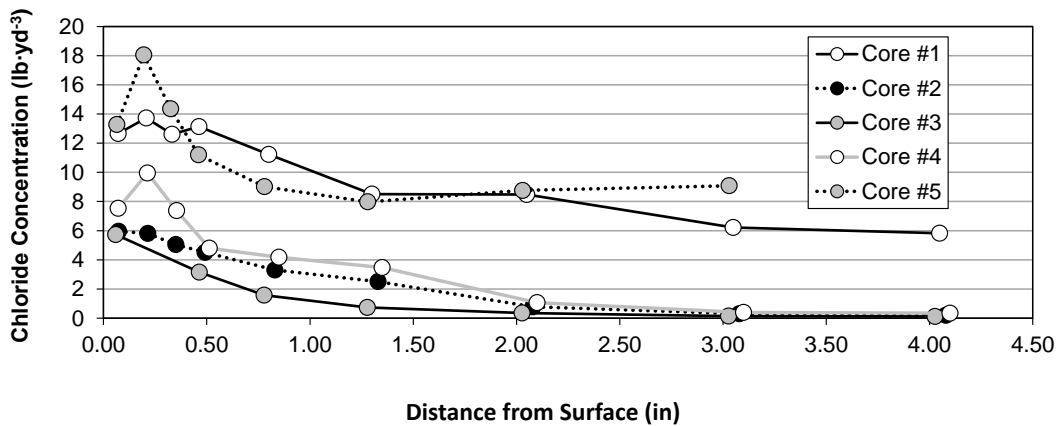


Figure C8. Chloride concentration. Concentration for each core is plotted as a function of distance from the outer/exposed surface.

Importantly, the on-crack cores showed not only greater surface chloride content than the others but also a much lower relative decrease in concentration with depth; concentrations at a depth of four inches for core #s 1 and 5 were approximately half of that at the surface, while for core #s 2, 3, and 4 concentration was more than 10 times smaller than that at the surface. This behavior is typical of enhanced chloride penetration at cracks, which had been documented earlier for splash/evaporation regimes at Sunshine Skyway. This effect is illustrated in Figure C9 comparing the chloride concentration profiles of various pairs of cores. The chloride content is shown in logarithmic scale to better emphasize relative concentration trends.

In addition to the core data analyzed in this study, data pairs for cores that were extracted from a cracked region of the structure (“on-crack”) and a companion core for each that was extracted from adjacent un-cracked (“sound”) concrete are shown. Each core in core pairs 1, 2, and 3 was extracted from Sunshine Skyway Bridge in 1997, as documented in Tables 3 and 5 of a previous FDOT report. [Sagüés et al. 2001]

These observations support evidence of strongly enhanced chloride penetration in the submerged chamber wall of the Sunshine Skyway footers.

C.3 Filled-Chamber Inspection

Resistivity of water in the Sunshine Skyway pier footers was once again measured at 3 ft intervals between the manhole-cover deck and footer bottom (floor) of each (North and South) pier footer during the filled-chamber footer inspection conducted on November 7, 2014. This work replicated the similar work conducted in 2012 described above. Neither oxygen nor temperature were recorded due to probe failure.

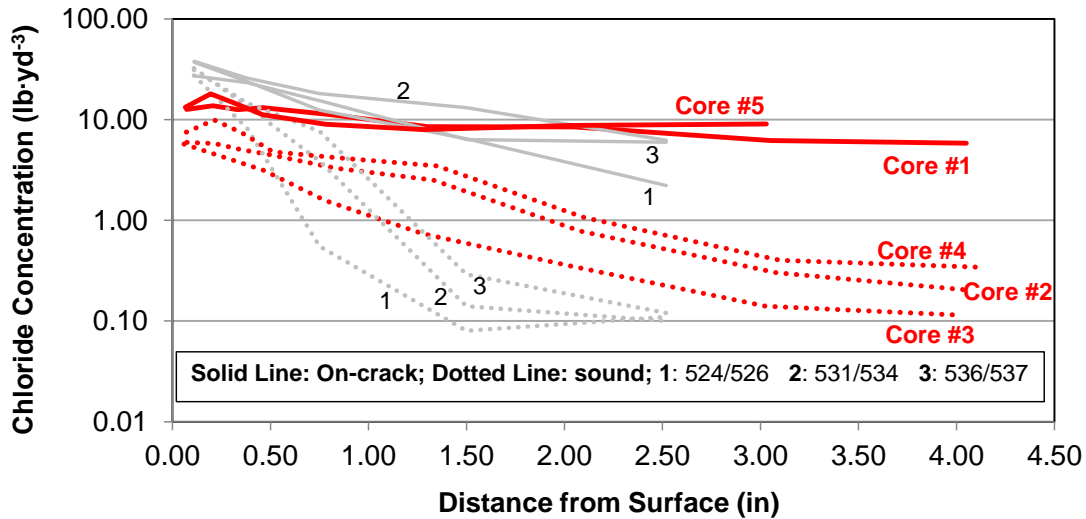


Figure C9. Comparison of chloride penetration in cores. Red lines indicate results from the current cores extracted from the chamber wall of Sunshine Skyway pier footers 111 and 112. The data associated with core pairs 1, 2, and 3 (extracted in 1997) and the numbers next to each pair (core designation codes) were taken from Sunshine Skyway splash/evaporation regimes described by Sagüés et al. [2001]. The two cores from each pier were taken from locations in close proximity to each other.

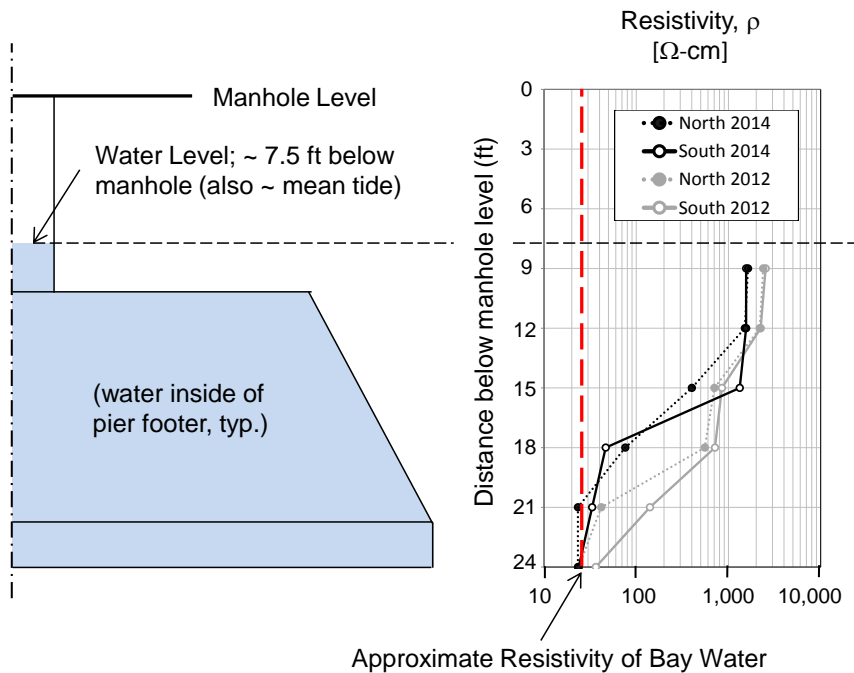


Figure C10. Resistivity of pier footer water. Results obtained November 7, 2014; Note that 2012 results shown for comparison.

C.4 Discussion

Both inspections (2012 and 2014) revealed general agreement between resistivity profiles in the North and South piers. Both surveys also revealed relatively high resistivity values of approximately 2,000 Ω -cm on the free-surface (i.e., water/atmosphere interface) of the water in each footer (indicative of low-salinity as would be found in freshwater) and much lower values of approximately 25 Ω -cm (roughly equivalent to those typically observed in Tampa Bay) in the water near the floor of each footer. The results indicate however a notable change in the depth at which the transition from high to low resistivity values took place. As shown in Figure C10, the transition observed in 2014 appears to be approximately three feet higher (i.e., closer to the surface) than that in the 2012 survey.

In 2012 it was suggested that the existence of a resistivity gradient could be explained by the apparent introduction of rainwater (essentially high-resistivity freshwater) into the pier footers incrementally in time and the subsequent incomplete mixing with the seawater already contained in the footers. In light of this explanation, the difference between 2012 and 2014 might be attributable to the difference in duration of the freshwater infiltration period. The 2012 survey had taken place four years after removal/refilling with water drawn from the bay (2008) whereas the 2014 survey took place only two years after the most recent refilling. When compared with previous results, the results from the 2014 study suggest that the transition depth might increase with time and would further suggest that a profile made in 2016 will be more similar to that of 2012. A report by Figg Bridge Inspection, Inc. [2013] addresses plausible means for rainfall concentration in that zone and supports the above interpretation.

Low dissolved oxygen values observed in 2012 implied the existence of a chemical or biological mechanism which had consumed or was actively consuming the oxygen in the water in the footers. Accordingly a test for Biochemical Oxygen Demand (BOD) was performed. Water specimens were collected near the surface and near the floor of each footer (the latter collection was conducted by the divers) and subsequently analyzed. The greatest BOD values in both footers averaged only 4.8 mg/L which is similar to values that are obtained when sampling a “relatively unpolluted stream”. [USGS 2003] This would suggest that no strong chemical oxygen consumption mechanism was present there, but it is noted that tests of this type, at least in seawater, may tend to underestimate the BOD. [Simon 2011]

Observations of the corrosion condition of reinforcing steel were limited to opportunities provided by the five cored holes described above. As indicated in Table C3, only one out of the 5 cores (centered on a crack) showed any indication of rebar corrosion. Rebar exposed by the other on-crack core and the three off-crack cores did not show signs of corrosion. In all cases where coating adhesion was examined it was found to be deficient (as is commonly the case for epoxy-coated steel bars in Florida bridges [Lau et al. 2010]). Analysis of chloride concentration in the cores indicated that penetration to the rebar depth was found to be important only in the case of the on-crack core examined. The profiles also showed an appreciable but still moderate level of surface chloride in the concrete, consistent with the submerged condition (no evaporative buildup) and with some extent of dilution by freshwater. The corresponding estimated chloride diffusion coefficient for the sound concrete cores is consistent, together with the high concrete resistivity measured, with the concrete being of low

permeability as expected from the high-performance mixture proportions specified for this bridge. [Lau et al. 2010]

The results suggest that, given the low permeability of the concrete in the footer chambers, premature rebar corrosion may be a concern only at crack locations. The observation of corrosion in one of the two crack locations examined validates that concern. Corrosion at those locations could be aggravated to some extent by macrocell coupling with steel exposed at epoxy coating breaks in the rest of the assembly. Previous work has shown that such aggravation can be severe if the extent of coating breaks is high (for example, exposing as much as 2% of the underlying steel). [Sagüés et al. 1991] An earlier survey of epoxy coated rebar condition in the Sunshine Skyway Bridge indicated 0.57% bare area exposed. [Sagüés et al. 1994] A report on work performed by a contractor during the 2012 inspection indicated a high degree of electric continuity (89% [Figg 2013]) for the epoxy-coated rebars in the footer chambers. Hence some key factors for macrocell corrosion aggravation of the crack-intersecting rebar are present, via mechanisms analogous to those considered in the previous subsections for pilings.

APPENDIX D: ROBUSTNESS OF MODEL OUTPUT

Robustness of the model output to choices of FEM mesh size, value of SF, and C_s distribution was ascertained by trial calculations. Calculations for mesh size and SF were performed with only the model indicated in each case but can be applied to both the steady-state and dynamic models as the models share current distribution calculations.

D.1 Mesh Size (Dynamic Model)

Total anodic current of the rebar assembly was chosen as a metric for mesh size sensitivity quantification. Normal simulations were performed with the “Coarse” element size setting of the FEM software package used. For comparison, 100-year Case 5 simulations without SACP were run using both the “Fine” and “Extra Coarse” settings. The ratio of the difference between the maximum and minimum projected currents to the minimum projected current among the three simulations was calculated as a percentage at 10-year intervals. The resulting values averaged $<1.1\%$. Accordingly, the model output was deemed to be largely robust to the choice of mesh size. Furthermore the average of the percentage difference between the absolute value of total anodic and cathodic current evaluated at 10-year intervals for all three mesh sizes was $<0.3\%$ indicating finely achieved current conservation.

D.2 Steel Factor (SF) (Steady-State Model)

Corrosion rate as a function of below-water active steel percentage was evaluated using an alternative value of SF=2 instead of SF=1 as was used for all other simulations. The nominal exchange current densities of the anodic and cathodic reactions over the entire rebar assembly were reduced by half in the expectation of obtaining approximately the same macrocell current levels as in the main sequence of calculations. Since nearly limiting diffusional conditions predominated in the submerged zone, the corresponding value of the total available oxygen reduction current below water would be expected to remain about the same there regardless of the value of surface area ratio for a given rebar cover. However, given the increased SF the corresponding anodic current density in the submerged region would be expected to be reduced by about half. As shown in Figure D1, the submerged region corrosion rate results of the SF = 2 simulations, after being multiplied by the SF, closely agreed with the results obtained using SF=1 as expected. These calculations illustrate robustness of the model output trends to the choice of steel placement density.

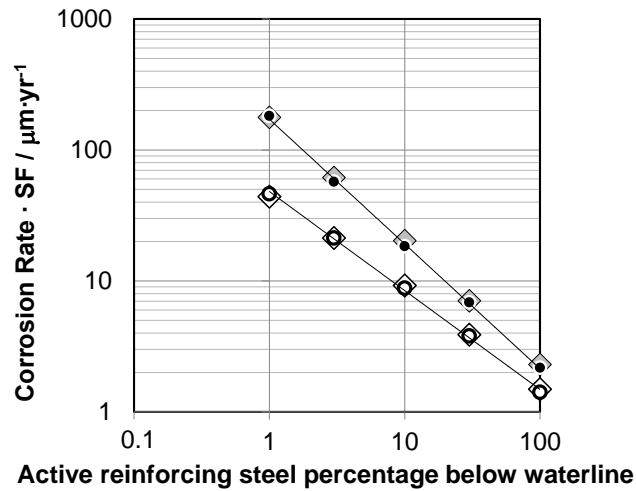


Figure D1. Corrosion rate as a function of active rebar surface area percentage. Rates were averaged over the active area. Filled symbols correspond to cases with no corrosion above waterline, resulting in higher corrosion rates in submerged zone. Circles denote the regular calculations with $SF=1$; diamonds denote cases with $SF = 2$, for which each result was multiplied by two as described in the text.

D.3 Surface Chloride Concentration Profile (Dynamic Model)

A 100-year Case 1 simulation was computed for five additional manifestations of the randomly varied chloride profile, using the same 0.25 coefficient of variation. The DF was computed for each simulation and subsequently plotted for comparison with each of the other damage functions (including the DF generated by using with the C_s profile shown in Figure 34). The results, shown in Figure D1, indicate that the different manifestations in randomly dispersed concrete surface chloride profiles lead to essentially equivalent DF projections sharing a similar overall trend.

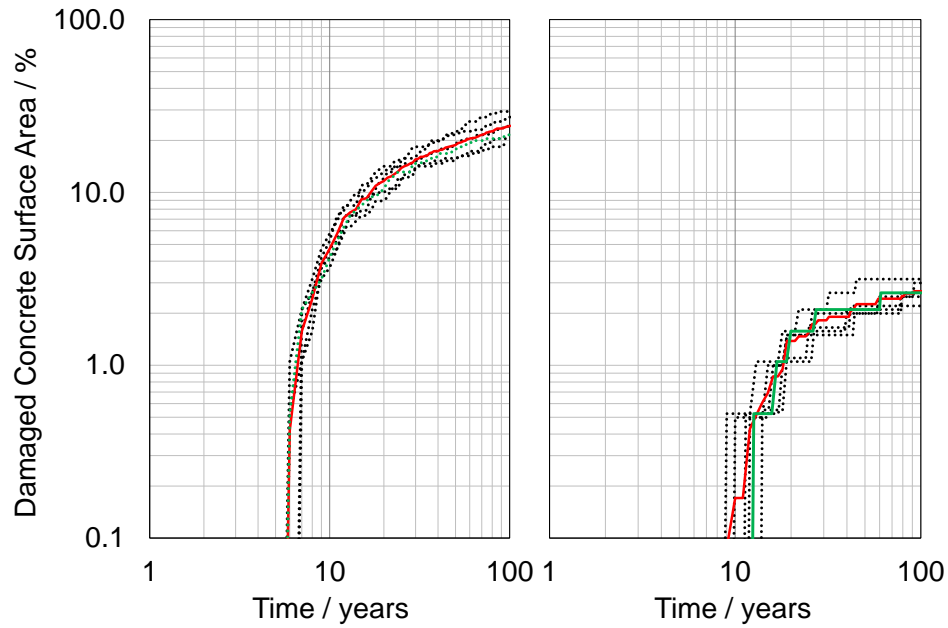



Figure D2. Damage functions for multiple chloride profiles, Case 1. Each DF is based on one of five different 0.25 coefficient-of-variability realizations of the chloride profile shown in Figure 34 (top). Left: DFs for all steel in the column; $P_{\text{Crit}} = 100 \mu\text{m}$. Right: DFs for steel in the submerged zone only; $P_{\text{Crit}} = 250 \mu\text{m}$. Green dotted line: profile used for the main body of calculations; Red solid line: average of all six profiles.

APPENDIX E: COPYRIGHT PERMISSION

Figures 2, 6, 7, 16, 18, 25, 26, 27, 28, 29, and 30 and portions of text in Chapters 1, 2, and 3 have been reproduced with permission from NACE International, Houston TX. All rights reserved. Paper 4364 presented at CORROSION/2014, San Antonio, TX.
 © NACE International 2014.



Permission to Publish
NACE International
Copyrighted Paper/Article

NACE International
 1440 South Creek Drive
 Houston, TX 77064
 Tel: 281-228-6219
 Fax: 281-228-4319

Date: 11/7/2015

Name: MICHAEL T. WALSH Title: GRADUATE RESEARCH ASSISTANT

Company (Publisher): UNIVERSITY OF SOUTH FLORIDA

Address: 4202 E FOWLER AVE, ENC 3300

Tel: 727-941-1111 Fax: 813-974-2957

Email: _____

Publication Media: Check the applicable Box:

Magazine/Journal ("Periodical"): _____ Issue: _____

Web Site URL ("Web Site"): for Dissertation

Circle the source: Materials Performance CORROSION Conference Paper Standards

Paper/Article Title: REBAR CORROSION IN SUBMERGED CONCRETE STRUCTURES - MODELING AND FIELD RESULTS ("Work") Conference Paper No./Year: 4364/2014

Authors: MICHAEL T. WALSH AND ALBERTO A. SAGÜES

NACE International ("NACE") hereby grants to "Publisher" the right to publish the Work utilizing the Publication Media elected above. To the extent the Publication Media is a Periodical, the publication right is limited to publication in the specific issue identified above and this right shall automatically terminate upon the date of issue of the particular issue of the Periodical, whether or not such Work is actually published. To the extent the Publication Media is a Web Site, the publication right is limited to publication at the specific Web Site identified above. Any right granted herein is a limited, non-transferable, non-exclusive right. No other rights in the Work are granted herein. The Publisher agrees to hold NACE harmless and indemnify NACE against any and all legal action and expenses arising out of the Publisher's use and editing of NACE material.

Notwithstanding the foregoing, Publisher may edit or otherwise modify the Work as reasonably necessary to accommodate the style and size requirements of the specific publication so long as the published Work that will appear in the Publication remains substantially similar to the original Work. Any such permitted edit or modification shall maintain the integrity of the overall original Work.

Publisher shall obtain a copy of the original Work directly from NACE International and shall not utilize copies of the Work from other sources, including the author(s). Publisher shall include on the published version of the Work the names of all authors listed on the original Work.

The Publisher shall include the following applicable Copyright notation with any publication of the Work*

A. Conference Paper
 Reproduced with permission from NACE International, Houston, TX. All rights reserved. Paper NUMBER presented at CORROSION/YEAR, City, State. © NACE International YEAR.

B. Magazine/Journal Article
 Reproduced with permission from NACE International, Houston, TX. All rights reserved. Published in the MONTH, YEAR issue of JOURNAL. © NACE International YEAR.

C. Standards
 STANDARDS/TECHNICAL COMMITTEE REPORT NAME. © NACE International YEAR. All rights reserved by NACE. Reprinted with permission. NACE standards are revised periodically. Users are cautioned to obtain the latest edition; information in an outdated version of the standard may not be accurate.

* Modifications to Notations: Other reference wording can be used, but must be approved by NACE in writing in advance.

As between NACE and Publisher, Publisher acknowledges that NACE owns all rights in the Works. Publisher shall not be entitled to any compensation for its efforts in promoting the Work.

PURPOSE OR CONDITIONS OF ACCURACY, COMPLETENESS OR QUALITY AND THOSE ARISING BY STATUTE OR OTHERWISE IN LAW, ARE HEREBY DISCLAIMED.

IN NO EVENT WILL NACE BE LIABLE FOR ANY DIRECT, INDIRECT, PUNITIVE, SPECIAL, INCIDENTAL OR CONSEQUENTIAL DAMAGES IN CONNECTION WITH OR RELATED TO THIS AGREEMENT (INCLUDING LOSS OF PROFITS, USE, DATA, OR OTHER ECONOMIC ADVANTAGE), HOWSOEVER ARISING.

This Agreement and the rights granted herein may be terminated immediately by NACE upon breach of this Agreement by Publisher. Unless earlier terminated, this Agreement and the rights granted herein will automatically terminate 6 months from the Date set forth above. If the Work has not been published within that time period, a new Agreement must be obtained.

Publisher may not, directly or indirectly, sell, assign, sublicense, lease, rent, distribute, or otherwise transfer this Agreement or any rights granted herein, without the prior written consent of NACE.

If any provision of this Agreement is found to be unenforceable, then this Agreement shall be deemed to be amended by modifying such provision to the extent necessary to make it legal and enforceable while preserving its intent. The remainder of this Agreement shall not be affected by such modification.

This Agreement does not create, and shall not be construed to create, any employer-employee, joint venture or partnership relationship between the parties. No officer, employee, agent, servant or independent contractor of either party shall at any time be deemed to be an employee, servant, agent or contractor of any other party for any purpose whatsoever.

This Agreement shall be governed by, and construed and enforced in accordance with, the laws of the State of Texas, without regard to the choice of law provisions of that State.

This Agreement shall only be effective if signed by authorized representatives of both parties. This Agreement constitutes the entire Agreement between the parties with respect to the subject matter of this Agreement. Any change, modification or waiver hereto must be in writing and signed by authorized representatives of both parties.

Other Terms & Conditions: _____

Publisher hereby requests permission to publish the paper/article described above and agrees to comply with all Terms and Conditions listed above.

Request submitted by:

MICHAEL T. WALSH
Printed Name

GRADUATE RESEARCH ASSISTANT
Title

Signature

11/7/2015
Date

Request approved by NACE:

Brenda Nitz
Printed Name

Advertising Coordinator
Title

Signature

Nov 9, 2015
Date

Request agreed to by:

MICHAEL T. WALSH
Lead Author Printed Name

GRADUATE RESEARCH ASSISTANT
Lead Author Title

Lead Author Signature

11/7/2015
Date

ABOUT THE AUTHOR

Michael T. Walsh was born and raised in Poland, Ohio, U.S.A. After graduating from Struthers High School in 1988, he proceeded to Case Western Reserve University in Cleveland, Ohio and earned a Bachelor of Science degree in Mechanical Engineering.

Walsh began his career in the American automobile industry working for the tier-one fuel system supplier Solvay Automotive Inc. in Troy Michigan. After five years, he returned to Ohio to work for the thermoplastic elastomer company Advanced Elastomer Systems, LP. Walsh joined the United States Navy in 1999 and was subsequently commissioned as a Civil Engineer Corps Officer. He served at both the United States Naval Academy in Annapolis, Maryland and Naval Mobile Construction Battalion 74 in Gulfport, Mississippi.

Upon honorable discharge from the U.S. Navy in 2005, Walsh accepted a position with American Land Lease, Inc. in Clearwater Florida and later enrolled as a graduate student at the University of South Florida (USF) in Tampa, Florida. He completed a Master of Science degree in Civil Engineering (area of concentration: Materials) and remained at USF to continue his research. He attained doctoral candidacy in September 2014 and defended his doctoral dissertation in October 2015.

Soli Deo Gloria.